ABSTRACT

HYDRODYNAMICS, DISSOLUTION, AND MASS TRANSFER EFFECTS IN DIFFERENT DISSOLUTION TESTING APPARATUSES AND LABORATORY SYSTEMS

by
Bing Wang

Dissolution testing apparatuses and shaker flasks agitated by shaker tables are laboratory systems routinely found in many laboratories at most companies and agencies, and especially in pharmaceutical companies. These devices are commonly used in a number of applications, from drug development to quality control. Despite their common use, these systems have not been fully investigated from an engineering perspective in order to understand their operation characteristics. For example, the hydrodynamics of many of these systems have received little attention until relatively recently, and only over the last few years have some of these systems, such as the USP dissolution testing Apparatus 2, been studied in greater detail by a few research groups, including our group at NJIT. Meanwhile, a number of modifications have been introduced in industry to simplify the practical use of these devices and to automate many of the processes in which they are utilized. This, in turn, has resulted in the introduction of variability in the way these devices are operated, with possible implication for the results that they generate in laboratory experiments and tests.

Therefore, this work was aimed at studying some of these devices in order to quantify how such systems operate and what the implications for their use in the laboratory are. More specifically, the systems that were examined here included the USP Dissolution Testing Apparatus 2 with and without automatic sampling probes, dissolution testing mini vessel apparatuses, and baffled shaker flasks. In order to study all these phenomena, a

number of tools were used, including Particle Image Velocimetry (PIV) and Computational Fluid Dynamics (CFD) to investigated the hydrodynamics of these systems; experimental tablet dissolutions under a number of controlled environments; and a combination of experimental, computational and modeling approaches to study mass transfer and solid suspension effects. The issues that were investigated depended on the specific apparatus.

For the case of the USP Dissolution Testing Apparatus 2, the effects of the presence of different probes on the hydrodynamics in the dissolution vessel and on the dissolution profiles using solid dosage forms were investigated in this work. The results indicate that in most cases, the presence of the probe resulted in statistically significant increases in the dissolution curves with respect to the curves obtained without the probe, and that tablets at, or close to, the center of the vessel were more significantly affected by the presence of the probe, and so were tablets located immediately downstream of the probe. The hydrodynamic effects generated by the arch-shaped fiber optic probe were small but clearly measurable. The changes in velocity profiles in the dissolution vessel resulted in detectable differences in the dissolution profiles, although not high enough to cause test failures. However, these differences could contribute to amplify the difference in dissolution profiles in those cases in which tablet has an intrinsically higher release rate. In addition, the minimum agitation speed, N_{js}, to achieve particle suspension was investigated. A novel method to determine N_{js} was first developed and then applied to determine N_{js} as a function of different operating variables.

Similarly, the hydrodynamics of smaller dissolution apparatuses termed “minivessels” were studied here and compared with the standard USP 2 system. The flow pattern in minivessels was obtained by both CFD simulations and PIV velocity measurements for four different agitation speeds in the mini vessel, and it was shown to result in flow patterns qualitatively similar to those in the standard USP 2 system. The velocity profiles were also compared on several iso-surfaces for the mini vessel system and the standard system, showing difference between two systems. In the most important zone, i.e., the inner core zone at the vessel bottom, the velocities were similar on the lowest iso-surface, especially for the axial velocity at 100rpm and 125rpm in the mini vessel compared with 100rpm in the 900mL USP 2 system. This was not clearly the case for iso-surfaces above the bottom zone.

Finally, the hydrodynamics of baffled shaker flask was investigated. These baffled "trypsinizing" flasks are similar to the typical Erlenmeyer-type conical shaker flasks commonly used in biological laboratories but with a major difference, in that they are provided with vertical indentations in the glass flask so as to create vertical baffles that promote better mixing when shaken. Measurements of the velocity in the flask were obtained using PIV for seven rotation speeds of 100, 125, 150, 160, 170, 200, and 250 rpm. Two vertical cross sections were measured to obtain the velocity profiles in the flask: the one with largest diameter of the flask, and the one with the smallest diameter. The 1D energy spectra indicate nearly isotropic flow in the BF for all rotation speeds and the existence of inertial subrange, which validate the use of dimensional argument analysis for the estimation of energy dissipation rate.

The results obtained in this work will contribute to increase our understanding of the performance of a number of very common and important laboratory apparatus thus contributing to a more appropriate use of all these devices in both industry and federal and state agencies.

HYDRODYNAMICS, DISSOLUTION, AND MASS TRANSFER EFFECTS IN DIFFERENT DISSOLUTION TESTING APPARATUSES AND LABORATORY SYSTEMS

by
Bing Wang

A Dissertation
Submitted to the Faculty of
New Jersey Institute of Technology
in Partial Fulfillment of the Requirements for the Degree of
Doctor of Philosophy in Chemical Engineering

Otto H. York Department of Chemical, Biological and Pharmaceutical Engineering

August 2015

APPROVAL PAGE

HYDRODYNAMICS, DISSOLUTION, AND MASS TRANSFER EFFECTS IN DIFFERENT DISSOLUTION TESTING APPARATUSES AND LABORATORY SYSTEMS

Bing Wang

Dr. Piero M. Armenante, Dissertation Advisor Distinguished Professor of Chemical Engineering, NJIT Director, Pharmaceutical Engineering Program, NJIT	Date
Mr. Gerard Bredael, Committee Member Associate Principal Scientist, Merck & Co.	Date
Dr. Zongming Gao, Committee Member Chemist, FDA	Date
Dr. Costas Gogos, Committee Member Distinguished Research Professor of Chemical Engineering, NJIT	Date
Dr. Norman Loney, Committee Member Professor of Chemical Engineering, NJIT	Date
Dr. Laurent Simon, Committee Member Associate Professor of Chemical Engineering, NJIT	Date

BIOGRAPHICAL SKETCH

Author: Bing Wang

Degree: Doctor of Philosophy

Date: August 2015

Undergraduate and Graduate Education:

- Doctor of Philosophy in Chemical Engineering,
  New Jersey Institute of Technology, Newark, NJ, 2015
- Master of Engineering in Chemical Engineering,
  Tianjin University, Tianjin, China, 2010
- Bachelor of Science in Applied Chemistry,
  Tianjin University, Tianjin, China, 2008

Major: Chemical Engineering

Publications:

Wang, Bing; Bredael, Gerard; Armenante, Piero. Effect of a Fiber-Optic Probe on the Dissolution of Salicylic Acid Tablets in USP Apparatus 2, *Dissolution Technologies*, **2013**, *20* (2), 21-30.

Duan, Changchun; Wang, Bing; Liu, Chunjiang; Yuan, Xigang. Flow Pattern Optimization of a Sieve Plate Extraction Column Using Computational Fluid Dynamics Simulations and Particle Image Velocimetry Measurements, *Ind. Eng. Chem. Res.*, **2013**, *52* (10), 3858–3867.

Zhao, Lin; Wang, Bing; Armenante, Piero; Conmy, Robyn; Boufade, Michel. Characterization of Mixing in the EPA Baffled Flask for Dispersion Effectiveness Testing. *J. Environ. Eng.*, 2015, in press.

Manuscript in Preparations:

Wang, Bing; Bredael, Gerard; Armenante, Piero. Hydrodynamic effect of a fiber optic arch shaped probe inserted the USP Dissolution Testing Apparatus 2.

Wang, Bing; Bredael, Gerard; Armenante, Piero. Hydrodynamics and strain rate study of mini vessel system compared to the standard USP Dissolution Apparatus 2.

Zhao, Lin; Wang, Bing; Armenante, Piero; Conmy, Robyn; Boufade, Michel. Mixing Characterization of the horizontal planes in the EPA Baffled Flask for Dispersion Effectiveness.

Presentations

Bing Wang and Piero M. Armenante, "CFD-Predicted and PIV-Measured Velocity Profiles in a USP Dissolution Testing Apparatus 2 Equipped with an Arch-Shaped Fiber Optic Probe and Their Impact on Tablet Dissolution," In Tools for Accelerating Pharmaceutical Development Forum, 2014 American Institute of Chemical Engineers Annual Conference (AIChE), Atlanta, USA.

Bing Wang and Piero M. Armenante, "Hydrodynamic effect of a fiber optic arch shaped probe inserted the USP Dissolution Testing Apparatus 2," In Graduate Student Division, 2014 International Society for Pharmaceutical Engineering (ISPE), New Jersey, USA.

Bing Wang and Piero M. Armenante, "Effect of a Fiber-Optic Probe on the Dissolution of Salicylic Acid Tablets in USP Apparatus 2," In Graduate Student Division, 2013 International Society for Pharmaceutical Engineering (ISPE), New Jersey, USA.

~To my beloved Parents and my Dear Husband for their love, support and encouragement~

仅以此书献给我的父母以及爱人的支持，是你们的鼓励和支持让我顺利完成博士学历！

~书山有路勤为径
学海无涯苦作舟~

ACKNOWLEDGMENT

I would like to express my deepest gratitude to my Advisor, Professor Piero M. Armenante. Dr. Armenante is Distinguished Professor at NJIT and has contributed valuable and countless resource to the Chemical Engineering department. Although he is busy working as the Director of Pharmaceutical Engineering program, he constantly gave me support, encouragement, and thorough guidance. Dr. Armenante's hardworking qualities, professionalism and decency will always serve as an inspiration to me.

I express my deep gratitude to Mr. Gerard Bredael for his kind guidance of my Ph.D. work and his great contribution for most of the entire projects. I would also like to thank Dr. Zongming Gao, Dr. Costas Gogos, Dr. Norman Loney and Dr. Laurent Simon for serving on my dissertation committee. I would like to give special thanks to Mr. Shawn W. Yetman and Mr. Robert Lions for great help with the equipment. They have used their professional background and expertise to provide me with great support. I would like to express my deepest appreciation to Ms. Qianqian Liu for her kindly help in carrying out my research at the starting point. I would also like to thank Yiran Zhang and all the members of the research group in the Mixing Lab for their help in my study and research.

This work was partially supported through a grant from Merck & Co., Summit, NJ, whose contribution is gratefully acknowledged. The author also wish to thank Mr. Gerard Bredael again for his great contribution and support.

TABLE OF CONTENTS

TABLE OF CONTENTS
(Continued)

TABLE OF CONTENTS
(Continued)

Chapter **Page**

TABLE OF CONTENTS
(Continued)

Chapter **Page**

LIST OF TABLES

LIST OF FIGURES

LIST OF FIGURES
(Continued)

LIST OF FIGURES
(Continued)

LIST OF FIGURES
(Continued)

LIST OF FIGURES
(Continued)

LIST OF FIGURES
(Continued)

LIST OF SYMBOLS

d_T	Diameter of tablet
ρ_L	Density of water
μ	Viscosity of water
D_{AB}	Diffusivity of the salicylic acid in water
Φ	Association parameter of the solvent (water)
M	Molecular weight of the water
V_A	Solute molar volume
υ	Kinematic viscosity of water

CHAPTER 1

INTRODUCTION

1.1 Background

Dissolution testing apparatuses and shaker flasks agitated by shaker tables are laboratory systems routinely found in many laboratories at most companies and agencies, and especially in pharmaceutical companies. These devices are commonly used in a number of applications, from drug development to quality control.

Dissolution testing is a critical technique in the pharmaceutical industry to evaluate solid and semi-solid dosage forms *in vitro*, examine the dissolution behavior to differentiate formulation types, and provide an optimization of drug release from formulations. The United States Pharmacopeia (USP) lists several standardized dissolution testing methods and apparatuses, and the most widely used of these devices are the USP Dissolution Testing Apparatus 1 and 2.

USP Apparatus 1, the rotating basket dissolution apparatus, was developed in 1960s, and the USP Apparatus 2 was developed shortly after Apparatus 1. Both systems consist of a 1 L cylindrical, hemispherical bottom, unbaffled vessel and a shaft agitator. The difference of the two systems is the device at the end of the shaft: USP Apparatus 1 has a mesh basket, and this device is appropriate for dosage forms such as capsules, beads and suppositories. The design of the basket can prevent light drugs from floating around during the dissolution tests. The USP Apparatus 2 contains a paddle instead of the mesh basket in the same vessel as the USP Apparatus 1. The USP Apparatus 2 is usually used for tablets heavier that the dissolving liquid medium which can rapidly sink when dropped into dissolution medium. In general, a suitable dissolution test method for a specific drug product needs to be considered, specifying operating variables such as the dissolution medium, pH value, dissolution medium volume, temperature control, agitation speed, and other important variables.

In the industrial practice, some modifications are often made to the standard USP Apparatus 2 for some specific use or in order to overcome some limitations. For example, manually sampling is routinely conducted in dissolution processes. However, there are several disadvantages to this approach, such as labor intensiveness, the possible introduction of operator error, the small number of data that can be reasonably collected with this approach due to the need for human intervention, and the progressive removal of medium over time as a result of sampling. In order to overcome these limitations, automatic sampling probes can be used, thus simplifying and automating testing procedures. Fiber optic probes are the most widely used sampling probes, and several types are available. Based on their shape and location where they are placed in the vessel, fiber optic probes can be categorized into three types, as shown in Figure 1.1. The shaft probes are usually fixed in a hollow shaft and placed at the center of the vessel. The rod probe is essentially a solid rod dipped in the vessel with a detection window in the traditional sampling location defined by United States Pharmacopeia (USP). Arch-shaped probes consist of a metal arch with a detection gap at the bottom of the probe located at the traditional USP sampling location [1].

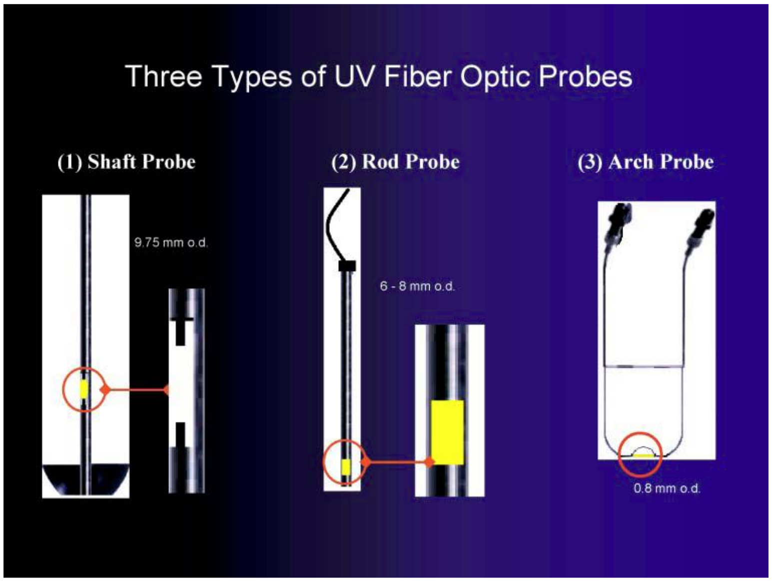

Figure 1.1 Three types of UV Fiber Optic Probes [1].

UV light is able to get into the dissolution medium from one side of the gap and travels to the other side. Therefore light absorption data can be obtained. This system also has other advantages, such as small displacement volume, simple light path, and reduced bubble and particulate accumulation [2]. The arch-shaped probe can be used in the USP Dissolution Apparatus 2 to automatically determine the dissolution profiles. However, the effect of a probe on the hydrodynamic of USP Apparatus 2 system and the resulting dissolution effects need to be studied to ensure that automatic sampling can be widely used industrially.

In most pharmaceutical companies, the use of the standard USP Apparatus 2 and dissolution methods are well established and this system is typically the first choice for dissolution test. However, for some specific cases, such as when very small tablets are used or only small amounts of drug product are available during the development stage, these traditional methods have practical limitations which can result in lower analytical sensitivity. In this regard, the standard USP Apparatus 2 dissolution method has been modified, and a small volume dissolution vessel with a mini paddle has been suggested as an alternative to standard dissolution equipment. This mini vessel system consists of a small volume vessel with a small-size impeller similar in shape to the USP Apparatus 2. However, this mini vessel dissolution apparatus and method are not yet included in the US Pharmacopoeia (i.e., it is not yet a "compendial" method). This implies that some important issues must to be considered, such as results reliability, apparatus calibration, method validation, and so on, before this approach can be widely used. In addition, the hydrodynamics of these systems has not been investigated so far, and it is unclear how dissolution tests conducted in mini vessels compare to those obtained in the standard USP Apparatus 2. Therefore, the mini vessel system needs to be studied in greater details before it can be widely used in the industrial practice.

In many laboratories, orbital shakers are also frequently used. These systems typically include an orbital shaker device powered by an electric motor, which can generate a smooth uniform circular motion transmitted to a non-slip table mat that can hold up flasks during shaking action. The shaker table board is rotating horizontally, and the beakers or flasks that it supports are shaken in a similar orbital fashion. In addition to conical flasks, orbital shakers are often used to rotate baffled trypsinizing flasks which are widely used in sampling preparation of biochemical companies. “Trypsinizing” flasks are similar to the typical Erlenmeyer-type conical shaker flasks commonly used in biological laboratories but with a major difference, in that they are provided with vertical indentations in the glass flask so as to create vertical baffles that promote better mixing when shaken. During the agitation process, the cells that adhere to vessel can be more easily dislodged. This system is also used at the laboratory scale for the culture of animal cells in a suspension mode. Particle suspension can be experimentally characterized in orbital shaker system, and correlations for the critical agitation conditions for complete particle suspension have been developed [3]. The system is a basic tool in that laboratory and has an important role in aggregation and breakup of particles. The aggregation behavior was studied under various conditions of induced shear rate and particle volume concentration for particle aggregates smaller than the Kolmogorov scale experimentally by the shaker system [4].

Baffled trypsinizing flasks are also used by the Environmental Protection Agency for environmental studies. These flasks are routinely filled with oil-water mixtures and are placed on orbital shakers to simulate oil dispersion in water during oil spills. This approach is used to study, in flasks, the dispersion effectiveness caused by different mixing intensities and small scale turbulence structures similar to those anticipated at sea. By using this approach, the dispersant breakdown in the sea can be studied at the laboratory scale and the flow inside the flask can be used to characterize the type of mixing occurs from breaking waves at sea. In the past, a hot-wire anemometer was used to measure the turbulence intensity in these system so that the energy dissipation rate could be determined [5]. However, hot-wire anemometry is an invasive measurement and other approaches should be used to better characterized energy dispersion in such systems. Therefore, there is a need to extend this type of research in order to provide a more detailed characterization of flow and energy dissipation in this kind of apparatuses.

1.2 Motivation and Overall Objectives of This Work

Despite their common use, these routinely-used laboratory systems have not been fully investigated from an engineering perspective in order to understand their operation characteristics. For example, the hydrodynamics of many of these systems have received little attention until relatively recently, and only over the last few years have some of these systems, such as the USP dissolution testing Apparatus 2, been studied in greater detail by a few research groups, including previous work in the research group of Prof. Armenante [6, 7]. Meanwhile, a number of modifications have been introduced in industry to simplify the practical use of these devices and to automate many of the processes in which they are utilized. This, in turn, has resulted in the introduction of variability in the way these devices are operated, with possible implication for the results that they generate in laboratory experiments and tests. *Therefore, the overall objective of work is to study these devices from a hydrodynamic perspective in order to quantify how such systems operate and what the implications are for their use in the laboratory.*

More specifically, the systems that have examined here are the following: USP Dissolution Testing Apparatus 2 with and without automatic sampling probes, dissolution testing mini vessel apparatuses, and baffled trypsinizing shaker flasks. The specific issues that were investigated depended on the specific apparatus.

For the case of the USP Dissolution Testing Apparatus 2, the modification is on the sampling process. Pharmaceutical company are eager to intend to replace manual sampling with automatically sampling, which implies that the fiber optic probe should be inserted into the dissolution vessel to do the sampling work automatically. However, the hydrodynamics of USP Apparatus 2 has been shown to be very complex, and the USP 2 system is very sensitive to any deviation from perfect symmetry, which may introduce hydrodynamic changes. The use of a probe introduces asymmetry in the USP 2 system and may act as a “baffle” in the liquid flow. The insertion of baffles in any mixing system improves mixing performance by altering the system’s hydrodynamics, which, in a dissolution testing device, can result in dissolution rates changes. Possible changes in the dissolution performance and flow field should be considered before replacing the current methodology with this technique. Therefore, the effects of the presence of different probes on the hydrodynamics in the dissolution vessel and on the dissolution profiles using solid dosage forms have been investigated in this work. In addition, the agitation speed, N_{js}, to achieve the just suspended state of solid particles in the USP Apparatus 2 system has been investigated, in order to determine the values of N_{js} under different experiment conditions such as particle size and particle density.

Secondly, the hydrodynamics of smaller dissolution apparatuses termed “mini vessels” has been studied together with the dissolution profiles they generate. The flow pattern, flow velocity distribution, strain rate, and mass transfer coefficient were obtained through experimental measurements and computational simulation. The results were also compared with those obtained in the original USP Apparatus 2 system, in order to provide the operating conditions, such as the agitation speed in the mini vessel systems, that results in dissolution results closest to the original USP Apparatus 2 system.

Finally, the hydrodynamics of baffled trypsinizing shaker flasks was investigated. The turbulence structure inside the shaken baffled trypsinizing flask was investigated under seven agitation speeds. For each speed, the velocity profiles were obtained on two different vertical cross sections. To study the turbulent structure in the flask, there are several characteristic parameters of interest in the turbulent mixing process. The energy dissipation rate which can characterize the intensity of the mixing energy is one of the most important scaling parameters [8]. The second parameter is integral length which is based on the velocity field. The integral length can characterize the size of eddies containing most of the turbulence mixing energy [9]. The last one is Kolmogorov microscale which can provide an estimate for the smallest eddy that can exist in the turbulent flow. These parameters have been calculated and evaluated from the turbulent velocity field which can be obtained in different agitation speeds and different cross section of the flask.

In order to study these phenomena, a number of experimental and computational tools were used including Particle Image Velocimetry (PIV) and Computational Fluid Dynamics (CFD) to study the hydrodynamics of these systems and obtain the velocity profiles for each system. Experimental tablet dissolution profiles as a function of time under a number of controlled environments, especially for the USP 2 system with and without probe, were also obtained. The dissolution rates for the original USP 2 system and the modified system with a probe were compared in order to quantify the probe influence on the dissolution rate. Furthermore, a combination of experimental and computational approaches were used to study mass transfer and solid suspension effects. Also, a number of calculations from the velocity profiles have been done to obtain the characteristic parameters for turbulence study in the trypsinizing shaker flask system.

In summary, in this work the characteristics of both the original USP 2 system without probe and the modified USP 2 system with probe were studied in detail. The dissolution rates and hydrodynamics were provided more details and compared. Moreover, another alternative and similar dissolution vessel to the USP 2 system, i.e., the mini vessel system, was studied at different agitation speeds in order to determine its hydrodynamics and compare it to the closest case, i.e., the USP 2. To do so, the parameters such as velocity comparison, strain rates, and mass transfer coefficient were used. The hydrodynamics in another commonly used system, baffled, trypsinizing flask, was also studied. The turbulence structure inside the flask has been characterized by several parameters, which can be calculated form the velocity data.

In conclusion, this dissertation is focused on the study of the hydrodynamics in different commonly used laboratory devices in order to elucidate how these devices operate, and quantify the impact of different geometries and operating conditions on the critical variables that affect the performance of these devices and the experimental data that can be extracted from them.

CHAPTER 2

EFFECT OF A FIBER-OPTIC PROBE ON THE HYDRODYNAMICS OF USP APPARATUS 2 AND THE DISSOLUTION OF SALICYLIC ACID TABLETS

2.1 Background and Objective

In most industrial applications, the use of the USP Dissolution Testing Apparatus 2 to test drug release from solid oral dosage forms requires periodically removing liquid samples manually during the dissolution process and analyzing them separately, for example with a spectrophotometer or another analytical device, in order to quantify the drug concentration in the dissolution medium as a function of time. There are several disadvantages in this approach such as labor intensiveness, the possible introduction of operator error, the small number of data that can be reasonably collected with this approach due to the need for human intervention, and the progressive removal of medium over time as a result of sampling.

A different approach that can be used to overcome the limitations of manual sampling is by using probes that are permanently inserted in the dissolution medium and are connected to an external device to measure the dissolving drug concentration continuously. Since this method can save time and minimize errors, different types of probes have been developed, and several studies have appeared in the literature describing their performance, as well as their advantages and limitations [11-32]. Fiber optic probes, which are widely used sampling probes, are devices permanently immersed in the medium in the dissolution vessel. A light signal generated externally travels through a small gap in the fiber optic cable located in the dissolution medium. The attenuated light signal received at the other end of the cable is used by the external detection device to determine the evolving concentration of the dissolving drug. Fiber optic probes and their applications in dissolution testing have been studied for a number of years since the early study by Josefson [11]. These studies have indeed shown that probes can be advantageously used in dissolution testing, and that they generate accurate and reproducible dissolution data.

Despite these advantages, the use of fiber optic probes in dissolution testing can also raise some issues especially when a previously validated manual sampling process is converted to automatic sampling using a permanently inserted fiber optic probe. One of the main concerns is the effect that the presence of the probe can have on the hydrodynamics in the dissolution vessel and its impact on dissolution rates. Probes are typically small, but they can introduce asymmetry in the vessel and they can act as small obstacles ("baffles" in the fluid mixing literature) in an otherwise unstructured flow.

Even though there is no probe inserted in the system, the hydrodynamics in dissolution testing Apparatus 2 is very complicated. Early studies have reported that the hydrodynamics of Apparatus 2 is very complex which results in the poor reproducibility of dissolution testing data. The fluid flow in Apparatus 2 is highly heterogeneous and is strongly affected by even small variations of the apparatus geometry [33, 35, 36, 37, 38]. In the past decade, a limited number of literature studies have been focused on the hydrodynamics in Apparatus 2 by using CFD simulation and Laser-Doppler Velocimetry (LDV) or PIV for the experimental determination of velocities and flow pattern. The CFD simulation results can be compared with the velocity distribution obtained by PIV [39]. Bai et al. [40] has obtained the velocity profiles by CFD simulation and LDV measurements, which indicated that the flow pattern is nearly independent of different agitation speed, especially in the inner core region just below the impeller where the tablet is usually located. However, the small differences in equipment configurations and operating conditions can significantly affect the fluid hydrodynamics of Apparatus 2, and hence the tablet dissolution rate [38]. Furthermore, the impeller location can also affect the tablet dissolution rate. When the impeller is placed 8mm off center in the vessel, the dissolution profiles were largely independent of the tablet location at the vessel bottom, which can effectively eliminate artifacts generated by random settling of the tablet at the bottom, and the test is more robust [41]. This hydrodynamics effect in turn can possibly result in changes in the fluid velocity profile and in the shear rates, which can cause variations in dissolution testing profiles and dissolution rates. Several investigators have in fact observed such changes in dissolution rates [1, 2, 12, 13, 18, 20, 27, 31, 32].

Therefore, the objective of this section of the work was to quantify the possible changes in dissolution rates and hydrodynamics that can result from the introduction of a commercial fiber optic probe in the vessel.

Here, dissolution tests were conducted with non-disintegrating salicylic acid calibrator tablets in two USP Apparatus 2 systems, i.e., the experimental system (with the probe) and the standard control system (without the probe), in order to observe the difference of dissolution profiles caused by the probe itself when the tablets were dropped in the vessel at the beginning of the test. Significant efforts were made to minimize the effect of any other factor that could play a role in the dissolution tests. In addition, and to make the system more sensitive to the effect of small geometric differences, tests were also conducted with tablets fixed at several positions in the vessel. As shown in previous studies by this group [6, 7, 33], tablets placed at different locations on the vessel bottom can have different dissolution rates since they experience different flows around them and different shear stresses, especially if the system is non-symmetrical. Therefore, in this work, dissolution tests were conducted not only with the standard tablet drop technique specified in the USP [34], but also with tablets fixed in place at nine positions on the vessel bottom, i.e., the central position, four positions on the 10 °off-center circle, and other four positions on the 20 °off-center circle. Statistical tools were used to evaluate and compare the results at each tablet position.

Then, the hydrodynamic changes introduced by an arch-shaped fiber optic probe in a USP Dissolution Testing Apparatus 2 filled with 900 mL of dissolution medium were studied by (1) experimentally determining the velocity profiles in the vessel, with and without the probe, using Particle Image Velocimetry (PIV) and quantifying changes in the flow velocities on selected horizontal iso-surfaces; and (2) predicting the velocity distribution using Computational Fluid Dynamics (CFD). These results so obtained were used to analyze the dissolution data from of actual dissolution tests conducted with and without the probe using Prednisone tablets fixed at nine different locations at the bottom of the vessel.

2.2 Experimental Apparatus, Materials, and Methods

2.2.1 Dissolution Testing Experiments

USP 2 Dissolution Apparatus. Dissolution tests were conducted in a commercial USP Apparatus 2 (Distek 5100 Bathless Dissolution Apparatus; Distek Inc., North Brunswick, NJ) [7, 33, 42]. Two experimental systems were used, one with the inserted fiber-optic probe (Figure 2.1 A) and the other without the probe (Figure 2.1 B). In both cases, they were typical unbaffled, cylindrical, hemispherical-bottomed glass vessels with a maximum nominal volume of 1 L. The impeller consisted of the typical two-blade paddle impeller and a shaft. Exact dimensions were reported elsewhere [33, 42]. The effect of possible minor geometrical variations between vessels was eliminated by randomly choosing glass vessels in each experiment.

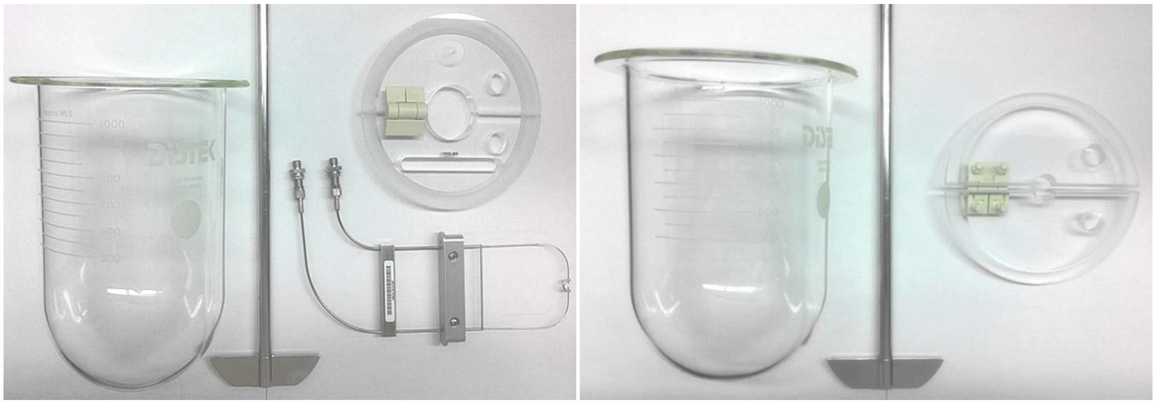

(A) (B)

Figure 2.1 Dissolution testing systems used in this work. (A) USP dissolution testing Apparatus 2 with fiber-optic probe: glass vessel, paddle impeller, modified lid, and fiber-optic probe; and (B) standard USP dissolution testing Apparatus 2: glass vessel, paddle impeller, and lid.

The fiber-optic probe was an arch-shaped Opt-Diss metal probe provided by the Merck Company, Summit, NJ. The probe consisted of two sections of thin vertical tubing, 0.8 mm in diameter, bent at the bottom to bring the ends horizontally to form a small gap (Figures 2.1 A and Figure 2.2 A). The two pieces of tubing were kept in position by two horizontal metal braces. The probe was installed inside the vessel by suspending it from a slotted lid cover so that the probe tip was in the correct sampling location specified in the USP [43]. The exact dimensions and location of the probe in the vessel are given in Figure 2.2 A–D.

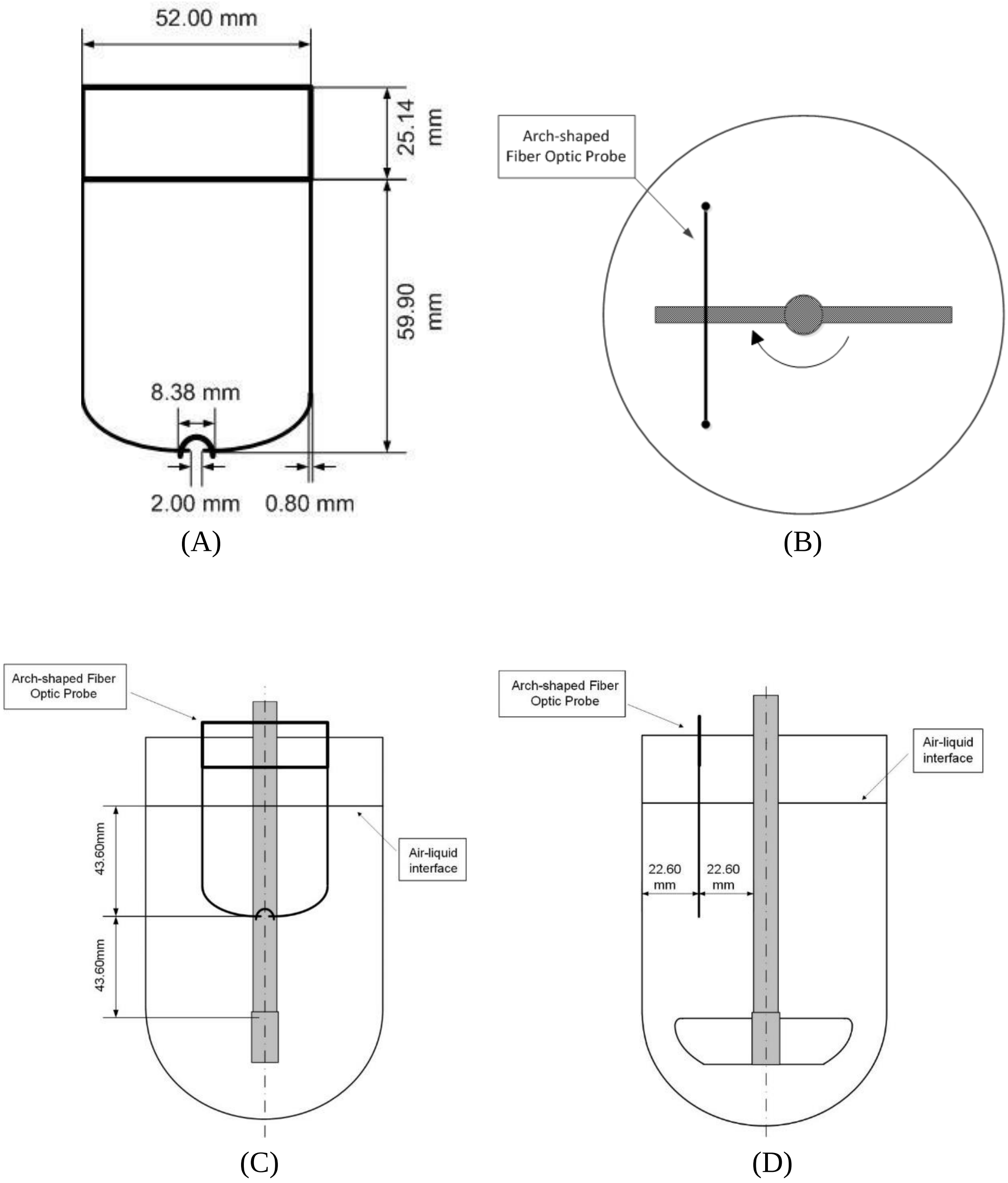

Figure 2.2 (A) Arch-shaped, fiber-optic probe used in this work and its dimensions; (B) top view of the probe in dissolution testing vessel; (C) side view of the probe in dissolution testing vessel; (D) front view of the probe in dissolution testing vessel.

Experiment Materials. Salicylic acid calibrator tablets (300-mg, non-disintegrating; USP lot #Q0D200), purchased from USP (Rockville, MD), were used in all experiments.

When needed to anchor the tablet, an exceedingly small amount of a commercial acrylic glue was used to fix the tablet at a particular location on the bottom of the dissolution vessel.

The dissolution medium for salicylic acid tablets was prepared in accordance with the USP General Chapter <711> Dissolution, using 0.05 M monobasic potassium phosphate and sodium hydroxide to obtain a buffer solution with a pH value of 7.4 ± 0.05. The solution was deaerated before use according to the method of Moore [44] in which the medium was be placed in a carboy tank connected to a vacuum pump, and vacuum was applied for 30 min. This stock solution was used as needed (900-mL aliquots per test).

Experiment Method. Experiments were first conducted following the standard USP procedure [43]. Accordingly, the dissolution medium was heated to 37 °C, the agitation was started at 100 rpm, and the tablet was dropped. In the experimental group tests, the optic probe was inserted at the same time the tablet was dropped. In the control group, no probe was present. In each side-by-side experiment, two tablets were tested simultaneously in the two systems. The first pair of samples was taken immediately after the tablet was dropped (t = 0). Additional samples were taken at 5-min intervals. Each experiment lasted 45 min. A 10-mL syringe with a 2-mm diameter cannula was used to take 10-mL samples manually from the buffer medium in both systems, with and without the probe (i.e., the fiber-optic probe was not used for sample analysis in order to eliminate the sample collection method from the list of experimental variables). A PVDF 0.45-µm filter was mounted on the syringe to remove solid particles that could possibly be drawn in with the sample. The first 2 mL of the sample were discarded, and the remaining aliquot was transferred to a vial for further analysis, as described below. All paired experiments were performed in triplicate.

Additionally, a separate group of experiments was conducted in which the tablets were not dropped into the medium but instead glued on the bottom of the vessel before the beginning of the test. This approach was similar to that previously described [42] and was used here to determine the sensitivity of the tablet dissolution process to tablet location, as when the tablet remained stuck to the vessel bottom during the dissolution process. Therefore, the experimental procedure was slightly modified from that specified in the USP since the tablets had to be glued on the bottom of the vessel before beginning the test. Before the experiment, two tablets were fixed with a very small bead of glue in the same position in both setups (i.e., in the standard system without probe and in the experimental system with the fiber-optic probe inserted). The probe system was nonsymmetrical since the probe was placed on one side of the vessel. Therefore, nine different tablet locations were investigated, as shown in Figure 2.3 (A) and Figure 2.3 (B).

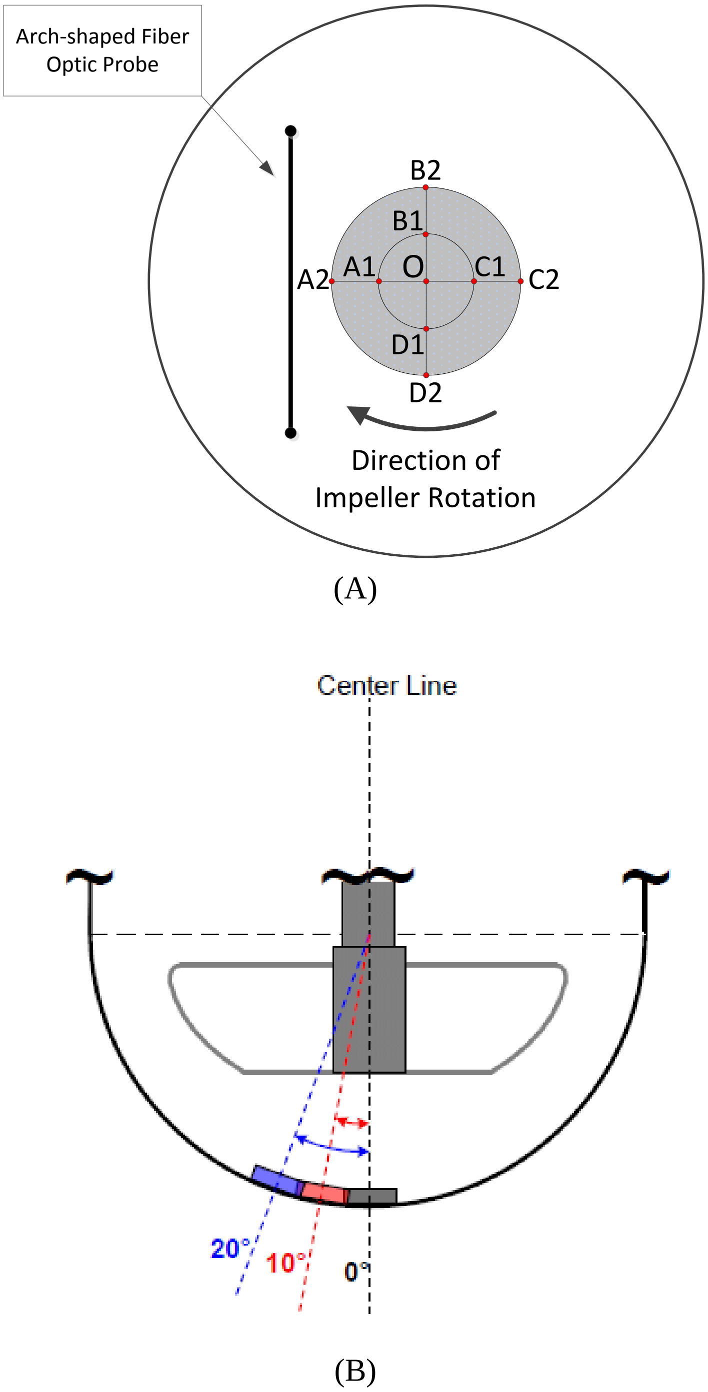

Figure 2.3 (A) Top view of the bottom of the dissolution vessel with the locations of the nine different tablet center positions used in the testing system; (B) Side view of the bottom of the dissolution vessel with three different tablet positions (0°, 10°, and 20°) in the standard system.

Tablets in Position O were at the center of the vessel bottom. Tablets in Positions A1, B1, C1, and D1 were on the inner circle 10 ° off center from the vessel vertical centerline. Tablets in Positions A1, B2, C2, and D2 were 20 ° off center on the same outer circle. Positions on the same circles were spaced 90 ° apart from one other. In each experiment, two tablets at the same positions were tested simultaneously in the two systems. After the vessels with the attached tablets were properly setup in the Distek system, 900 mL of deaerated buffered medium, previously preheated to 37.5 ℃, was poured gently along the vessel wall with the help of a plastic funnel to minimize gas introduction and to reduce dissolution of the tablet before the test started. Because of the heat loss during the liquid transfer into the vessels, the resulting buffer solution temperature was 37 ℃. Throughout the dissolution test, the temperature was maintained at 37 ℃ by the system temperature controller. The agitation at 100 rpm was started immediately after pouring the dissolution medium, the probe was inserted in the experimental system, and a stopwatch was started simultaneously. The first pair of samples was taken at this time ($t = 0$). Additional samples were collected at 5-min intervals for 45 min, as described above. Again, triplicate paired experiments were conducted for all positions.

Sample analysis was carried out using 1-cm quartz cells placed in a UV spectrophotometer (Cole Parmer S2100UV+; Cole Parmer, Vernon Hills, Illinois), measuring absorbance at 296 nm, specified for salicylic acid in USP. The cell was rinsed three times with the sample solution before it was filled with sample solution. Sample absorbance was converted to concentration using a calibration curve previously obtained by preparing standard solutions of different known concentrations. The absorbance vs. concentration calibration curve was linear ($R^2 = 0.9998$).

Data Analysis. The mass fraction of drug dissolved in the medium at any time t relative to initial total tablet drug amount, m_D/m_T, was calculated from the concentration data and plotted as a function of time. The amount of drug removed during sampling and not replaced was accounted for in the calculations.

The dissolution profiles for both systems with and without the probe were statistically compared using the paired Student's t-test equations to determine if the dissolution profiles were statistically similar to one other (null hypothesis). The corresponding t-test equations are as follows [45]:

$$\mathrm{T-value} = \frac{\overline{\mathrm{X_D}} - \mu_0}{\mathrm{S_D} - \sqrt{\mathrm{n'}}} \tag{2.1}$$

$$\mathrm{DF} = \mathrm{n'} - 1 \tag{2.2}$$

Where $\overline{X_D}$ is the sample mean (the average of the differences between curves at the same time t), μ_0 is the population mean (the average difference between the profiles; i.e., $\mu_0 = 0$ here if the null hypothesis is correct), S_D is the sample standard deviation (the standard deviation of the differences between curves), n′ is the number of samples (equal to 9 since each profile consisted of 10 points but the initial data point at t = 0 was not used), and DF is degrees of freedom (equal to 8 here). The T-value significance was chosen here to be 0.05 (i.e., if the T-value, P (t-test), was smaller than 5%, the null hypothesis was rejected), and the two groups of dissolution data (with and without the probe) were considered statistically different.

In addition, the similarity of the two dissolution profiles was also determined using the FDA-recommended approach consisting of a model-independent method based on the difference factor (f_1) and the similarity factor (f_2) proposed by Moore and Flanner [46]:

$$f_1 = \frac{\sum_{t=1}^{n} |R_t - T_t|}{\sum_{t=1}^{n} R_t} \times 100 \qquad (2.3)$$

$$f_2 = 50 \log_{10} \left\{ \left[1 + \left(\frac{1}{n} \right) \sum_{t=1}^{n} (R_t - T_t)^2 \right]^{-0.5} \times 100 \right\} \qquad (2.4)$$

Where R_t is the reference assay at time t (in this case the standard system), T_t is the test assay (in the probe system), and n is the number of samples. The value of f_1 was in the range 0–100. High f_1 values were associated with large average differences between the experimental and control profiles. The f_2 value was a logarithmic transformation of the sum-squared error of the differences between the dissolution curves. High f_2 values were associated with small average differences between the experimental and control profiles. Statistical similarity between the two curves required that $0< f_1 <15$ or $50 < f_2 <100$ [46, 47].

2.2.2 Flow Field Measurements

Particle Image Velocimetry (PIV). A Dantec FlowMap 1500 2D Particle Image Velocimetry (PIV) apparatus (Dantec Dynamics A/S, Tonsbakken 16-18, DK – 2740 Skovlunde, Denmark) was used to experimentally measure the flow field and velocity distribution on the selected 2D plane inside the vessels, as shown in Figure 2.4.

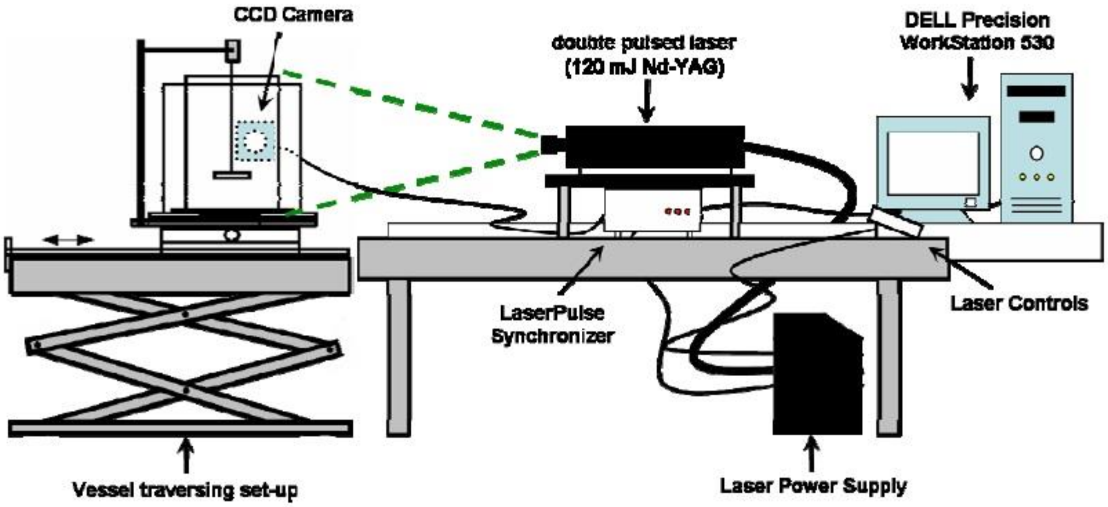

Figure 2.4 Schematic of laboratory PIV experimental set-up.

The PIV system consisted of a double pulsed 120 mJ Nd-Yag laser (New Wave Research model Solo 120 15 HZ, Fremont, CA, USA), a digital camera (Dantec Dynamics

HiSense PIV/PLIF camera model C4742-53-12NRB), a synchronizer (LASERPULSE Synchronizer, TSI model 610034), and a computer (DELL Precision WorkStation 530) for data acquisition and data analysis. The laser system consisted of two infrared laser heads combined in a single package with a second harmonic generator and two discrete power supplies. The laser source came from a Class IV laser, which emitted 532 nm wavelengths light. It produced two pulsed infrared laser beams which passed through an optical arrangement of lenses to generate a laser light sheet. The time between two pulses was a critical data acquisition parameter which was generally selected to suit the velocity of the flow field and the size of the interrogation area so there was no loss-of-pairs [48]. For a given measurement scenario, the higher the velocity the shorter the time between pulses. The laser light sheet was shot through the dissolution apparatus. The fluid in the apparatus was distilled water to which a very minute amount of seed particles had been added. The seed particles were silver-coated hollow borosilicate glass spheres (Dantec Measurement Technology USA, Mahwah, NJ, USA) with density of 1.4 g/cm^3 and size range from 2 to 20 μm (mean particle size 10 μm) and were used to follow the fluid flow and scatter the laser light for flow velocity measurement. The laser light scattered by the particles was captured by a CCD digital camera (PIVCAM 10-30, TSI model 630046) oriented perpendicularly with the laser light sheet. The laser and camera were connected to a synchronizer, which was connected to the computer where the software (FlowManager Software) was run to analyze the raw data and obtain the velocity values on the 2D plane.

The software collected pairs of digitized images from the CCD camera. These images were subdivided into small subsections called interrogation areas. Each pair of images for a given interrogation area was then analyzed using adaptive cross-correlation to determine the spacial x-displacement and y-displacement. The resulting fluid velocity in each interrogation area was obtained by dividing the x- and y-displacements by the time interval between the two images.

Velocity distribution in both the testing system and standard system were measured by PIV. In each experiment, the vessel was placed in a square Plexiglas tank filled with water in order to minimize the refractive effects at the curved surface of the vessel wall during the PIV measurements. A small amount of seed particles was added to the liquid (water) in the vessel under investigation and two pairs of images were taken at a time interval of 1 ms. Because the laser light sheet was blocked by the shaft, only half of the cross section of the vessel could be illuminated. For the standard system, which was a symmetric system, it was assumed that the hydrodynamics of medium flowing was the same on each cross section of the vessel. Therefore, the velocity map on only one cross plane needed to be measured. However, the testing system had a probe on only one side of the vessel and was therefore asymmetrical. Thus, four lengthwise cross-sections of the testing system were measured. For each section, three repeated experiments were conducted. The cross sections chosen to be measured in this work are shown in Figure 2.5.

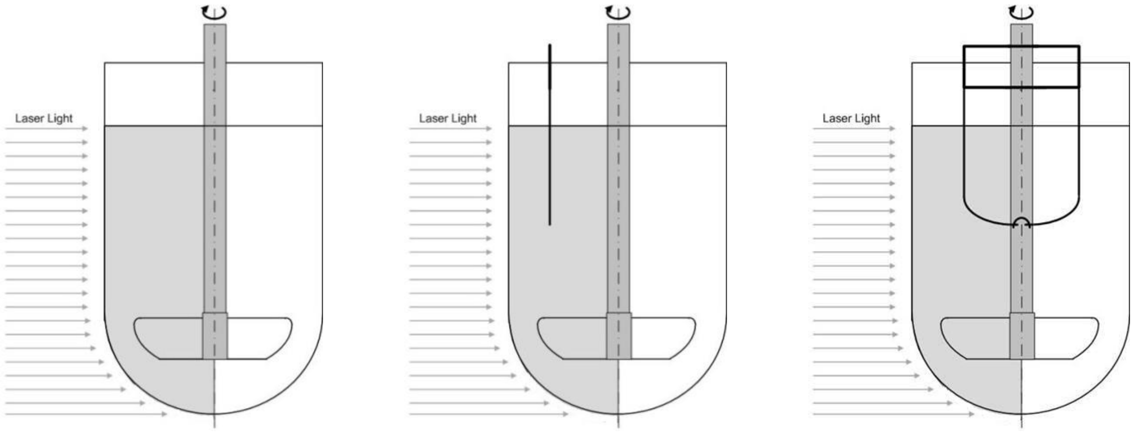

Without Probe With Probe-Section A With Probe-Section B

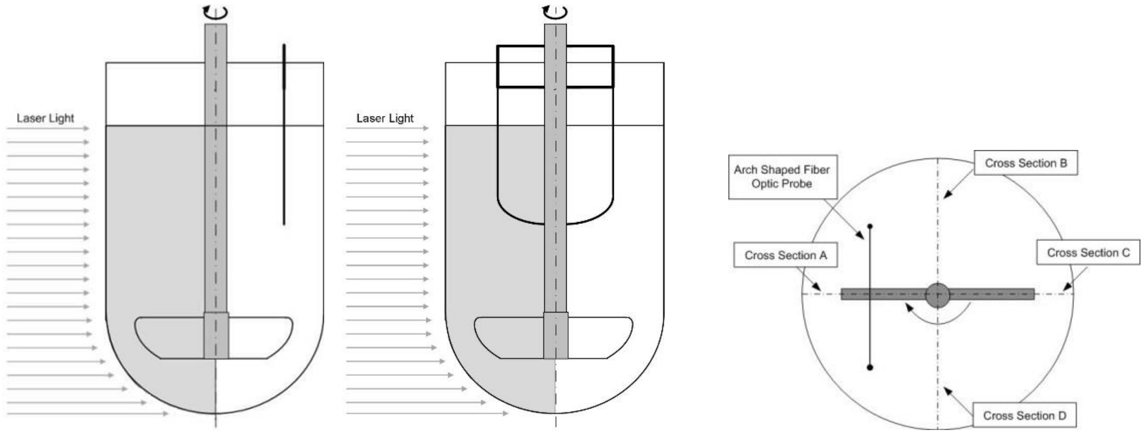

With Probe-Section C With Probe-Section D

Figure 2.5 Four cross sections of PIV measurements.

In order to fully quantify the fluid flow in the dissolution apparatus, six horizontal surfaces (iso-surfaces) were selected inside the vessel, as shown in Figure 2.6. The lowest point in the bottom of the vessel was defined as Y=0 mm. The vessel was separated into three regions, i.e., above the impeller, around the impeller, and below the impeller. Two of the iso-surfaces were located above the impeller, i.e., at Y=106mm, and at the bottom of the probe, i.e., at Y=94mm. One iso-surfaces was in the impeller region, i.e., the upper edge of the shaft, i.e., Y=44mm. The other iso-surfaces where below the impeller, i.e., Y=19mm, Y=13mm and Y=7mm. In this 2D experiment, three repeated experiments were conducted for each section; the average radial and axial velocities on each iso-surface were calculated, plotted and analyzed. In this 2D PIV experiment, the radial and axial velocities on the whole cross section could be obtained, which were shown in the velocity vector map. For each iso-surface, the radial velocity and axial velocity were divided by the tip velocity to be scaled, plotted and compared with the simulation results.

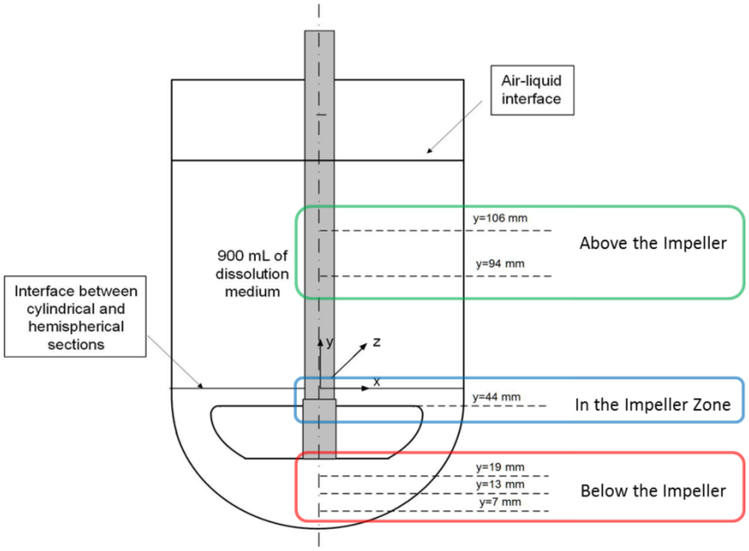

Figure 2.6 Iso-surface lines inside the USP 2 dissolution vessel.

2.3 Hydrodynamic Simulation via Computational Fluid Dynamics (CFD)

2.3.1 Computational Fluid Dynamics Approach

CFD is a branch of fluid mechanics using mathematical equations and numerical analysis to study fluid flow, heat transfer, chemical reactions, etc. One of the earliest CFD calculations using finite differences and divided the physical space in cells was developed from the pioneering accomplishments of enthusiasts such as Richardson (1910) and Courant, Friedrichs, and Lewy [49]. Along with the computer science fast paced improved, the CFD as a developing science, received much more attention. Since the late 1960s, there were considerable growth in study of CFD and application to number of industry fields, such as aerospace, combustion, mechanical, oceanic flows, stirred mixing process, etc. [50].

Compared to experimental method, CFD simulation has many advantages [54]. The great advantage of CFD method is the saving of time, human labor, and space room cost associated with experimental method. It is particularly useful when the experiment can't be adopted because of limit conditions or unavailable conditions, such as measurements the variables of everywhere in the sealed pipe, or dangerous environment in an oven. Furthermore, it is suitable for the new equipment or process developing stage. In addition, CFD can provide answers for "what if" questions in a shorter time and save significant cost compared to conducting experiments.

In recent years, CFD has been commonly used to analyze the performance of basic equipment in industry, such as stirred tanks [51], spray dryers [52], heat exchangers [53] and some other equipment. Since CFD can give a full general prediction in hydrodynamics, heat transfer, mass transfer, phase change (such as in freezing, melting or boiling), chemical reaction, and mechanical movement (such as an impeller turning, pistons, fans or rudders), it has become an integral part of process design, geometry change and equipment modification in many companies. It is easier to do comparison through the CFD results and obtain the optimized conditions or modified equipment which has improved performance, more confident scale-up, or improved product quality [55].

The CFD simulation can be performed through CFD software in computer. The simulation process includes three major tasks consisting of pre-processing, processing/solving, and post-processing. During the first stage, pre-processing, the problem at hand is conceptualized and the physics of the problem is analyzed. Then structure geometry can be set up and mesh can be defined. Specialized CFD software, such as GAMBIT software, can help define the object shape and create the mesh simultaneously. In the processing step, the simulation is started, and the relevant conservation equation are discretized, and solved for each of the hundreds of thousands of cell in which the control volume is divided. This step is time-consuming process and will stop when an acceptable convergence is achieved. In the last step, the model should be already solved, and the results can be analyzed, exported, and compared. This last task can provide the visualization of 2D or 3D graphs of the velocity field and contour plots of other scalar variables such as temperature, concentration, pressure, etc.

In this work, the CFD package Fluent (version 6.3.26) was used to simulate the 3D hydrodynamics of USP Dissolution Testing Apparatus 2. The geometry model was constructed in the commercial mesh generator Gambit 2.4.6. This simulation can predict the flow field in both of the standard system and the testing system in order to compare the

CFD predictions with the PIV measurements.

2.3.2 Mesh

The physical models for the two systems were constructed in Gambit software to generate a mesh to define the computational cells used in the simulation. For the standard system, an unstructured tetrahedral mesh was created in the whole vessel as shown in Figure 2.7. The mesh typically contained 1,676,834 cells, and 293,543 nodes. The average EquiSize Skew parameter ranged from 0.3 to 0.4, and the worst element quality was 0.77 (the lower this number, the higher the quality of the mesh for the processing step). This implied that the standard USP Apparatus 2 system had a high mesh quality, which had a significant impact on the quality of the solution.

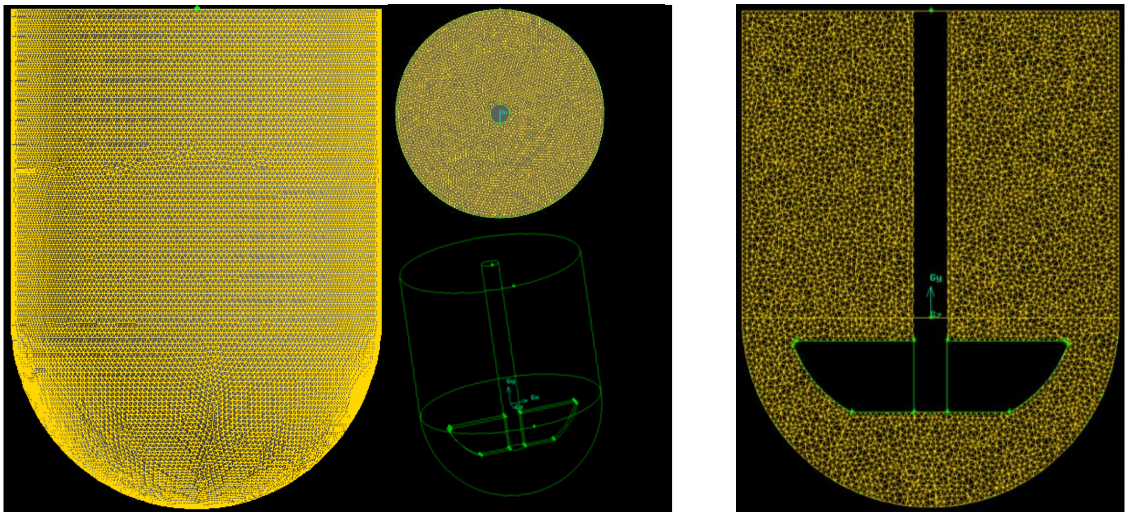

Figure 2.7 Mesh structure of standard system generated by GAMBIT software.

The testing system shown in Figure 2.8 contains the probe on one side of the vessel and is therefore asymmetric. The mesh for this system was similar to the previous one, except for the presence of the probe (and the mesh refinement around it) and the use of the two domains described above. The mesh typically contained 2,342,163 cells and 467,601 nodes. The average EquiSize Skew parameter ranged from 0.3 to 0.4, and the largest value was 0.81 for an individual cell. The physical models for both of the two systems were used as input in the FLUENT software.

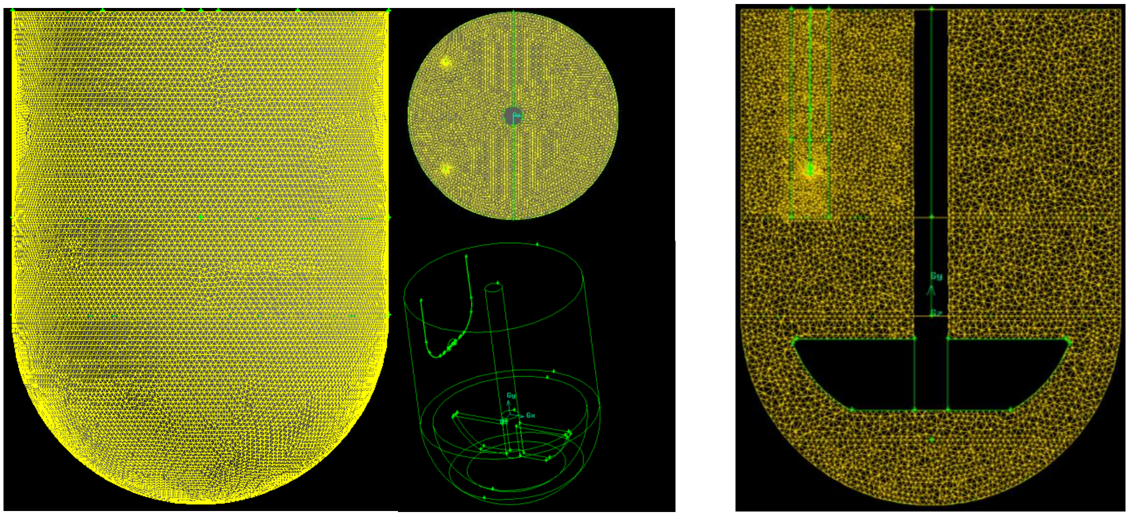

Figure 2.8 Mesh structure of testing system generated by GAMBIT software.

The flow field inside the vessel was obtained by solving appropriate conservation equations in each cell, i.e., the Navier-Stokes equation and the mass conservation equations. In Cartesian coordinates, the continuity equation for an incompressible fluid can be written in Equation 2.5:

$$\frac{\partial u_i}{\partial x_i} = 0 \tag{2.5}$$

Similarly, conservation of momentum (Navier-Stokes equation) used for turbulent flow calculation can be written as in Equation 2.6:

$$\frac{\partial u_i}{\partial \mathrm{t}} + \frac{\partial u_i u_j}{\partial x_j} = -\frac{1}{\rho}\frac{\partial P}{\partial x_i} + \nu \nabla^2 u_i + g_i \tag{2.6}$$

2.3.3 Turbulence Modeling

The fluid flow in USP 2 system is turbulent. Therefore, a turbulence model must be incorporated in the CFD simulations. Turbulent flows are characterized by fluctuating velocity fields. These fluctuations transport quantities such as momentum, energy, and species concentration, and cause the transported quantities to fluctuate as well. Since these fluctuations can be of small scale and high frequency, direct turbulence simulation is too computationally expensive in practical engineering applications. Instead, the instantaneous (exact) governing equations can be time-averaged, ensemble-averaged, or otherwise manipulated to remove the turbulent component, resulting in a modified set of equations that are computationally less expensive to solve. Two alternative methods can be employed to transform the Navier-Stokes equations in such a way that the small-scale turbulent fluctuations do not have to be directly simulated: Reynolds averaging and filtering. The Reynolds-averaged Navier-Stokes (RANS) equations represent transport equations for the mean flow quantities only, with all the scales of the turbulence being modeled. The Reynolds-averaged approach is generally adopted for practical engineering calculations, and uses models such as Spalart-Allmaras, k-ε and its variants, k-ω and its variants, and the RSM. Another alternative approach as mentioned above is called LES, which used a set of “filtered” equations to compute the large eddies. “Filtering” is essentially a manipulation of the exact Navier-Stokes equations to remove only the eddies that are smaller than the size of the filter, which is usually taken as the mesh size. However, because typical applications are simple geometries, and LES needs large computer resources and high-order spatial discretization, the conventional turbulence models commonly modeled by Reynolds - averaged approach.

In the Reynolds-averaged method, the velocity component in the instantaneous (exact) Navier-Stokes equations can be taken into the mean (time-averaged) and fluctuating components as:

$$u_i = \bar{u}_i + u_i' \tag{2.7}$$

Where $\bar{u}_i$ and u_i' are the mean and fluctuating velocity components (i = 1, 2, 3). Substituting the velocity expressions in this form into the instantaneous continuity and momentum equations and taking a time average yields the Reynolds-averaged Navier-Stokes (RANS) equations. For an incompressible fluid, they can be written in Cartesian tensor form as:

$$\frac{\partial \bar{u}_i}{\partial x_i} = 0 \tag{2.8}$$

$$\frac{\partial \bar{u}_i}{\partial t} + \bar{u}_j \frac{\partial \bar{u}_i}{\partial x_j} = -\frac{1}{\rho}\frac{\partial \bar{P}}{\partial x_i} + \nu \nabla^2 \bar{u}_i + g_i - \frac{\partial}{\partial x_j}\left(\overline{u_i' u_j'}\right) \tag{2.9}$$

The first three terms on the right side of this equation represents, respectively, the pressure forces, viscous transport and body forces (such as gravity). And the last term represents the Reynolds stresses, consisted of velocity fluctuating components. These

Reynolds stresses should be modeled by the mathematical approach including the Boussinesq hypothesis in order to close and solve the Equation 2.6; therefore, one or two transport equations are added to solve the turbulent viscosity in the case of turbulent model.

It is an unfortunate fact that no single turbulence model can be superior for all classes of problems. The choice of turbulence model depends on the physics property of the flow, the level of accuracy required, the available computational resources, and the amount of time available for the simulation, etc. For the simulation for USP 2 system in this work, the nature of the flow and the computing resources on hand should be considered in order to choose an appropriate turbulence model. FLUENT software provided different turbulence models, i.e., the k-ω model with low Reynolds number correction, RNG k-ε model, and Realizable k-ε model [56, 57], or with no turbulence model at all, i.e., assuming laminar flow. The flow inside both the standard USP 2 system and testing system with probe are typically turbulent, and the k-ε model and k-ω model can be used in the simulations. In previous work by this group [6], it was shown that using the k-ω model with low Reynolds number correction produced velocity predictions that were in closer agreement with the experimental data. Therefore, the k-ω model was used in this work.

Standard k-ε Model. The standard k-ε model is a semi-empirical model based on model transport equations for the turbulence kinetic energy k and its dissipation rate ε. In the derivation of the standard k-ε model, it is assumed that the flow is fully turbulent, and the effects of molecular viscosity are negligible. The standard k-ε model is, therefore, valid only for fully turbulent flows. Its main advantages are that it is robust and computationally economical. The main disadvantage of this model is the assumption that fluctuating velocities are isotropic. In the derivation of the k-ε model, it was assumed that the flow is fully turbulent, and the effects of molecular viscosity are negligible. The standard k-ε model is therefore valid only for fully turbulent flows. The governing transport equations for the standard k-ε model are:

$$\frac{\partial k}{\partial t} + \bar{u}_i \frac{\partial k}{\partial x_i} = \frac{\partial}{\partial x_i}\left(\frac{\nu_t}{\sigma_k}\frac{\partial k}{\partial x_i}\right) + \nu_t\left(\frac{\partial \bar{u}_i}{\partial x_j} + \frac{\partial \bar{u}_j}{\partial x_i}\right)\frac{\partial \bar{u}_i}{\partial x_j} - \varepsilon \tag{2.10}$$

$$\frac{\partial \varepsilon}{\partial \mathrm{t}} + \bar{u}_i \frac{\partial \varepsilon}{\partial x_i} = \frac{\partial}{\partial x_j}\left(\frac{\nu_t}{\sigma_\varepsilon}\frac{\partial \varepsilon}{\partial x_i}\right) + C_{1\varepsilon}\frac{\varepsilon}{k}G - C_{2\varepsilon}\frac{\varepsilon^2}{k} \tag{2.11}$$

Where G is the generation of k and is given by:

$$G = \nu_t\left(\frac{\partial \bar{u}_i}{\partial x_i} + \frac{\partial \bar{u}_j}{\partial x_i}\right)\frac{\partial \bar{u}_i}{\partial x_j} \tag{2.12}$$

The turbulent viscosity is then related to k and ε by the expression:

$$\nu_t = C_\mu \frac{k^2}{\varepsilon} \tag{2.13}$$

The coefficients C_μ, $C_{1\varepsilon}$, $C_{2\varepsilon}$, σ_k, σ_ε are constants which have the empirically derived values of 0.09, 1.44, 1.92, 1.0 and 1.3 [58].

k-ω Turbulence Model with Low-Reynolds-Number Correction. The standard k-ω model is an empirical model based on model transport equations for the turbulence kinetic energy (k) and the specific dissipation rate (ω), which can also be thought of as the ratio of ε to k. The standard k-ω model was first introduced by Wilcox [56]. The k-ω model has been modified over the years, production terms have been added to both the k and ω equations, which have improved the accuracy of the model for predicting free shear flows. It has lower sensitivity to boundary conditions. It has good performance for free shear and low Reynolds number flows [59]. The governing equations for the standard k-ω model are:

$$\frac{\partial}{\partial t}(\rho k) + \frac{\partial}{\partial x_i}(\rho k u_i) = \frac{\partial}{\partial x_j}\left(\Gamma_k \frac{\partial k}{\partial x_j}\right) + G_k - Y_k \tag{2.14}$$

$$\frac{\partial}{\partial t}(\rho \omega) + \frac{\partial}{\partial x_i}(\rho \omega u_i) = \frac{\partial}{\partial x_j}\left(\Gamma_\omega \frac{\partial \omega}{\partial x_j}\right) + G_\omega - Y_\omega \tag{2.15}$$

Where, the term G_k represents the generation of turbulence kinetic energy due to mean velocity gradients. G_ω represents the generation of ω. Γ_k and Γ_ω respectively represent the effective diffusivity of k and ω. Y_k and Y_ω are the dissipation of k and ω due to turbulence.

$$\mathit{\Gamma}_k = \mu + \frac{\mu_t}{\sigma_k} \tag{2.16}$$

$$\Gamma_\omega = \mu + \frac{\mu_t}{\sigma_\omega} \tag{2.17}$$

Where (σ_k and σ_ω are the turbulent Prandtl numbers for k and ω. The turbulent viscosity, μ_t , is computed by combining k and ω as follows:

$$\mu_t = \alpha^* \frac{\rho k}{\omega} \tag{2.18}$$

The k-ω model with low-Reynolds-number Correction is from a modification of the standard k-ω model by defining a different form of $\alpha*$. The coefficient $\alpha*$ damps the turbulent viscosity causing a low-Reynolds-number correction. It is given by:

$$\alpha^* = \alpha_\infty^* \left(\frac{\alpha_0^* + Re_t/R_k}{1 + Re_t/R_k} \right) \tag{2.19}$$

In the standard *k*-*ω* model, $\alpha^* = \alpha^*_\infty = 1$. The *k*-*ω* turbulence model with low-Reynolds-number correction is more appropriate than the standard *k*-*ω* model when predicting transitional flow. However, good convergence cannot be easily achieved by using *k*-*ω* models. Under relaxation parameters need to be adjusted carefully to get well converged simulation results.

2.3.4 Reference Frame Method

A single reference frame (SRF) model was used for simulations with the standard USP 2 system. Since the standard system is a symmetric system with only impeller inside vessel is in the center of the vessel, the momentum equations for the entire domain (i.e., representing the whole fluid inside the vessel) can be solved in a single rotating frame. The approach consists of using a frame of reference rotating with the impeller in which the impeller is assumed to be at rest in this frame of reference, while the vessel wall is assumed to be rotating, as shown in Figure 2.9. In order to represent correctly the flow in the real system (where the impeller is actually rotating), the simulations must include the non-inertial forces appearing in the rotating frame of reference.

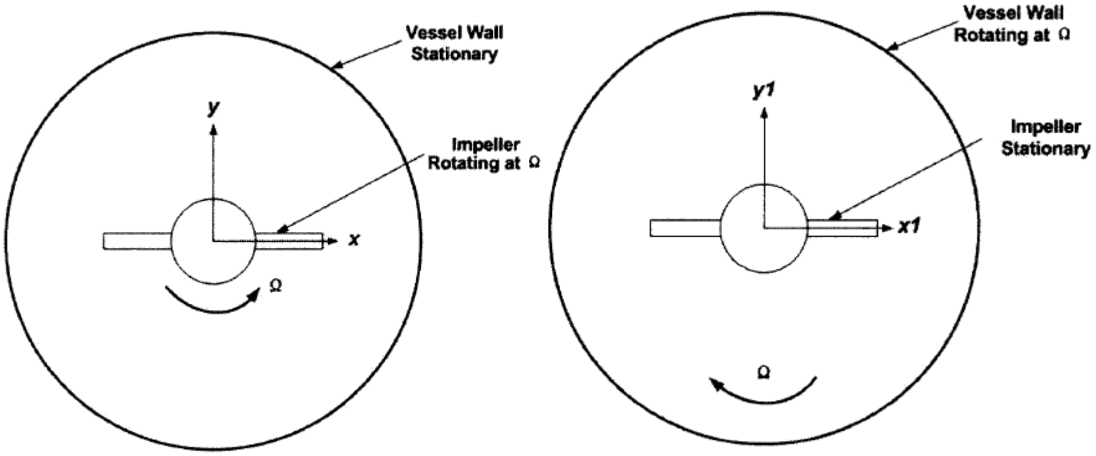

(A) (B)

Figure 2.9 Transforming coordinates from absolute frame to a rotating reference frame, top view. (A) Original reference frame. (B) Rotating reference frame.

When the equations of motion are solved in a rotating reference frame, the acceleration of the fluid is augmented by additional terms that appear in the momentum equations [60]. The absolute velocity $\vec{v}$ and the relative velocity in the reference frame are related by the following equation:

$$\vec{v}_r = \vec{v} - \left(\vec{\Omega} \times \vec{r}\right) \tag{2.20}$$

Where, $\vec{\Omega}$ and $\vec{\mathrm{r}}$ are the angular velocity vector and the position of the vector in the rotating reference frame respectively. The left-hand side of the momentum equations appears as follows for an inertial reference frame:

$$\frac{\partial}{\partial t}(\rho\vec{v}) + \nabla\cdot(\rho\vec{v}\vec{v}) \tag{2.21}$$

For a rotating reference frame, the left-hand side written in terms of absolute velocities becomes:

$$\frac{\partial}{\partial t}(\rho\vec{v}) + \nabla\cdot(\rho\vec{v}_r\vec{v}) + \rho\left(\vec{\Omega}\times\vec{v}\right) \tag{2.22}$$

In terms of relative velocities the left-hand side becomes:

$$\frac{\partial}{\partial t}(\rho\vec{v}_r) + \nabla\cdot(\rho\vec{v}_r\vec{v}_r) + \rho\left(2\vec{\Omega}\times\vec{v}_r + \vec{\Omega}\times\vec{\Omega}\times\vec{\mathrm{r}}\right) + \rho\frac{\partial\vec{\Omega}}{\partial t}\times\vec{\mathrm{r}} \tag{2.23}$$

Unfortunately, the SRF approach cannot be used in simulations for systems that are asymmetric, such as the testing system in this work, which has a probe on one side of impeller. In this case, the SRF method cannot be used because the probe is not moving with the rotating fluid. The hydrodynamics in this asymmetric system can be simulated in CFD using a number of approaches. The least computationally intensive is the Multiple

Reference Frames (MRF) method. Accordingly, the liquid volume inside the testing system is partitioned between two domains: an inner domain including the paddle, and an outer domain comprising the other region, i.e., the probe and the liquid volume between the inner domain and the vessel wall, as shown in Figure 2.10.

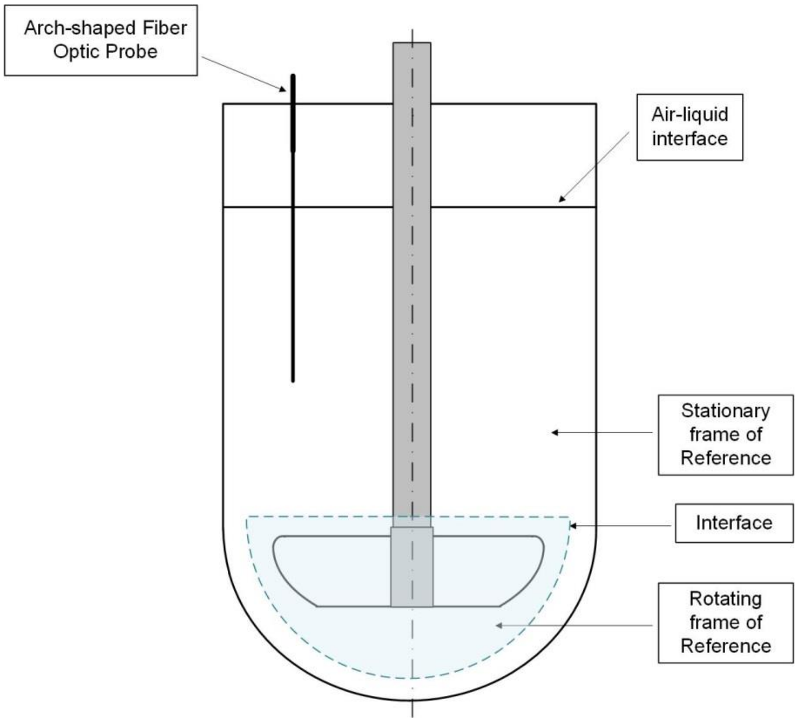

(B)

Figure 2.10 The MRF model used in this work for the simulation of USP 2 system with probe.

As for the impeller shaft (except for the paddle), it was difficult to include it in the inner domain since this domain could not be easily extended to the top portion of the vessel because of the presence of the probe. Therefore, the shaft was simulated by assigning a fixed rotating velocity to its surface. The MRF approach is a steady-state approximation in which the flow in the computational cells in the inner rotating domain is solved using the moving reference frame equations (including the non-inertial terms), and the flow in the cells in the stationary domain is solved with the appropriate stationary equations. At the interface between the domains, the flow in one zone is used to determine the fluxes at the boundary of the other zone. The MRF approach can be used as long as the interaction between the two zones is relatively weak, since each zone appears “frozen” with respect to the other one, although one zone is actually rotating and the other is not.

2.3.5 Boundary Conditions

In the simulations for the two systems, the boundary conditions were as following: the no-slip condition was assumed at all solid surfaces; the air-water interface was assumed to be flat, and was modeled as a frictionless surface, i.e., the normal gradients of all variables were zero at this interface. In the previous work of this group, the liquid level at the vessel top was measured when the liquid was rotating and compared with that when the liquid was at rest. It showed that the liquid level at the shaft dropped closely to 0mm when the rotating speed was 100rpm. This observation additionally implies that the boundary condition used in the simulations, i.e., that the liquid level was flat, is indeed appropriate.

2.4 Results of Dissolution Testing Experiments

2.4.1 Dissolution Profiles for Dropped Tablets

The dissolution profiles obtained using USP procedure in which the tablets were dropped in the vessel at the beginning of the experiment are shown in Figure 2.11. The percentage drug release was systematically higher in the system with the probe than in the standard system without the probe, although the difference was typically only about 1%. At t=45 minutes, the m_D/m_T ratio was 30.4% with the probe and 29.3% without the probe. The average standard deviations were 0.82% and 0.36%, respectively. The f_1 and f_2 values were equal to 5.64 and 93.22, respectively, i.e., within the FDA requirement (Table 2.1). However, the P (t-test) value was 0.00007, which was significantly lower than 0.05, indicating that the two dissolution profiles were statistically different, although the difference between them was small.

Table 2.1 Probability Associated with Paired T-test (P (T-test)), Difference Factor (f_1), and Similarity Factor (f_2), for Average Dissolution Profiles (Drug Release Mass Ratio, m_D/m_T, vs. Time) Obtained With and Without the Fiber Optic Probe

Tablet Position	Tablet Off-Center Angle	P (t-test)	Difference Factor (f_1)	Similarity Factor (f_2)
Dropped Tablet	USP Procedure	0.00007	5.64	93.22
O	0 °	0.00021	8.91	90.27
A1	10 °	0.00030	14.92	78.08
B1	10 °	0.00186	11.53	80.54
C1	10 °	0.00067	10.16	85.39
D1	10 °	0.53083	1.11	99.12
A2	20 °	0.00038	13.17	77.55
B2	20 °	0.00335	3.64	94.54
C2	20 °	0.00071	1.66	98.70
D2	20 °	0.00511	1.93	93.22

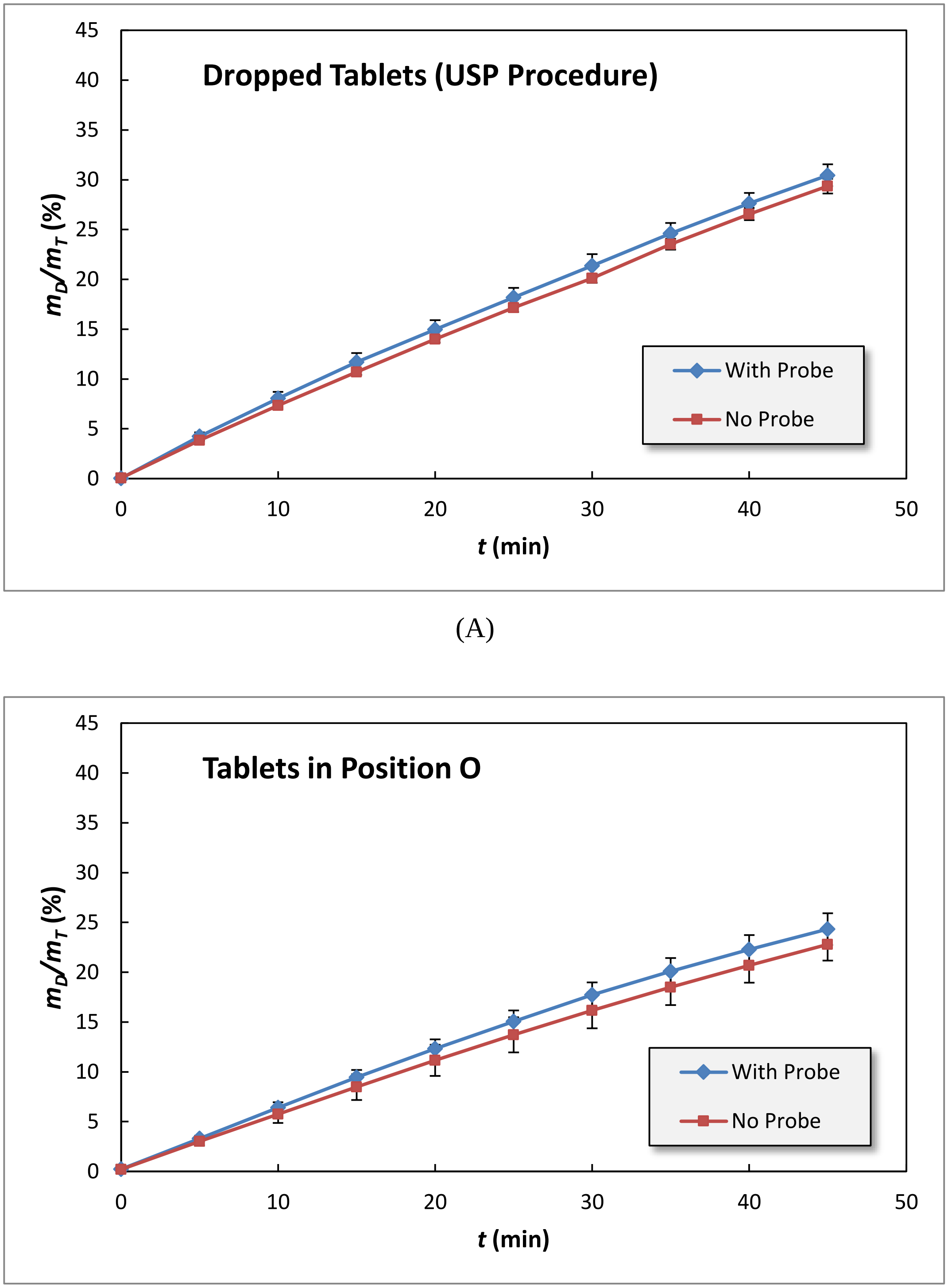

(A)

(B)

Figure 2.11 Dissolution profiles for experiments in the presence and absence of the fiber optic probe with: (A) Tablets dropped according to USP procedure; and (B) Tablets in Position O.

2.4.2 Dissolution Profiles for Centrally Positioned Tablets

The dissolution profiles for tablets fixed at the center of the vessel bottom (Position O) are presented in Figure 2.11. Also for this case, the percentage of dissolved drug was higher in the system with the probe throughout the whole experiment (average difference $\cong$ 1.5%). The final difference in drug released at 45 minutes was close to 2%. The average standard deviations for each profile were 0.93% and 1.29%, respectively. The results of the t-test (P (t-test) = 0.00021; Table 2.1) indicated that the two curves came from different populations, although the f_1 and f_2 values were 8.91 and 90.27, respectively, both of which are in the recommended FDA range.

2.4.3 Dissolution Profiles for 10 ° Off-center Tablets

The dissolution curves for tablets in the four positions on the 10 ° off-center circle (i.e., Positions A1, B1, C1 and D1) are shown in the top panels in Figure 2.12 and Figure 2.13. The m_D/m_T profiles for these four positions were always higher than for Position O (centered position), irrespective of the presence of the probe. Typically, m_D/m_T was about 28-31% for the 10 ° off-center tablets while it was 22-24% for the centered tablet. Figures 2.12 and 2.13 show that the presence of the probe resulted in dissolution profiles that were appreciably different from the corresponding profiles obtained without the probe. However, the magnitude of the difference between the curves in each panel depended on tablet position. The dissolution curves were independent of the presence of the probe only for the tablet positions just before the probe (Position D1).

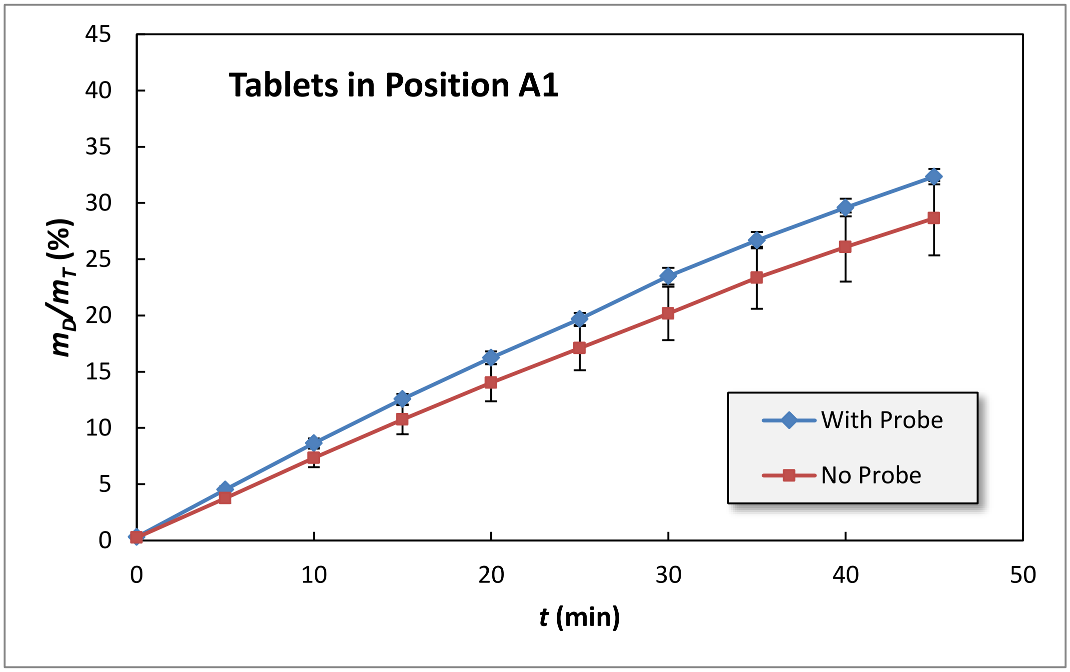

(A)

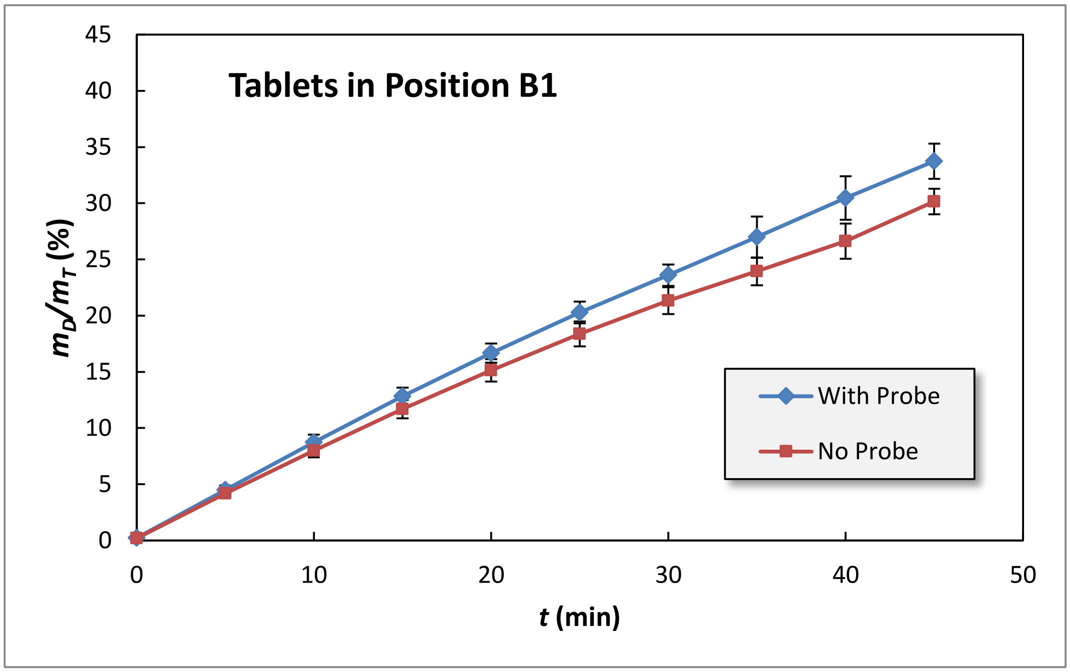

(B)

Figure 2.12 Dissolution profiles for experiments in the presence and absence of the fiber optic probe with: (A) Tablets in Position A1; and (B) Tablets in Position B1.

The dissolution curves for tablets in Position A1 were consistently higher when the probe was present than when it was not, with average differences of about 3-4% (Figures 2.12). This is consistent with the fact that this position is immediately downstream of the first vertical element of the probe and the closest to the probe. The values of the P (t-test) (=0.00030), f_1 and f_2 reinforced this observation. In particular, the f_1 value (14.92) was found to be very close to 15, the upper limit for acceptance (Table 2.1). Position B2, immediately downstream of the whole probe, was the second position most significantly affected by the probe for tablets on the 10 ° circle. The presence of the probe resulted in faster dissolution rates, with differences between the curves on the order of 3-4% and values of P (t-test), f_1 and f_2 consistent with this effect (Table 2.1). Tablets in Position C1, on the other side of the probe, were less affected by the probe, as shown in Figure 2.13 (A) and by the values of f_1 and f_2. Finally Tablets in Position D1, the most downstream with respect to the probe, were nearly unaffected by the presence of the probe. This was confirmed by the large value of the P (t-test) ($>>0.5$), the very small value of f_1, and large value of f_2 (Table 2.1). In fact, the two curves in Figure 2.13 (B) are nearly superimposed on each other.

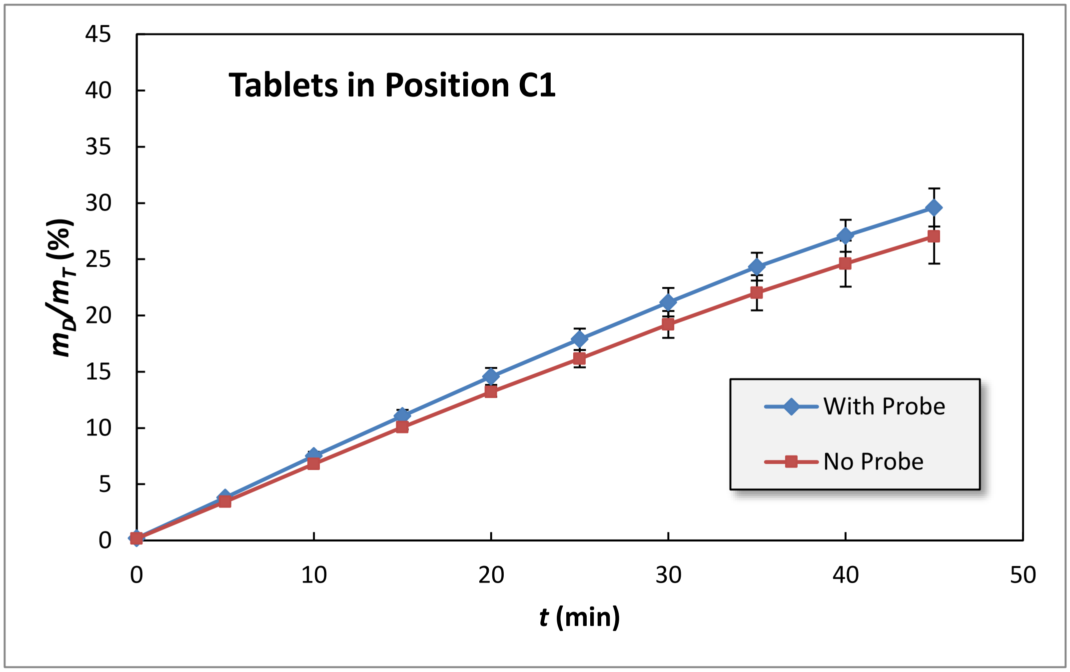

(A)

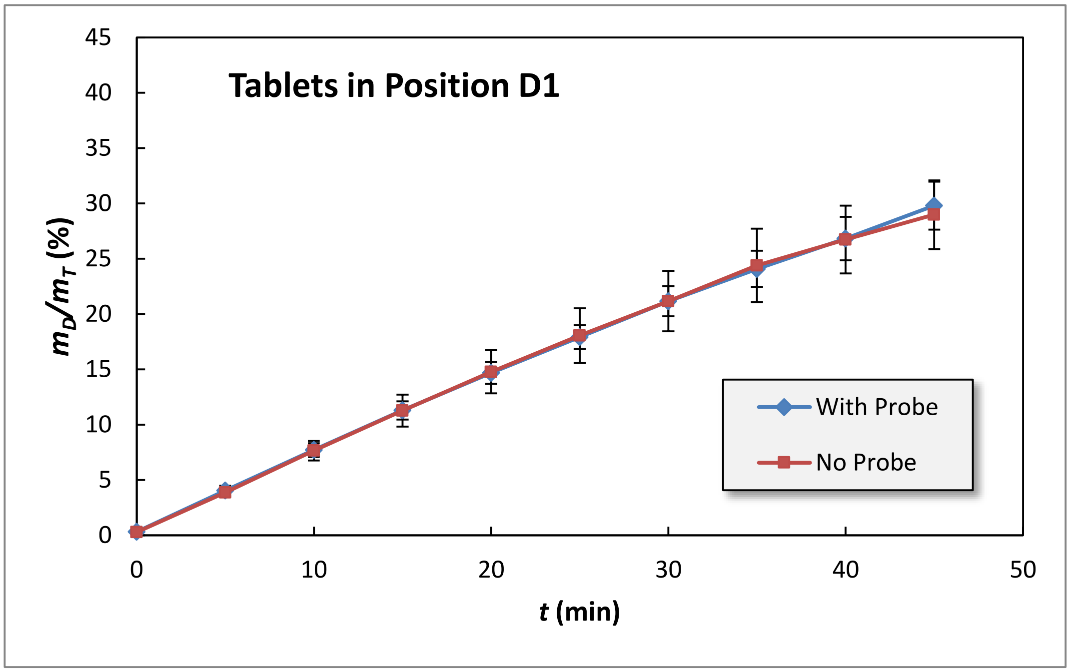

(B)

Figure 2.13 Dissolution profiles for experiments in the presence and absence of the fiber optic probe with: (A) Tablets in Position C1; and (B) Tablets in Position D1.

The results for all of the four positions can be explained by the concept that the turbulence effects generated by the rotating fluid as it moves past the probe propagates tangentially, i.e., downstream of the probe. This hydrodynamics effect was large for Position A1 since it was the first position downstream of the probe and the closest one. This turbulence effect propagated downstream (tangentially), but with decreasing intensity, through Position B1, and Position C1. When these disturbances reached Position D1, they had little impact on dissolution. This effect can be clearly seen by examining Figure 2.12 and Figure 2.13, as well by observing the decreasing values of the f_1 value and increasing value of f_2 (Table 2.1) as one moves tangentially and clockwise with the flow (Figure 2.3).

2.4.4 Dissolution Profiles for 20 ° Off-center Tablets

The dissolution profiles for the four positions (i.e., Position A2, B2, C2 and D2) on 20 ° off-center circle are shown in Figure 2.14 and Figure 2.15. The difference between dissolution profiles was larger for Position A2 (3-4%) than for any other position downstream. No significant difference could be observed for Positions B2, C2 and D2. In some of these runs, the dissolution curves for the systems with the probe were identical or even lower than those without the probe.

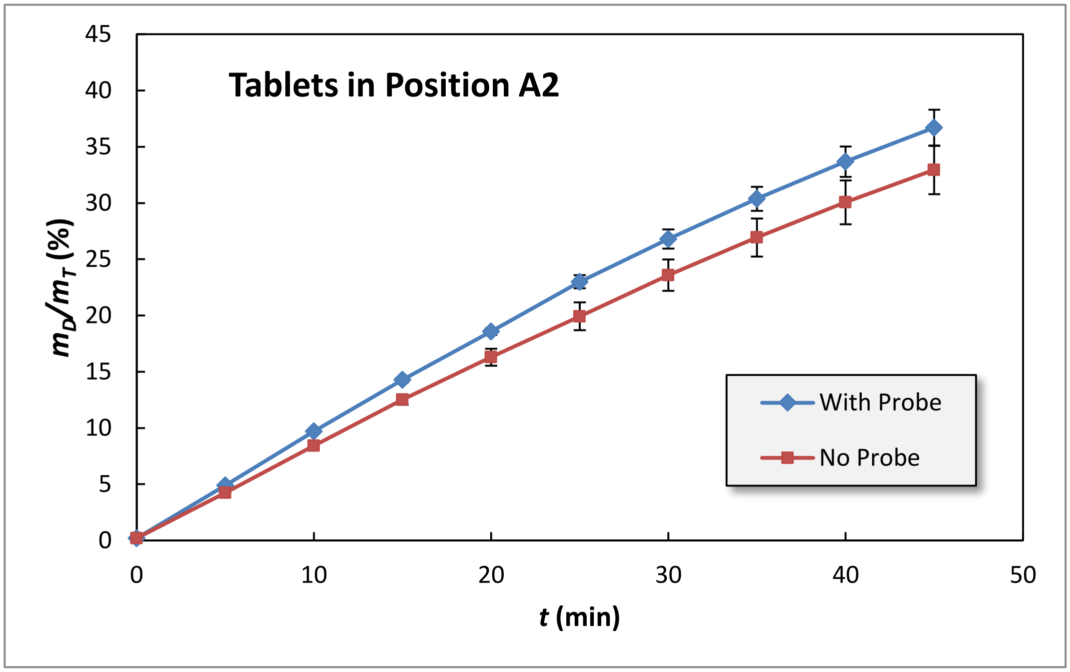

(A)

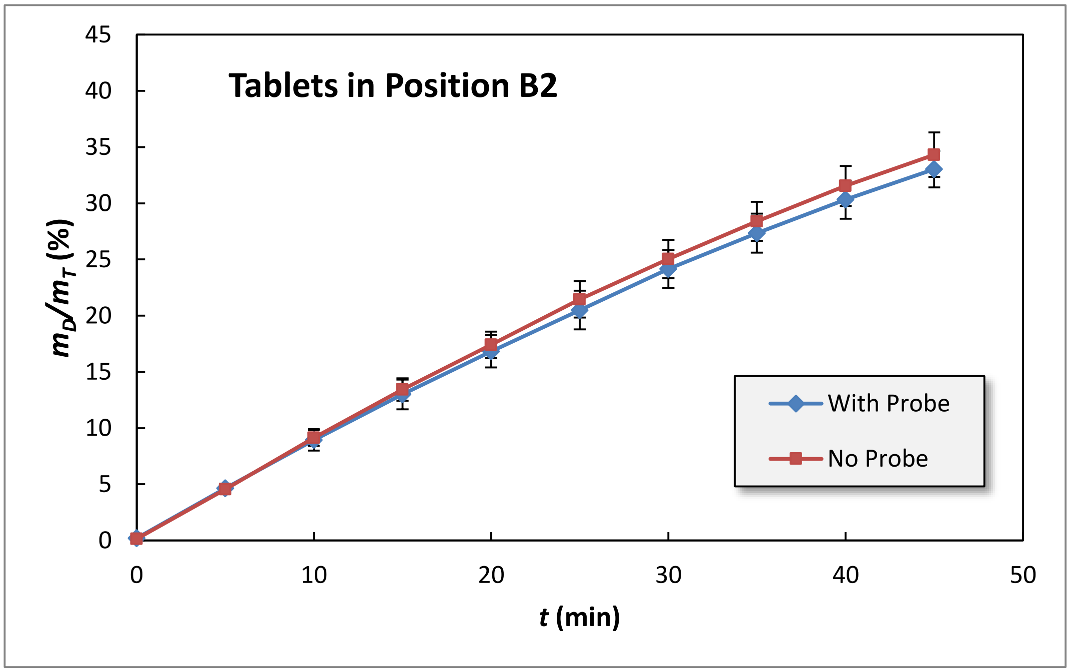

(B)

Figure 2.14 Dissolution profiles for experiments in the presence and absence of the fiber optic probe with: (A) Tablets in Position A2; and (B) Tablets in Position B2.

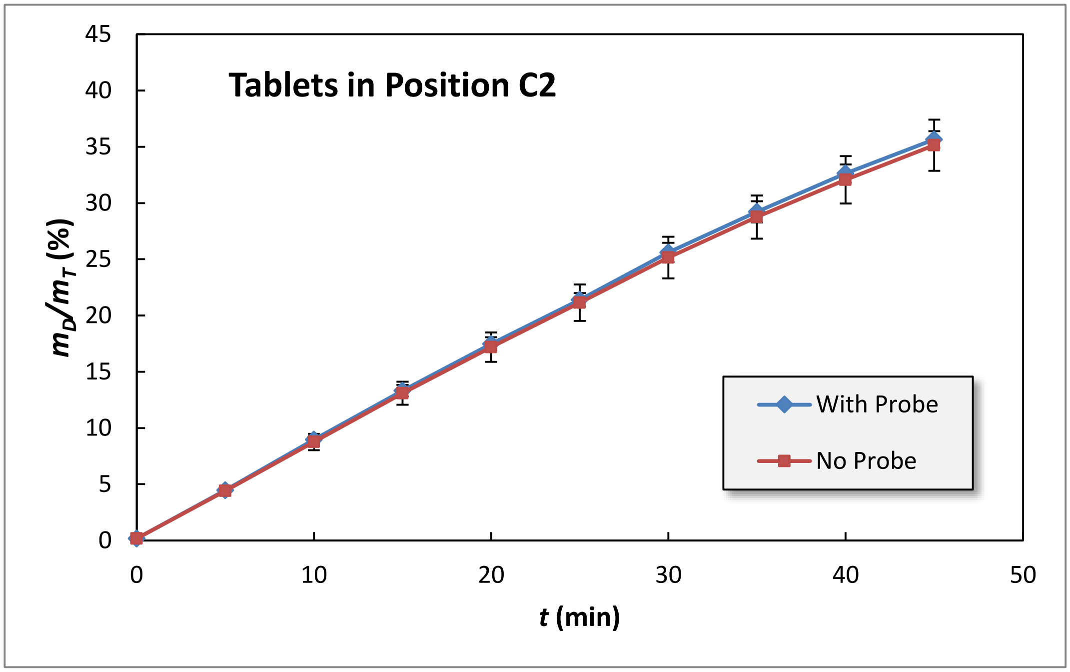

(A)

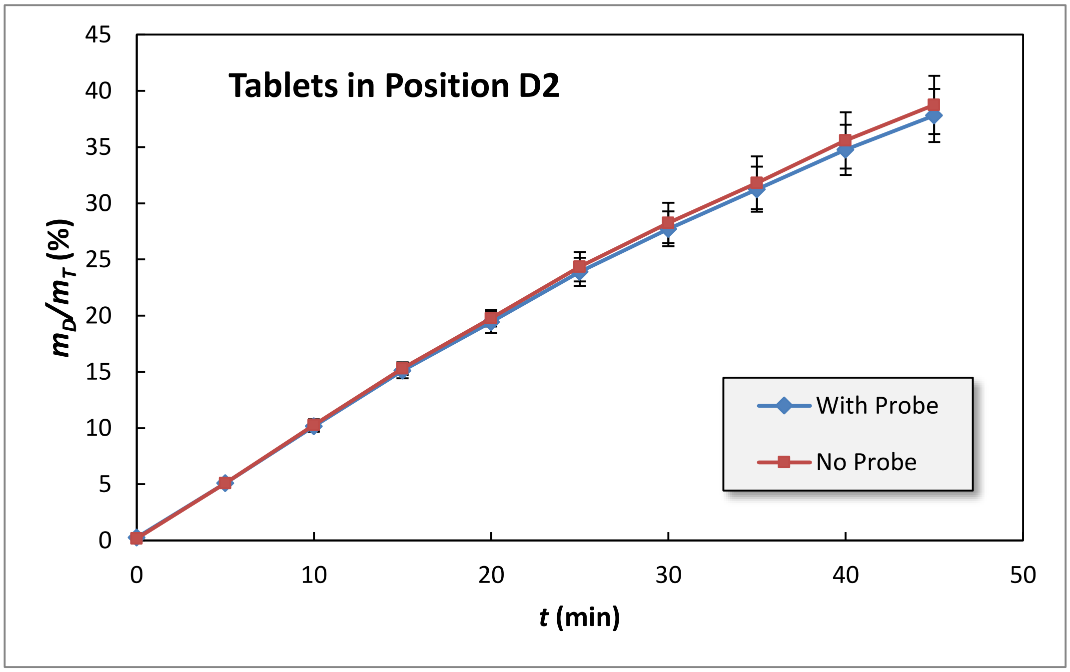

(B)

Figure 2.15 Dissolution profiles for experiments in the presence and absence of the fiber optic probe with: (A) Tablets in Position C2; and (B) Tablets in Position D2.

A comparison of the results for tablets on 20 ° circle with those on the 10 ° off-center indicates that m_D/m_T curves for tablets on the outer circle were larger than those on the inner circle. Typically, the final m_D/m_T value was about 33-39% for these 20 °off-center tablets, while it was 27-33% for the 10 ° off-center tablets. However, such a comparison also shows some similarities. At Positions A1 and A2, i.e., at the same azimuthal (tangential) location on different circles, the rotating fluid downstream of the first vertical element of the probe produced higher differences between systems with and without the probe. This difference was still evident for tablets at other downstream locations on the inner circle but was not significant for tablets on the outer circle.

2.4.5 Discussion for Dissolution Results

By examining the totality of the results obtained in this work (Figures 2.11 to Figure 2.15), one can conclude that, in general, the presence of the fiber optic probe can potentially have an effect on the dissolution process. The experimental results presented here show that salicylic acid tablets in systems with a probe have dissolution profiles that are consistently higher than those obtained in standard systems without a probe, although for some tablets located on the outer 20^o circle (Positions B2, C2 and D2) the dissolution profiles with and without the probe were found to be almost identical. The magnitude of the dissolution enhancement effect generated by the probe depends on how the process is conducted and the exact location of the tablet during the dissolution process.

Irrespective of whether the probe was present or not, the dissolution profiles for tablets on the outer 20^o circle were found to be higher than those on the inner 10^o circle, which, in turn, were higher than those for tablets fixed at the central position. This observation is consistent with previous work by this group in which it was showed that the region just below the impeller is poorly mixed and that tablets located just outside this small region can experience a significantly higher flow and hence faster dissolution rates [6, 7, 33, 40]. However, the presence of the probe increased the dissolution rate appreciably and more significantly when the tablets were closer to the center of the vessel than when they were away from it. For example, tablets fixed at the center of the vessel exhibited a percent dissolution that was about 1-2% larger with the probe than without it. This increase is appreciable considering that the final percent dissolution of the tablets at 45 minutes was about 22-24%, and that it can be exclusively attributed to the presence of the probe. These differences in dissolution profiles could not be attributed to data scatter since the average standard deviation was relatively small, i.e., 0.93%and 1.29% with and without probe, respectively. This increase in dissolution was even more significant for tablets downstream of the probe on the 10^o circle. The percent dissolution for tablets in Position A1, i.e., closest to the probe, was about 3-4% larger with the probe than without. Similar but smaller increases were observed for tablets further downstream of the probe (Positions B1 and C1), although the probe effect was reduced for Position D1. On the 20^o circle, the probe effect could still be observed but was typically much smaller, except for Position A2, which was the closest to the probe.

The dissolution profiles for tablets dropped in the vessel, i.e., according to the USP-recommended method, were also affected by the presence of the probe. During these experiments, one could clearly observe that the tablets typically remained close to the central position, although they also moved periodically to the 10 ° off-center circle. This movement can be expected to result in higher dissolution profiles, which were in fact found here to be intermediate between those for the central position and those on the 10^{o} circle. The results in Figure 2.11 (A) show that dropped tablets typically produced an absolute increase in m_D/m_T caused by the presence of the probe of about 1%, which represents a measurable increase over the baseline without the probe.

For most of the cases examined here, and especially for those cases that were more sensitive to the presence of the probe and presented the largest differences between curves with and without the probe, the values of the P (t-test) were smaller than the 0.05 value selected here as the lowest value to identify statistically similarity (Table 2.1). This implies that in those systems the dissolution profiles with and without the probe were statistically different, i.e., that the results obtained in those paired experiments were unlikely to belong to the same underlying population. The P (t-test) does not require that the difference between the two population be necessarily large, but only that such difference be significant enough with respect to variations associated with the experimental error (and captured by the standard deviation) to manifest itself consistently. In some cases the magnitude of this difference was small (e.g., in many of positions on the 20^o circle), while in others the presence or absence of the probe caused relatively large differences between the dissolution curves (e.g., Positions A1 and A2).

In all cases, the values of the FDA-recommended similarity factor f_1 and difference factor f_2 were within the suggested FDA range, indicating that the effect introduced by inserting the probe, although statistically observable, was not significant enough to fail the dissolution test. However, for positions where the dissolution process was more significantly affected by the probe, such as Positions A1 and B1, higher f_1 and smaller f_2 values were obtained, which were appreciably closer to the acceptance limits (Table 2.1). This work indicates that there is an increased risk of possible enhanced dissolution profiles when fiber optic probes are used. Therefore, routine verification checks of dissolution results obtained with probes and through manual sampling should be performed.

It should be noted that the measureable impact on dissolution observed in this work was caused by an extremely small probe consisting of two vertical elements only 0.8 mm in diameter. The probe was inserted in the medium by only 43.60 mm, i.e., it was located in the upper portion of the solution, whereas the tablets were on the bottom of the vessel. This fact points to the extreme sensitivity of the USP Apparatus 2 to small geometric changes in the system. The reasons for these effects are likely to reside in the changes to the vessel hydrodynamics introduced by the probe. Two related phenomena may be at work here. Firstly, the vertical elements of the probe can act as small "baffles" in the rotating fluid, disrupting the smooth tangential flow generated by the impeller and producing an enhanced dissolution rate. This phenomenon is well known and amply described in the mixing literature [61, 62]. Secondly, the presence of a single probe only one side of the vessel introduces a small asymmetry in an otherwise symmetrical system. Previous studies have shown that USP Apparatus 2 is very sensitive to any deviation from symmetry [6, 7, 33, 40, 63]. The small asymmetry caused by the probe can result in a non-symmetrical flow, thus enhancing mixing effects. The combined effects of the baffling and asymmetry can generate a small but appreciable flow difference, especially in the region near the bottom of the vessel where the tablet resides, and where the flow has been shown to be particularly weak [6, 33] and easily affected by small geometric changes. Hence, higher dissolution rates can be expected when the probe is used, as shown here for most tablets positions. Recently, a modification of the existing Apparatus 2, called “OPI” for “Off-center Paddle Impeller,” has been proposed in which the impeller is placed off-center with respect to the vertical centerline in the vessel [42]. Previous dissolution tests conducted in this novel apparatus have resulted in dissolution profiles that are quite insensitive to small geometric changes, such as the tablet location. It is likely that the use of the OPI system could alleviate the sensitivity of the current Apparatus 2 to the presence of inserted probes.

2.5 Results of PIV Velocity Measurements and CFD Simulations

2.5.1 Velocity Distribution Profiles

Figure 2.16 presents the velocity contours from CFD simulation in the standard USP Apparatus 2 system and for all the other four cross sections in the testing system with the fiber optic probe. The predicted velocity profiles on a vertical cross section through the impeller shaft for different orientations of the impeller. Figure 2.17 shows the velocity vectors of PIV measurements and also CFD predicted velocity profiles in both of the two systems.

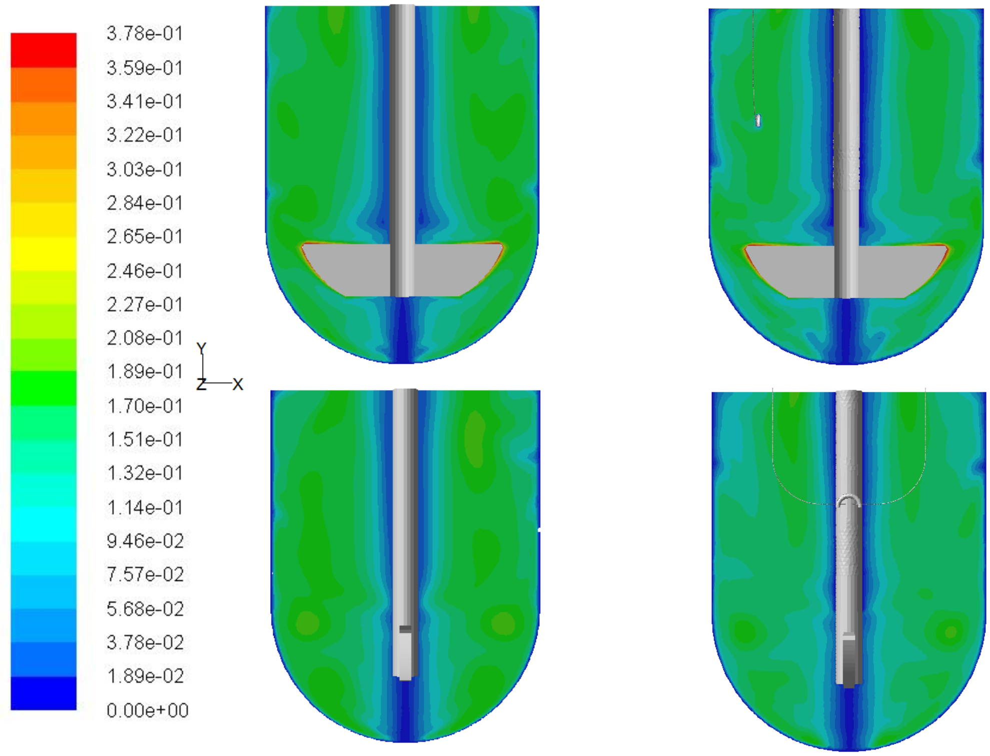

(A) **(B)**

Figure 2.16 CFD predictions of the velocity magnitude on a vertical cross section through the impeller shaft and for different impeller orientations (z-plane: plane of the impeller blades; x-plane: plane perpendicular to the impeller blades). Red color represents 3D velocity magnitudes equal to, or higher than $0.378 ms^{-1}$. (A) Standard system; (B) Test system with probe.

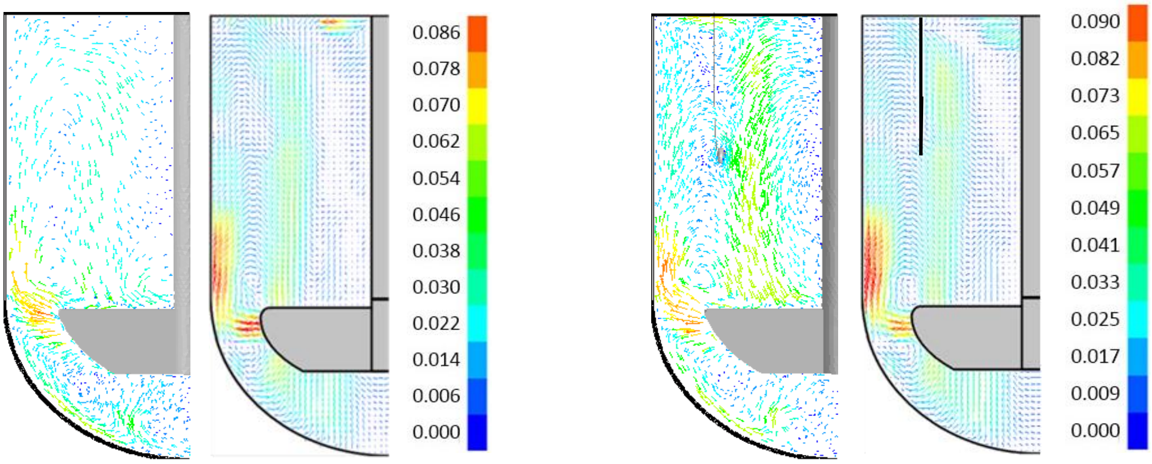

Standard System without Probe

Testing System with Probe-Section A

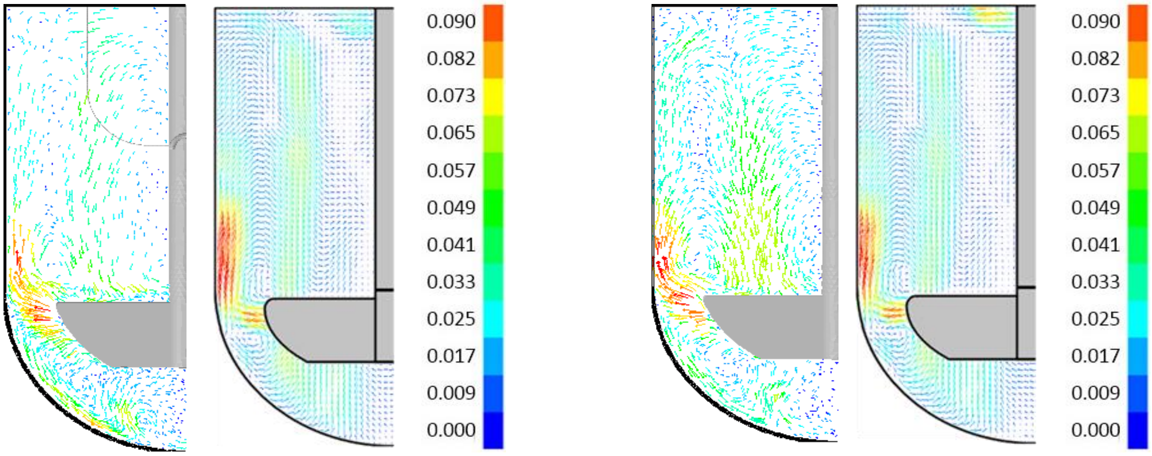

Testing System with Probe-Section B

Testing System with Probe-Section C

Figure 2.17 Velocity vectors from CFD simulation and PIV measurements in standard system and testing system of four different cross sections according to the probe position (continued).

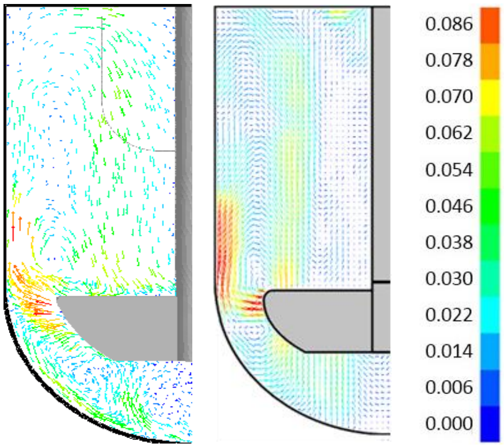

Testing System with Probe-Section D

Figure 2.17 (Continued) Velocity vectors from CFD simulation and PIV measurements in standard system and testing system of four different cross sections according to the probe position.

All of the velocity profiles in both systems show a similar flow pattern in the whole vessel. From the contour maps of CFD prediction in Figure 2.16, the general flow pattern and flow velocity magnitude was not significantly altered by the probe. Because of the impeller rotation, the fluid flow around the impeller had the highest velocity values, which were on the same order of magnitude of the impeller tip speed. The impeller-generated radial jet flow impacted the vessel wall, and formed strong upward and downward flows, producing the recirculation loops above and below the impeller. Above the impeller, the fluid pattern was dominated by an upper circulation loop associated with weak axial velocities that moved the fluid upward near the wall and then downward toward the impeller. Another even weaker vertical recirculation loop could be observed around the shaft. Below the impeller, the downward flows from the impeller-generated radial jet formed a recirculation loop. However, this loop did not fully penetrate the inner core zone just below the shaft, and the flow in this central inner core region was very weak and unstable.

The experiments also showed that the test system with the probe resulted in a slight difference in the velocity profiles. In Section A of test system, the fluid flowing from the impeller towards the vessel wall was slightly stronger than that in standard system or the other sections. This stronger flow produced higher velocity recirculation loops above and below impeller. Although the lower loop did not penetrate the inner core zone, the velocities near the vessel bottom, although still weak, were stronger that in the absence of the probe. For the other three sections, the velocities were also slightly different than those in the standard system. The loops velocities in Section B were a little higher than the other two sections. However, the enhancement in these three sections was smaller than that in Section A. The reasonable explanation is that the probe was suspended in the upper part of vessel in Section A, and the effect on the rotating fluid flow from the probe was obvious as the flow passed the probe, and the fluid flow moved to Section B, then Section C and finally Section D. The probe effect on the hydrodynamics decreased as the flow passed through these different sections, from A to D. The effect became weaker and weaker and in Section D no effect could be observed. This slight velocity difference in each section can result in the difference of tablet dissolution profiles, as shown in the previous section on tabled dissolution results.

For both of the two systems, the CFD velocity vectors in Figure 2.17 show the similar flow pattern with the experiment results. Since the CFD models for both systems have a large number of cells, the vector distribution is dense and the differences of each velocity profile cannot be clearly observed. However, the general flow pattern and velocity distribution can be obtained, and they are generally in agreement with the PIV results. Moreover, the velocity at each node in the CFD model were plotted, from which the difference of velocity profile could be found to better compare the velocity obtained from PIV experiment with the CFD results.

2.5.2 Velocity Comparison of CFD and PIV results

The axial and radial velocities on each horizontal iso-surface obtained from PIV experiments and with CFD simulations were plotted for both standard and test systems as shown in Figure 2.18 and Figure 2.19. The measurements for the standard system were repeated for six times, and the standard deviation was small (< 1%), which indicated the experiment was reducible and reliable. For each section, the experiments were repeated three times and plotted with the standard deviation. The velocities on each of the four sections for the probe system case were plotted and compared with the standard system. For each case, the PIV measurement results were compared with CFD simulations. The velocity changes resulting from the probe could be found out by comparing velocity profiles between these two systems. In Figure 2.18 and 2.19, the ordinates represent the normalized non-dimensional fluid velocity (scaled by using the impeller tip speed, V_{tip}) and the abscissas represent the normalized radial position (scaled using the vessel radius, R_0).

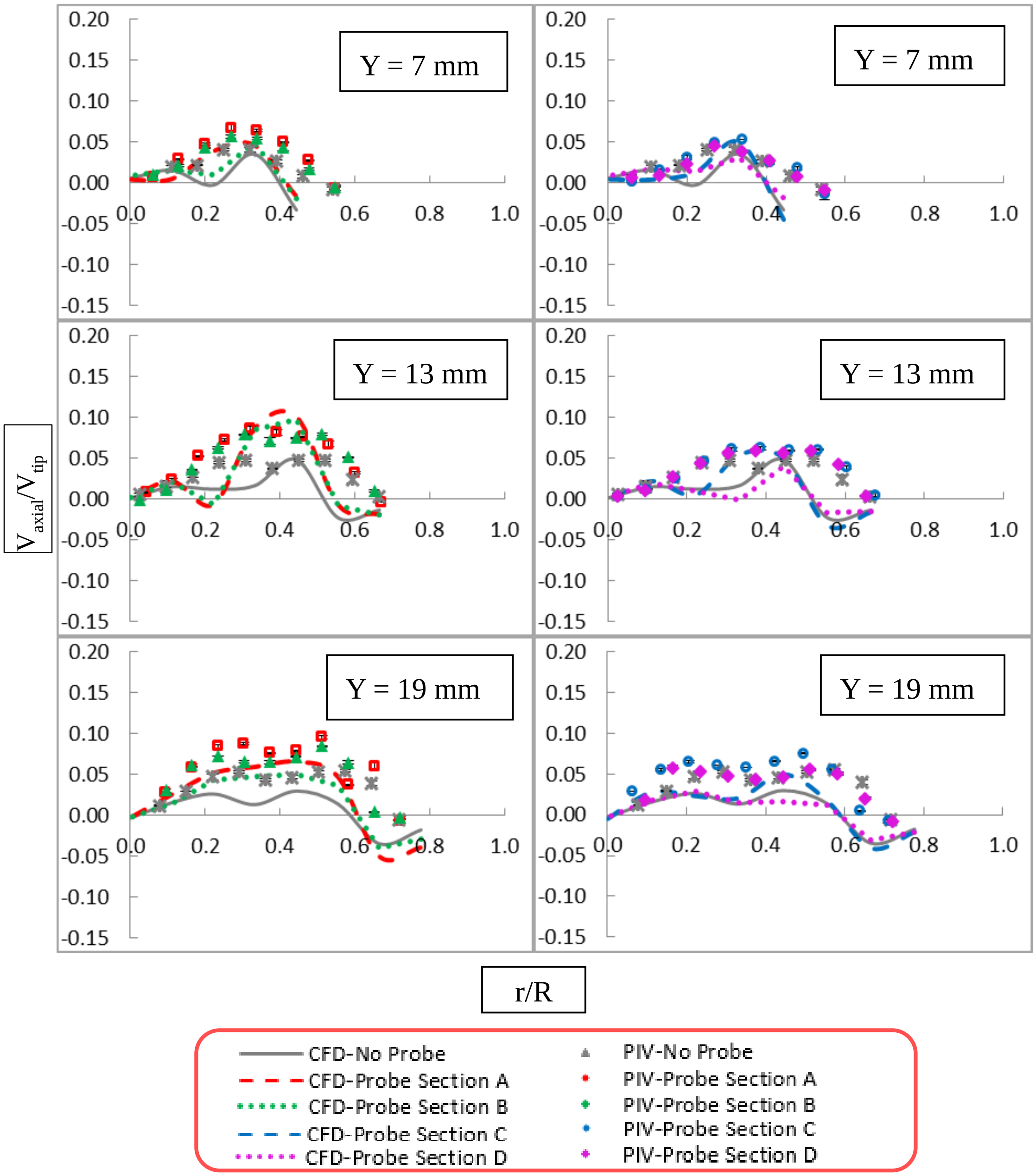

Figure 2.18 Scaled axial velocity comparison between experimental PIV velocity data and CFD predictions on iso-surfaces in both standard system and testing system of four cross sections (continued).

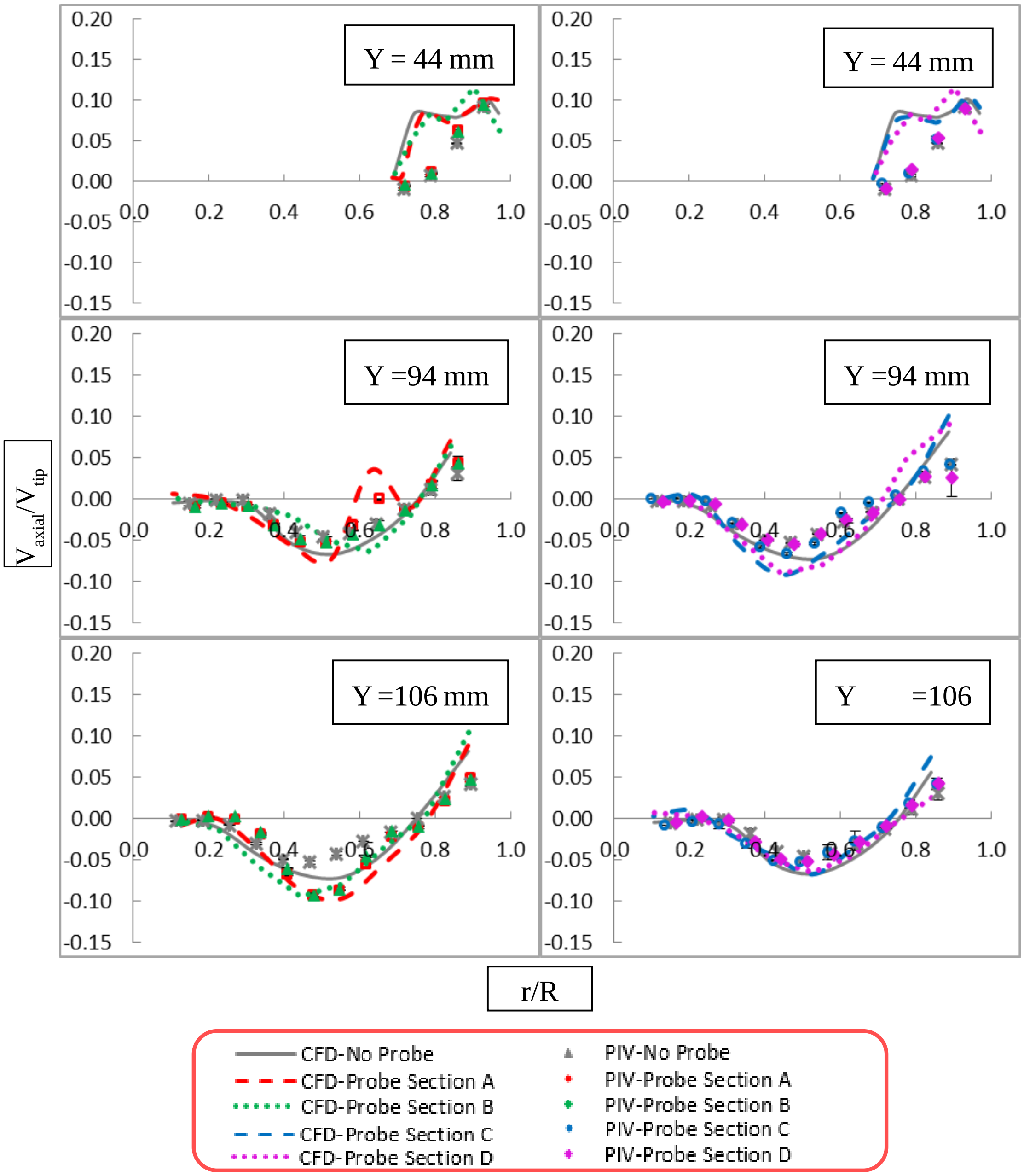

Figure 2.18 (Continued) Scaled axial velocity comparison between experimental PIV velocity data and CFD predictions on iso-surfaces in both standard system and testing system of four cross sections.

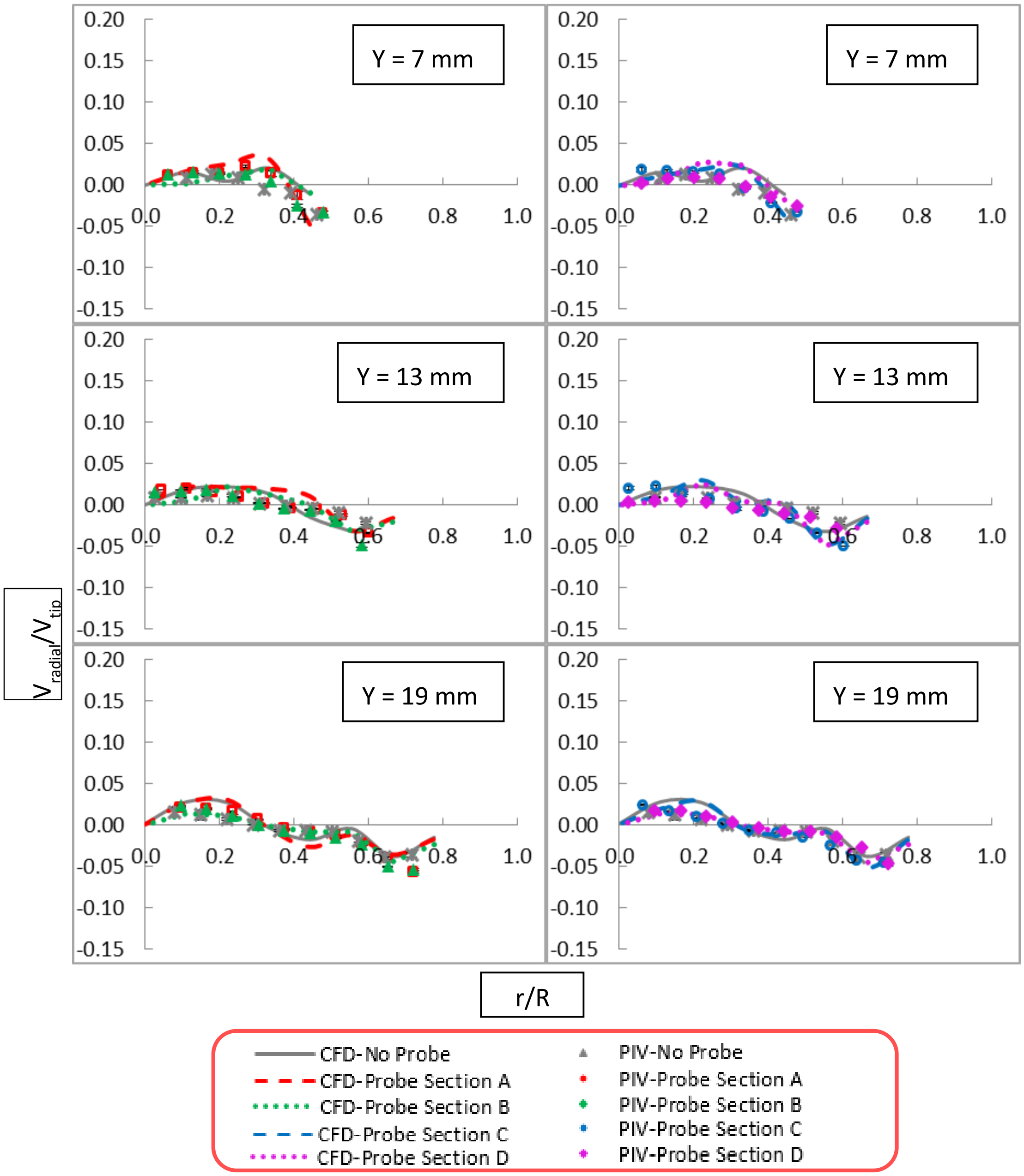

Figure 2.19 Scaled radial velocity comparison between experimental PIV velocity data and CFD predictions on iso-surfaces in both standard system and testing system of four cross sections (continued).

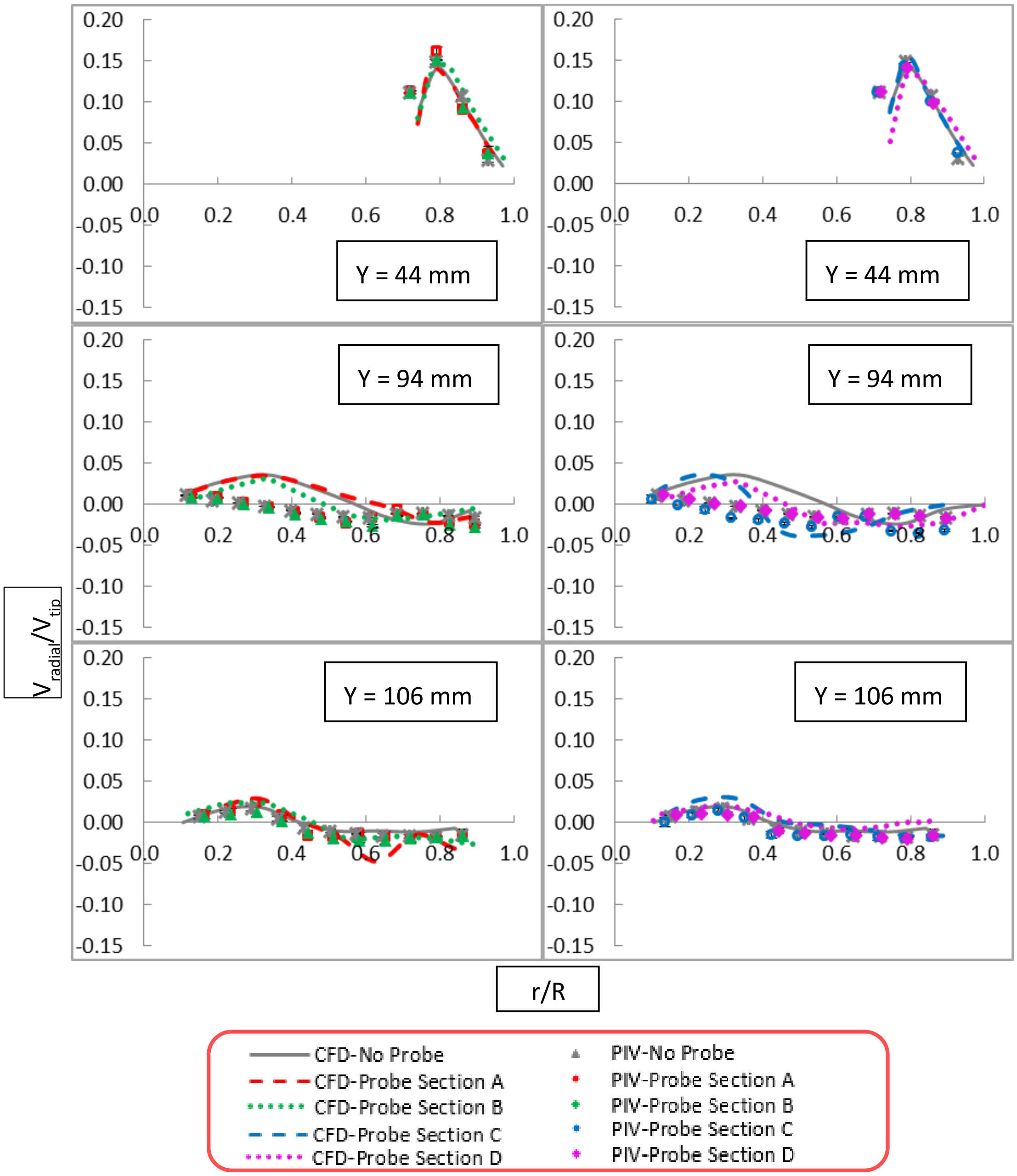

Figure 2.19 (Continued)Scaled radial velocity comparison between experimental PIV velocity data and CFD predictions on iso-surfaces in both standard system and testing system of four cross sections.

Velocity Profiles Below the Impeller. On the iso-surface Y = 19 mm, the CFD-predicted axial velocities were slightly higher than the PIV measurements for both of the standard and testing system. Most of the axial velocities were positive and the trends of the axial velocity were similar for the simulation and the experiment results. Both the simulations and the experiment results showed that the axial velocities were higher in the test system than in the standard system on all four sections. Moreover, the axial velocity differences on Section A were the highest in both of the simulations and the PIV measurement, but they became increasingly smaller when the position turned from A to D. As for the radial velocities on all four sections, the CFD and PIV results of are very close to each other, and the difference between two systems is small.

Similar trends can be observed for the axial and radial velocity on both iso-surfaces Y = 13 mm and Y= 7mm. In the region $0.2<r/R_0<0.4$, the CFD axial and radial velocities were higher than the PIV results. The axial and radial velocity differences between the test system and the standard system are obvious, and they are much higher in Sections A and B. In summary, for the three iso-surfaces in the core region under impeller, both the CFD and the PIV results show that the axial and radial velocities in the test system deviate from those in the standard system, and especially so for Section A and B. This indicates that the probe does result in differences in the fluid flow below the impeller that result in higher velocities in the region where the tablet is typically located during a dissolution test.

Velocity Profiles in the Impeller Region and above the Impeller. In these regions, the velocity profiles were obtained for three iso-surfaces, i.e., Y = 44 mm (top edge of the impeller), Y = 94 mm and Y = 106 mm. In Figure 2.18, the axial velocities on iso-surface Y = 44 mm of CFD simulation are positive, indicating an upward flow. In this region, the velocity was close between different cross sections, because their agitation speed was the same which was 100rpm, so their velocity around the impeller were very close to each other.

The PIV data shows that on the iso-surfaces at Y = 94 mm and Y = 106 mm, the axial velocities for the system with the probe are negative (downward flow) and increase from near zero at the impeller shaft position to peak value at similar radial positions ($0.5<r/R_0<0.6$). In the region of $0.8<r/R_0<0.9$, the axial velocity becomes positive indicating an upward flow. It should be remarked that the results for Section A on iso-surface Y = 94mm (position of probe bottom) are different when $0.5<r/R_0<0.6$. Here the velocities decrease more rapidly than in other experiment result and approach zero because the probe gives a resistance for the downward flow through it. The CFD simulations have similar result in general, but the decreasing of velocity of section A on iso-surface Y = 94 mm is more significant than that of the PIV results. For the region $0.4<r/R_0<1$ on iso-surface Y = 106 mm, the CFD prediction has a higher upward flow velocity than PIV results.

In Figure 2.19, the radial velocities for the region above the impeller are shown. On all of these three iso-surfaces, the PIV and CFD results are very close to zero for $0.1<r/R_0<0.9$, indicating that the flowing is weaker than in other regions. This region is above the impeller region and it far away from the tablet position. Therefore, it has less relation with the tablet dissolution process. However, it still shows that the radial velocity is a little bigger in section A and B on iso-surfaces Y = 94 mm in the region $0.1<r/R_0<0.4$ and $0.7<r/R_0<0.8$. Results for Section A from both the PIV and CFD at Y = 94 mm are slightly different from the other sections. The velocity decreases and then sharply increases in the region $0.6<r/R_0<0.7$, indicating that the probe produces a resistance in the radial direction towards it.

2.5.3 Discussion

The velocity distributions of both the standard dissolution system (apparatus 2) and the testing system are presented to show the general flow map and the hydrodynamics difference between the two systems, with comparison of CFD prediction and PIV measurement. Since the PIV data is extracted from 2D velocity measurement, only the axial and radial velocity on each cross plane were obtained and compared with CFD results. The 2-dimension velocity vectors from the PIV measurement are in general similar to the CFD-predicted velocities, although for some parts of regions they show slightly difference. Since the hydrodynamics in Apparatus 2 is highly non-homogenous especially below the impeller, a small difference of the impeller position may result in big change in the flow pattern (Bai and Armenante, 2007b). Therefore, any small difference in impeller position between the CFD and PIV may cause some difference of the flow pattern in the zone below the impeller. However, by comparing the radial velocity, axial velocity and velocity vectors, the CFD method can be seen to generally well predict the PIV-measured overall flow field and hydrodynamics effect of probe in the dissolution testing system.

The flow inside the standard Apparatus 2 is very complex, as shown in this study and in previous work in this group. Therefore, the optic probe inserting on one side of the apparatus can make it more complex and even asymmetric. In this study, the probe effect on the hydrodynamics flow can be clearly observed through the information in the CFD-generated Figures 2.18 and 2.19 (axial and radial velocity comparison), combined with the vectors display in Figures 2.16 and 2.17.

As shown in Figures 2.18 and 2.19, on each iso-surface, the general profiles for the axial and radial velocities are similar for all cross sections in both systems. However, the value of the axial and radial velocities on Section A is obviously influenced by the presence of the probe. This is less for Section B, Section C and Section D. This trend is confirmed from the PIV data and CFD curves shown in Figures 2.18 and 2.19, indicating that inserting probe has indeed influence on the flow pattern, although the general flow pattern did not change significantly. The probe has a bigger effect on Section A and Section B, which is shown also in the CFD data analysis.

Since the tablet is located in the inner core region below the impeller, it is hard to say that the flow is more disturbed in the area below the impeller while the probe is placed in the section above the impeller. However, the CFD and PIV results show some effects.

The first is that the axial and radial velocities below the impeller are larger in the testing system than in the standard vessel. In Figures 2.14-2.16, on the iso-surface Y = 7 mm, Y = 13 mm, and Y = 19 mm, it is obviously that the axial velocities for the standard system are lower than those in all of the sections in the testing systems. Especially in Sections A and B, the velocities are appreciably higher than that in standard system. The radial velocity on iso-surface Y = 19 mm is very close in both of the systems and close to zero. On the other two iso-surfaces Y = 7 mm and Y = 13 mm, the radial velocities are larger in the testing system than in the standard system. The slight increase of velocity in the testing system can result in a more intensive flow in the core region below the impeller, and can increase the tablet mass transfer rate. Although on the iso-surface Y = 19 mm the velocities are very close of the two systems, the velocities on the iso-surfaces at Y = 7 mm and Y = 13 mm, which are near the bottom of the vessel, show appreciable variations. Such velocity changes in the two systems can affect and increase the tablet dissolution effect.

Further evidence of the hydrodynamics effect can be observed from the velocity magnitude map in Figures 2.16 and 2.17 by PIV measurement and CFD predictions. In the testing system, the perturbation in the flow can be caused by the probe which is positioned in the region above the impeller. Therefore, it can be confirmed that the probe did generate a "baffle effect" altering the flow. Moreover, the perturbation generated by the probe above the impeller can reach the region below the impeller. Although the perturbation may become progressively weaker down along the recirculation flow, its effect could still be noticed. This effect is more obviously in Section A and Section B where the flow in the region below the impeller has increased turbulence and intensive than that of standard system.

2.6 Conclusion

The effect of an arch-shaped fiber optic probe on dissolution was experimentally studied in a USP Dissolution Testing Apparatus 2 using non-disintegrating salicylic acid calibrator tablets that were either dropped in the vessel according to the USP procedure or fixed in place at nine different positions on the vessel bottom. In most cases, the presence of the probe resulted in statistically significant increases in the dissolution curves with respect to the curves obtained without the probe, as assessed using a paired t-test approach.

In general, tablets at, or close to, the center of the vessel were more significantly affected by the presence of the probe, and so were tablets located immediately downstream of the probe. The magnitude of the absolute increase in the dissolution profiles for the most sensitive tablet positions was usually between 2% and 4%. With such differences, the value of the FDA-recommended difference/similarity parameters f_1 and f_2 were always within their acceptance limits, although in some cases just barely for f_1.

CFD simulations and PIV measurements were also conducted for Dissolution Testing Apparatuses 2 both in the presence (testing system) and in the absence (standard system) of the fiber optic probe. The testing system was studied at four cross sections

(Section A, B, C, and D).

Substantial agreement was found between the PIV data and the CFD predictions. The velocities in the upper region of the vessel where the probe is located were clearly affected by the presence of the probe. More importantly, some velocity components near the vessel bottom where the tablet is usually located, were found to be appreciably affected by the presence of the probe. Specifically, both the CFD simulation results and PIV data show that the axial velocities near the bottom are larger in the probe system than in the standard system. In addition, in the region just under the probe, the differences in axial velocities between the two systems are the largest in both of the simulations and PIV measurement, but they become progressively smaller at locations further away from the probe.

The results of this work indicate that the arch shaped fiber optic probe introduces as small but measurable baffling effect in the hydrodynamics in the dissolution vessel. This effect results in changes in the flow velocities which parallel the results of dissolution tests, where the dissolution profiles were typically found to be higher in the presence of the probe, but not sufficiently high to fail the tests, according to the FDA criteria (f_1 and f_2 values).

In summary, the hydrodynamic effects generated by the arch-shaped fiber optic probe are small but clearly measurable. The changes in velocity profiles in the dissolution vessel result in detectable differences in the dissolution profiles, although not high enough to cause test failures. However, these differences could contribute to amplify the difference in dissolution profiles in those cases in which tablet has an intrinsically higher release rate.

CHAPTER 3

EXPERIMENTAL DETERMINATION OF MINIMUM AGITATION SPEED OF SOLID SUSPENSION, N_{JS}, IN USP APPARATUS 2 SYSTEM

3.1 Background and Objective

In dissolution systems, it is often desired to eliminate “coning” effects, i.e., the formation of a pile of unsuspended particles resulting from the disintegration of a tablet during the initial stages of the dissolution process. This is typically achieved by increasing the impeller speed. In studies on the suspension of finely divided solid particles in mixing vessels, the most critical agitation speed that needs to be determined is the minimum agitation speed required to “just suspend” all the particles, N_{js}.

The objective of this portion of the work was to determine the minimum agitation speed, N_{js} of finely divided solid particles for different conditions in the USP 2 system. Accordingly, N_{js} was measured in a USP 2 system with a novel technique developed through previous work in our laboratory [64]. This approach consisted of experimentally measuring the size of the circular region of the vessel bottom covered by the solids at increasing values of the agitation speed, N, plotting N vs. the size of this region (expressed as either the region’s diameter D_S or its area A_S), and linearly regressing the data to obtain N_{js} as the limit of the N value for D_S or A_S going to zero. An example of this method is presented in Figure 3.1.

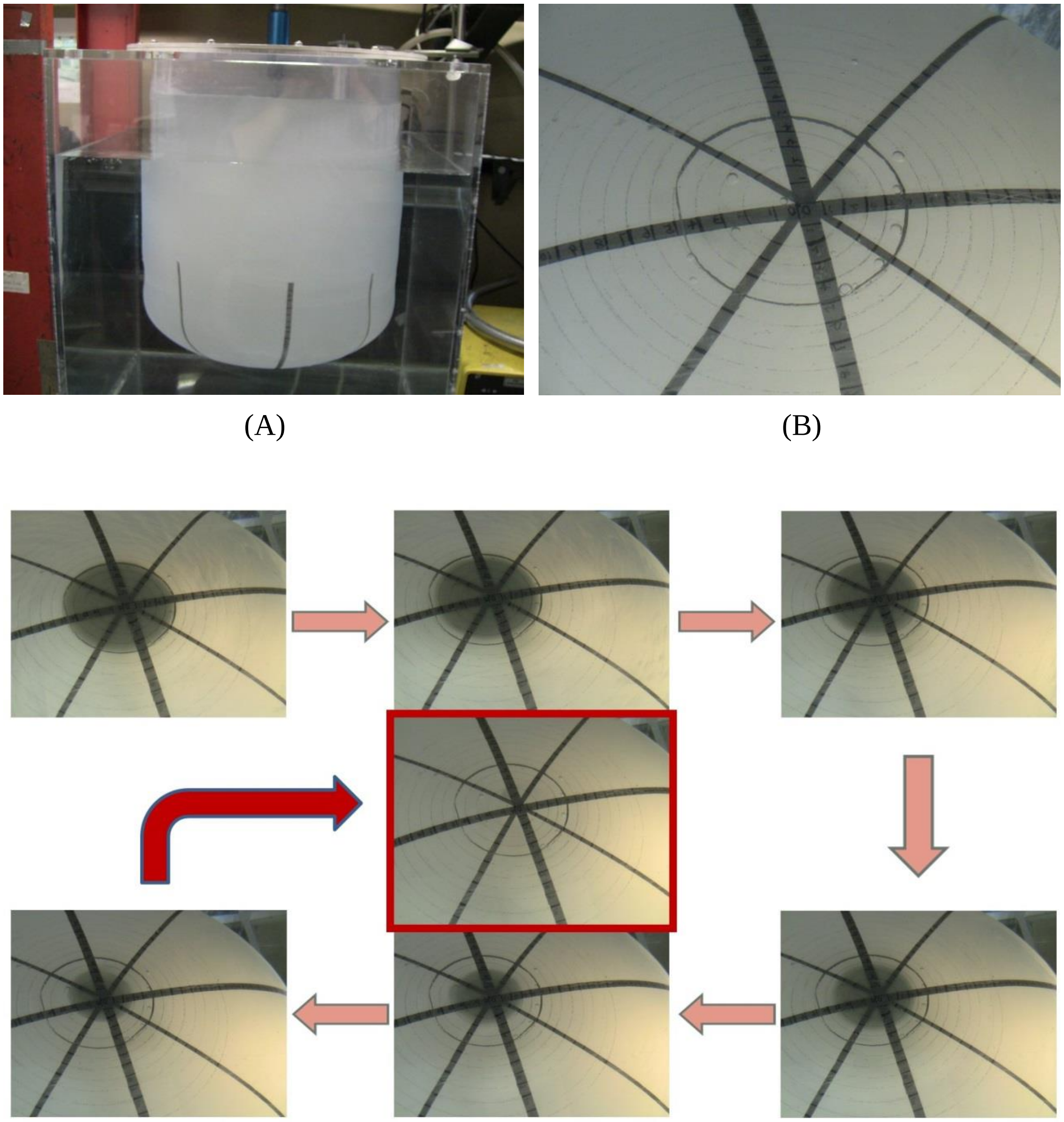

(A) (B)

(C)

Figure 3.1 (A) Torispherical-bottomed glass-lined tank system. (B) Bottom view of the tank with equally spaced circles drawn on its bottom. (C) New approach to N_{js} by Zhou and Armenante [64].

The N_{js} results obtained with the new approach were compared with those obtained using the traditional Zwietering's approach, visually requiring that the solids do not rest on the vessel bottom for more than 1-2 seconds. The visual observation method was also used to experimentally find out the N_{js} for complete solid suspension under different operating conditions. Excellent agreement was found between the results obtained using one of the novel approaches used here (i.e., that based on Ds) and those obtained using Zwietering's method. The novel method proposed here completely eliminates the observer's bias from the experimental determination of N_{js}.

The experimental system here is the USP Dissolution Apparatus 2, with a standard 1-L vessel filled with either 900mL or 500mL of dissolution medium. In the experiments, the relationship between N_{js} with the experiment parameters, such as particle density and particle size was obtained.

3.2 Experimental System, Materials, and Method

The solid suspension experimental system was the USP Apparatus 2 system, as mentioned in Chapter 2, including the USP Apparatus 2 device and the 1-L vessel. Before the experiment, equally spaced circles were drawn on the bottom of the vessel, similarly to the method developed by Anqi Zhou [64]. In an improved design, circular lines spaced 5 mm apart from each other (as measured on the hemispherical bottom) were etched on the outside of a typical USP Apparatus 2 vessel in Figure 3.2.

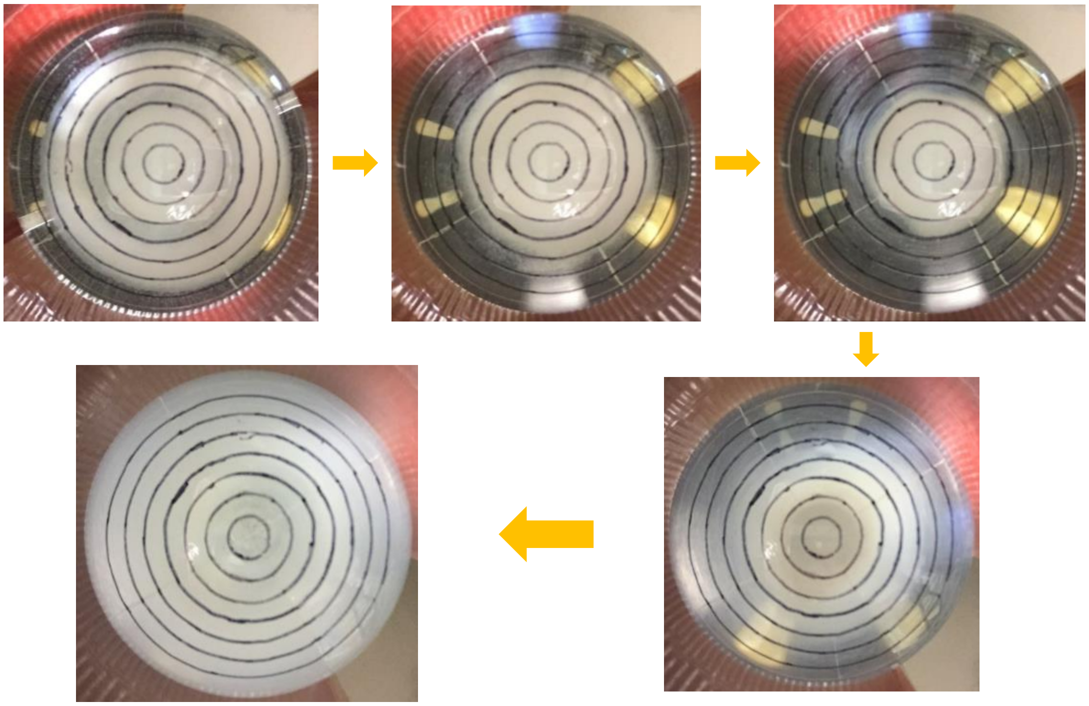

Figure 3.2 Bottom view of the USP 2 vessel with equally spaced circles.

These circles allowed for an easy determination of the area of the vessel bottom covered by solids in an experiment. The vessel was filled with either 900 mL or 500 mL of water. The particle density was determined by a pycnometer which could give actual density measurements for the particles. Uniform solids particles with different sizes and densities in different experiments were added to the liquid. The solids faction was always equal to 0.5% of the liquid volume. In many experiments the solid particles were silica particles (Evonik Corporation, Piscataway, NJ) with different sizes. These particles were spherical and with a uniform size from 10 μm to 100 μm. Other kinds of particles were also used to find out the relationship of N_{js} vs. particle density, such as glass beads, silver-coated hollow borosilicate glass spheres (Dantec Measurement Technology USA, Mahwah, NJ, USA), specifically hydrophilic fumed silica particles (Aeroperl 300/30, Evonik Corporation, Piscataway, NJ), and titanium dioxide particles (Aeroperl P25/20, Evonik Corporation, Piscataway, NJ). The particle sizes and densities are shown in Table 3.1.

Table 3.1 Sizes and Densities of the Solid Spherical Particles Used in This Work

Particle Type	Particle Size (μm)	Particle Density (g/cm^3)
Aeroperl 300/30	30	2.072
Aeroperl P25/20	20	3.197
Silver-Coated Hollow Glass Spheres	12	2.600
Silica Particle	11.3	1.830
	40.3	1.830
	112.5	1.830
	250.2	1.830
Glass Beads	40	2.332
	60	2.332
	75	2.332
	200	2.332

A typical experiment consisted of assembling the system, filling the vessel with the desired volume of liquid and adding the solid particles. The solids were initially at rest on the vessel bottom. Agitation was started at a low speed that did not allow the solids to become fully suspended. The system was allowed to reach steady state and the vessel bottom was observed with a help of a mirror to determine the bottom region covered with unsuspended solids once a dynamic equilibrium has been reached. A photograph was taken to record the measurement. The solids typically covered a circular region of the vessel bottom, often a nearly perfect circle, whose diameter and area could be easily measured with the help of the circles drawn or etched on the vessel bottom. This procedure was repeated at increasing values of the impeller agitation speed. As the agitation speed increased the solids began to be suspended.

Since the vessel bottom had been marked with circles and radii emanating from the vessel bottom center, both the diameter D_S of the area covered by solids at a given agitation speed N and the corresponding area A_S could be recorded and measured. In a typical experimental run, the solids covered on a circular area, N values were typically recorded at D_S values in the range 10 mm-60 mm. As the agitation increased more solids became suspended and eventually all solids were suspended. The values of N at which the particles were all suspended was visually detected and recorded. In addition, plots of N vs. D_S and N vs. A_S were obtained, and linear regression lines were used to find the predicted extrapolated values of N by these two methods when $D_S \rightarrow 0$ as well as when $A_S \rightarrow 0$. For each experimental configuration at least five measurements of N vs. D_S and N vs. A_S were taken. All experiments were conducted in triplicate.

3.3 Results

For each type of particles, experiments were conducted triplicate and the standard deviation was calculated for each point. The typical standard deviation was too small (<1%) to be plotted, indicating that the results were highly reproducible. An example of these results is shown in Figure 3.3.

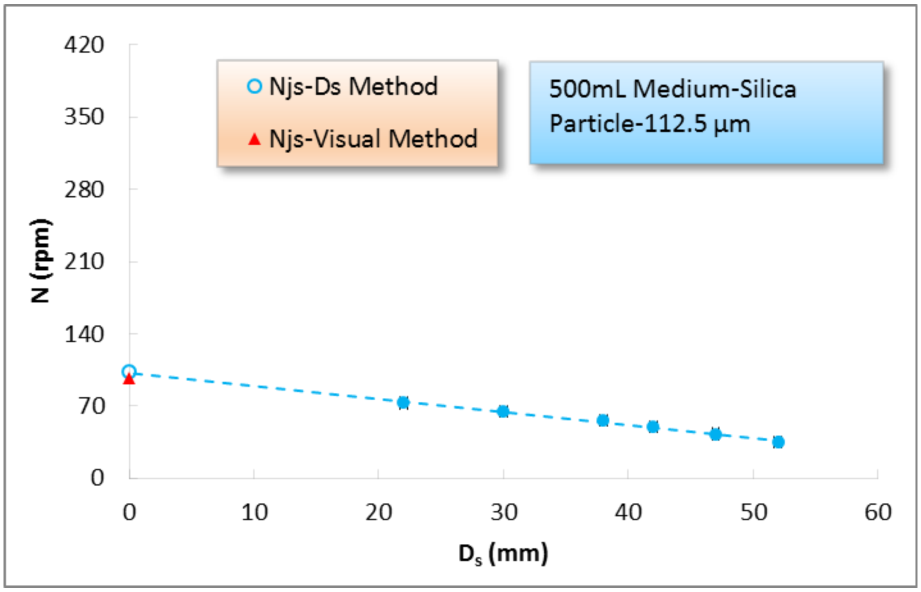

Figure 3.3 Standard deviation for 112.5μm silica particles with Njs-Ds-Method.

Plots of the N vs. D_S and N vs. A_S are shown respectively in Figure 3.4 and Figure 3.5. When N was plotted as a function of D_S the experimental points in the figures aligned themselves on straight lines. The data were linearly regressed and the extrapolated value of N for $D_S \rightarrow 0$ was taken to be the experimental value of Njs based on this method (Njs-Ds). This value was compared with the value of Njs obtained visually (Njs-visual). A similar approach was used to determine Njs-As, the experimental value of Njs based on a regression of N vs. As. The values of N_{js} so obtained are summarized in Table 3.2 for different experiment conditions.

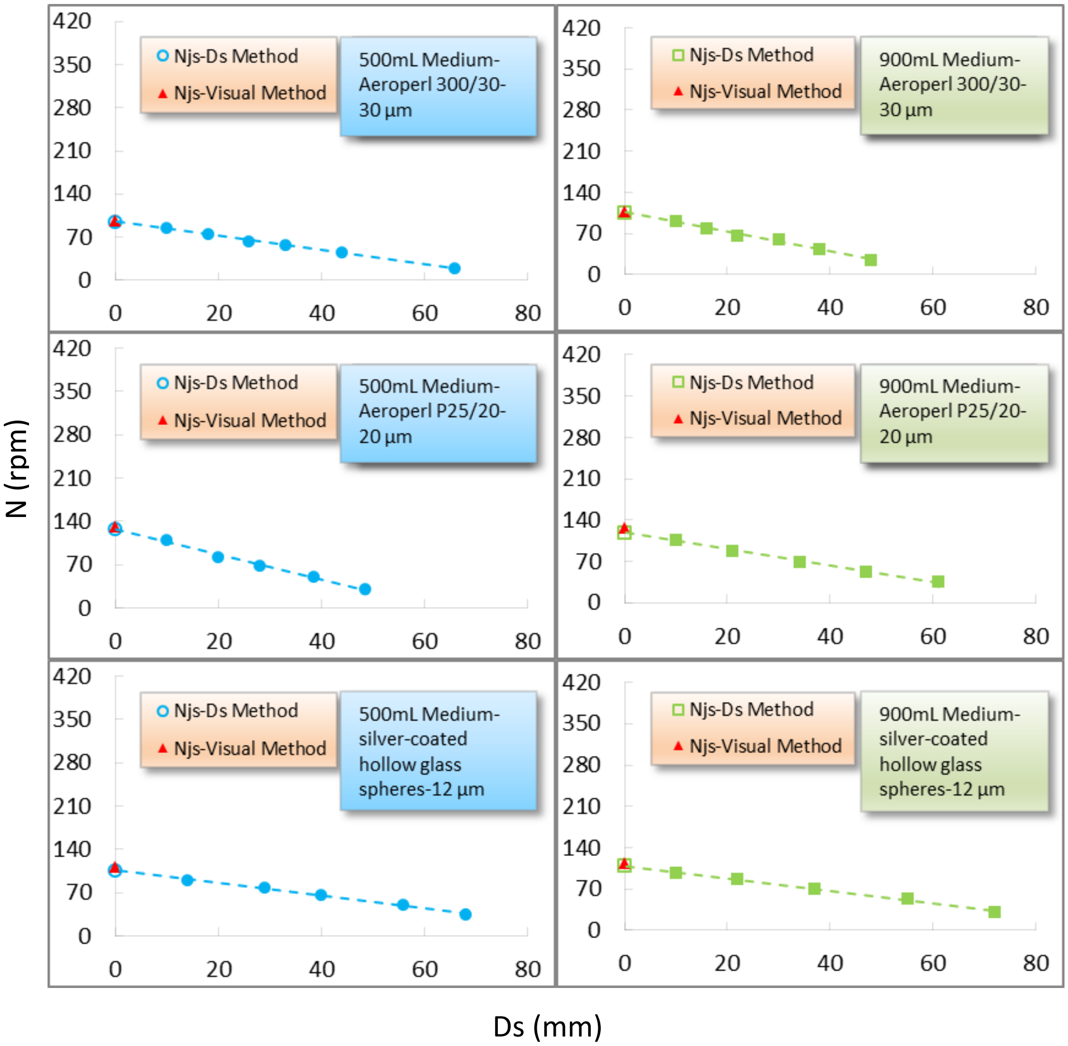

Figure 3.4 N_{js} obtained by D_S method in USP 2 system of 500mL and 900mL medium volume with different particle size and particle density (Continued).

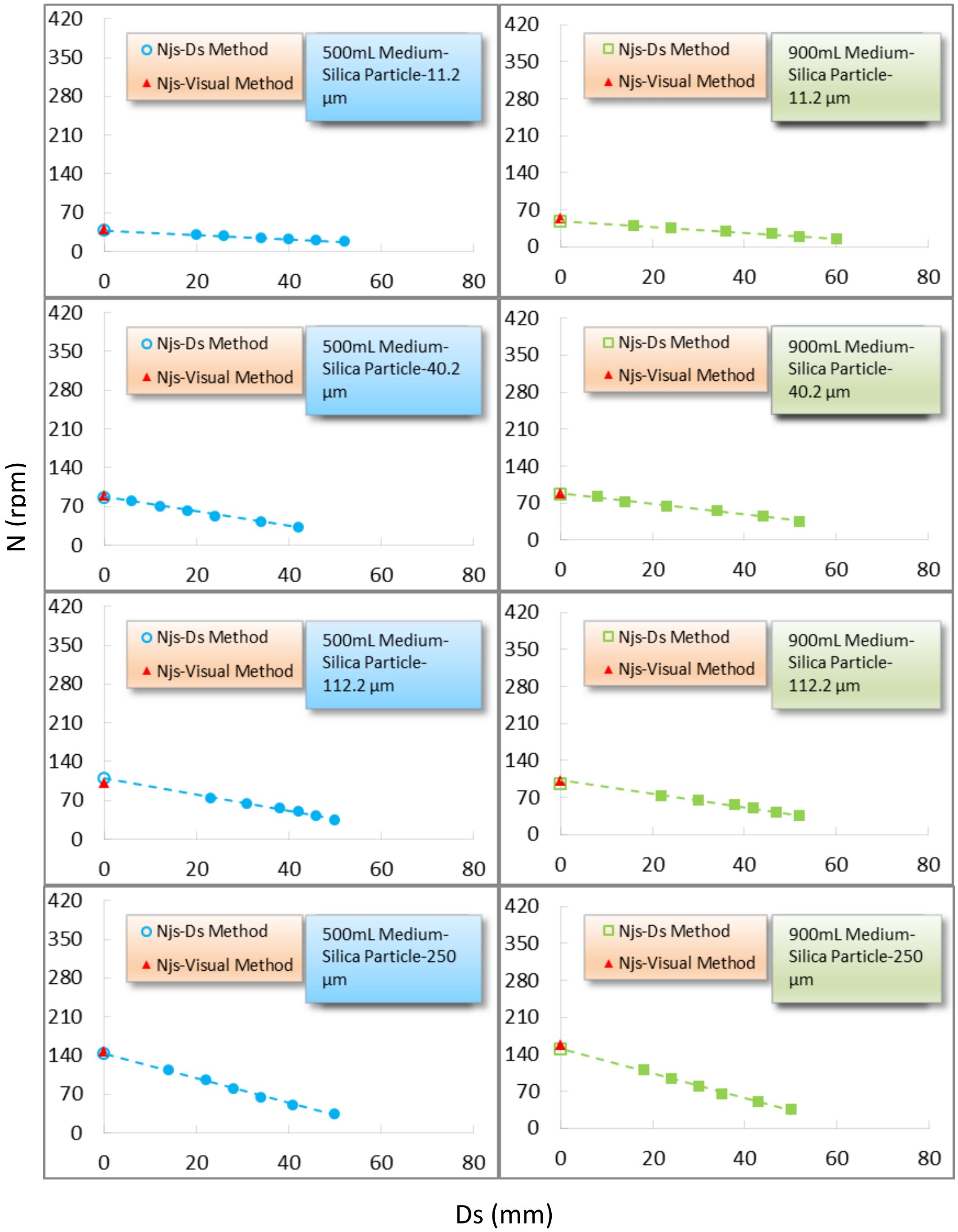

Figure 3.4 (Continued) N_{js} obtained by D_S method in USP 2 system of 500mL and 900mL medium volume with different particle size and particle density.

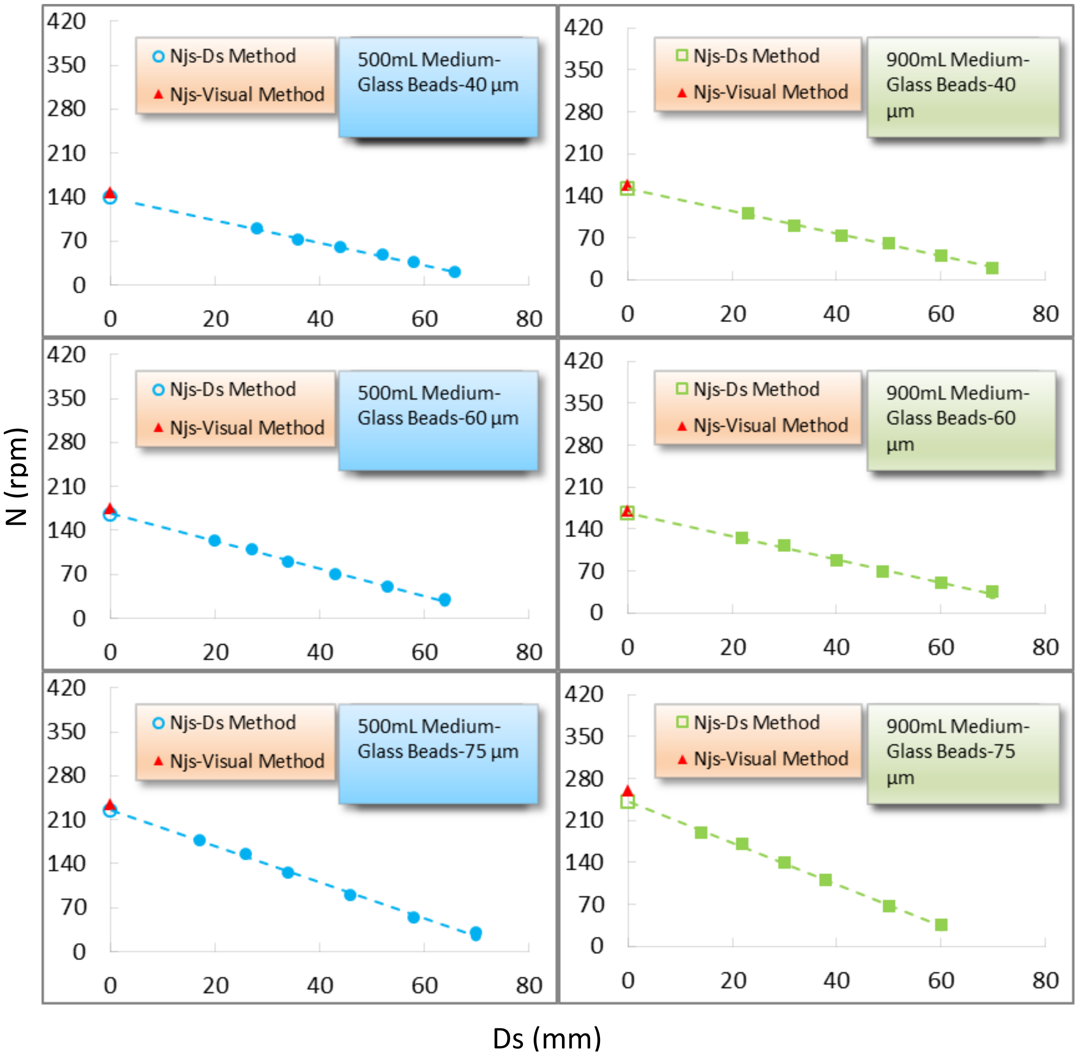

Figure 3.4 (Continued) N_{js} obtained by D_S method in USP 2 system of 500mL and 900mL medium volume with different particle size and particle density.

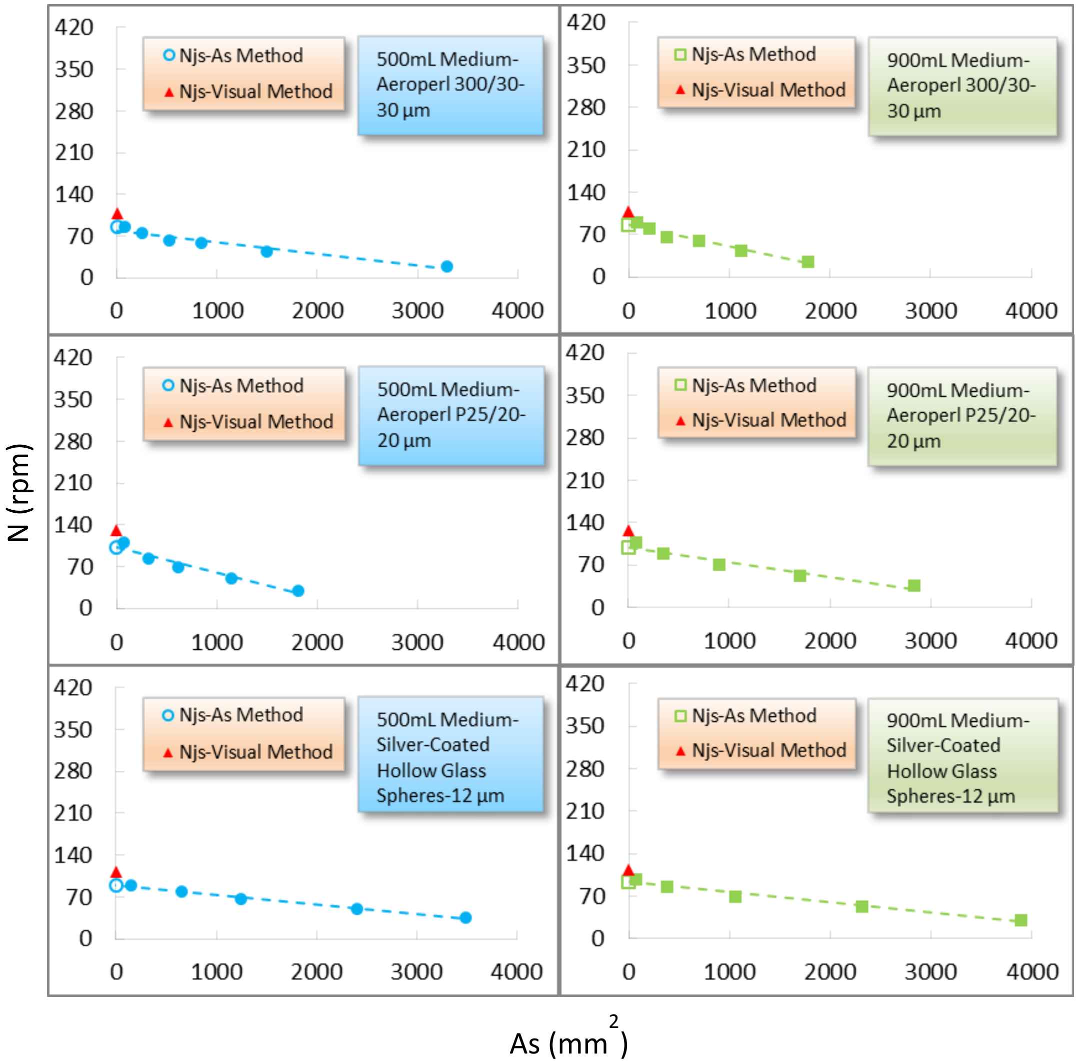

Figure 3.5 N_{js} obtained by A_S method in USP 2 system of 500mL and 900mL medium volume with different particle size and particle density (Continued).

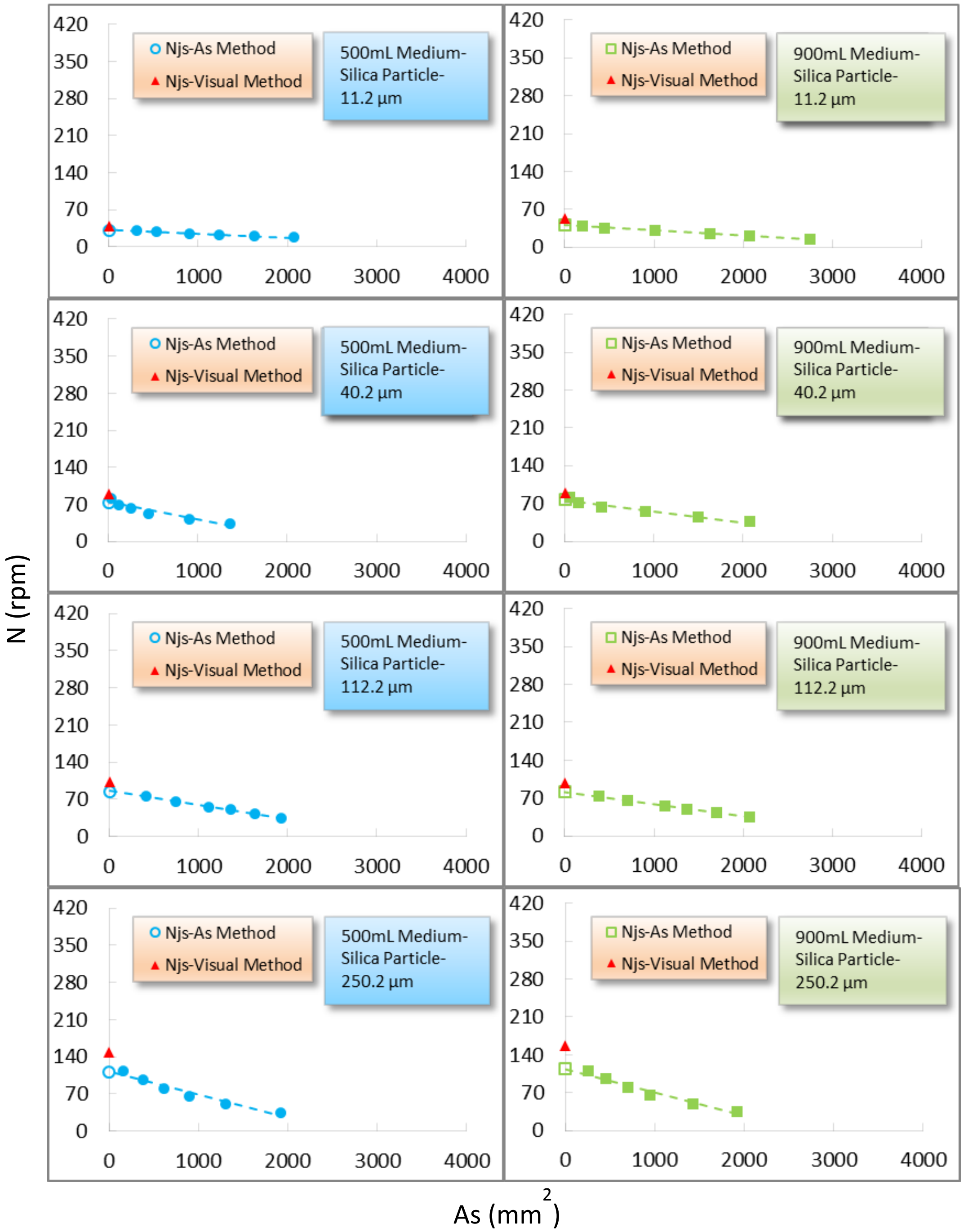

Figure 3.5 (Continued) N_{js} obtained by A_S method in USP 2 system of 500mL and 900mL medium volume with different particle size and particle density.

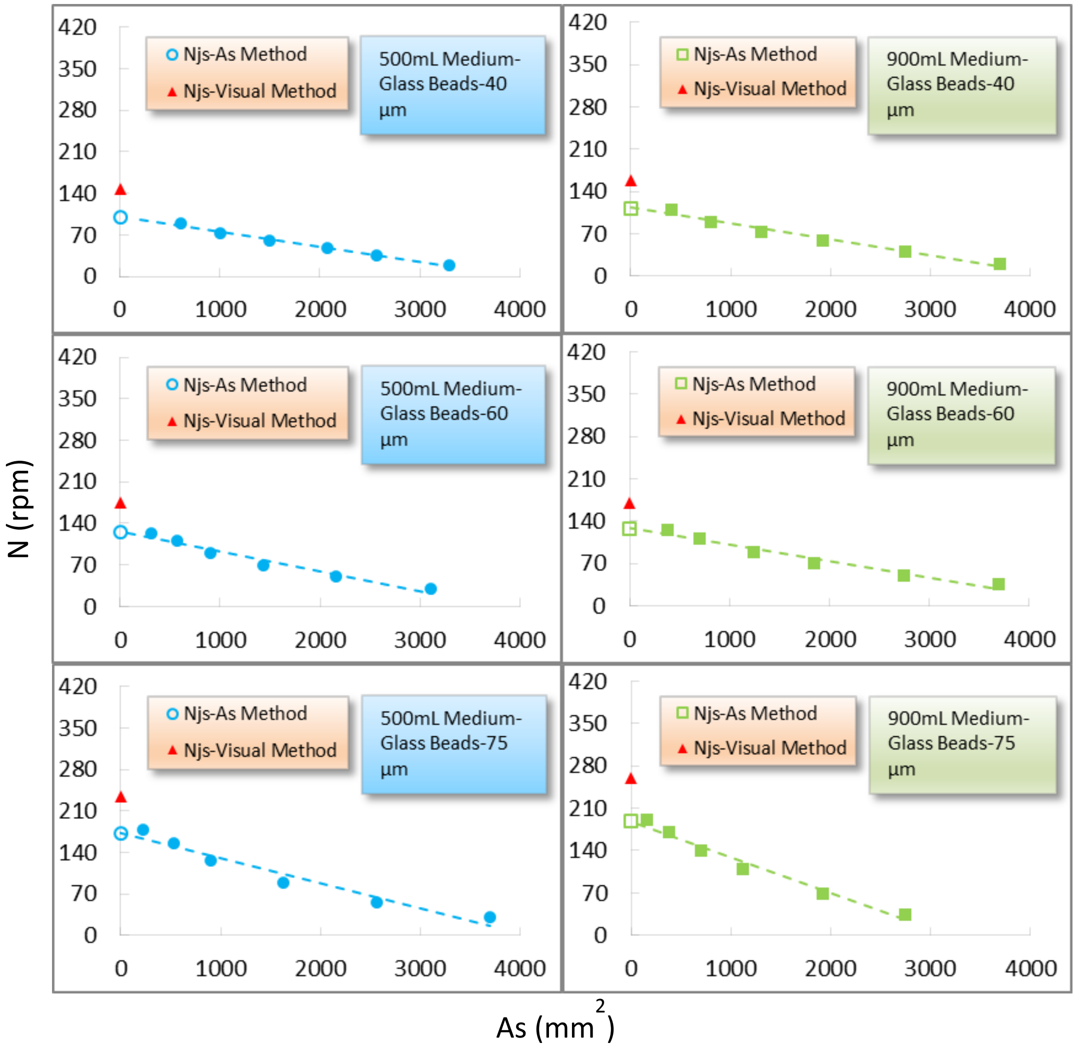

Figure 3.5 (Continued) N_{js} obtained by A_S method in USP 2 system of 500mL and 900mL medium volume with different particle size and particle density.

Table 3.2 Results for N_{js} of Different Kinds of Solid Spherical Particles with Different Methods

Solution Volume	Particle Size	Particle Density	Impeller Type	Baffling Type	$N_{js\text{-}Ds\text{-}Method}$	$N_{js\text{-}As\text{-}Method}$	$N_{js\text{-}Visual}$
500mL	30	2.072	USP 2	UB	96	78	98
	20	3.197	USP 2	UB	164	131	170
	12	2.600	USP 2	UB	127	104	140
	11.3	1.830	USP 2	UB	38	32	40
	40.3	1.830	USP 2	UB	77	67	80
	112.5	1.830	USP 2	UB	110	84	102
	250.2	1.830	USP 2	UB	144	112	148
	40	2.332	USP 2	UB	140	101	148
	60	2.332	USP 2	UB	166	126	175
	75	2.332	USP 2	UB	226	173	235
900mL	30	2.072	USP 2	UB	160	86	108
	20	3.197	USP 2	UB	119	99	128
	12	2.600	USP 2	UB	109	93	114
	11.3	1.830	USP 2	UB	49	40	54
	40.3	1.830	USP 2	UB	88	77	89
	112.5	1.830	USP 2	UB	103	81	97
	250.2	1.830	USP 2	UB	151	114	158
	40	2.332	USP 2	UB	151	113	159
	60	2.332	USP 2	UB	167	128	170
	75	2.332	USP 2	UB	242	188	260

The results of N_{js} determined from D_S method and A_S method are plotted in Figure 3.4 and Figure 3.5. For different medium volume, different particle size and density, the N_{js} values predicted by regression of N vs. D_S (R^2>=0.995) were in excellent agreement with the visual N_{js} based on Zwietering's method. However, the regression lines of N vs. A_S resulted in lower R^2 values (R^2>=0.930). The difference between N_{js} predicted from A_S method and that from the visual method was significant, which means that the A_S method is not appropriate for this unbaffled USP Apparatus 2 vessel system. However, the D_S method appears to be a valid novel method to determine the N_{js} instead of the traditional Zwietering's method in the USP Apparatus 2.

The N_{js} values for all the experiments were then plotted in a same figure in order to better visualize these results from D_S method and A_S method. Parity plots are presented in Figure 3.6, which were generated using the N_{js} visual values vs. those obtained with the D_S method and A_S method, respectively.

These parity figures showed that the experimental points align on an angle line: the closer the points are on a 45 ° line the better agreement between the novel method and conventional method. The parity plot with the D_S method show that the data align themselves on such a line much more than the As method, indicating that in all experiments for different operation conditions, the values of N_{js}-D_S-method agreed very well with the visual data. The average deviation between Njs-Ds and Njs-visual was 2%.

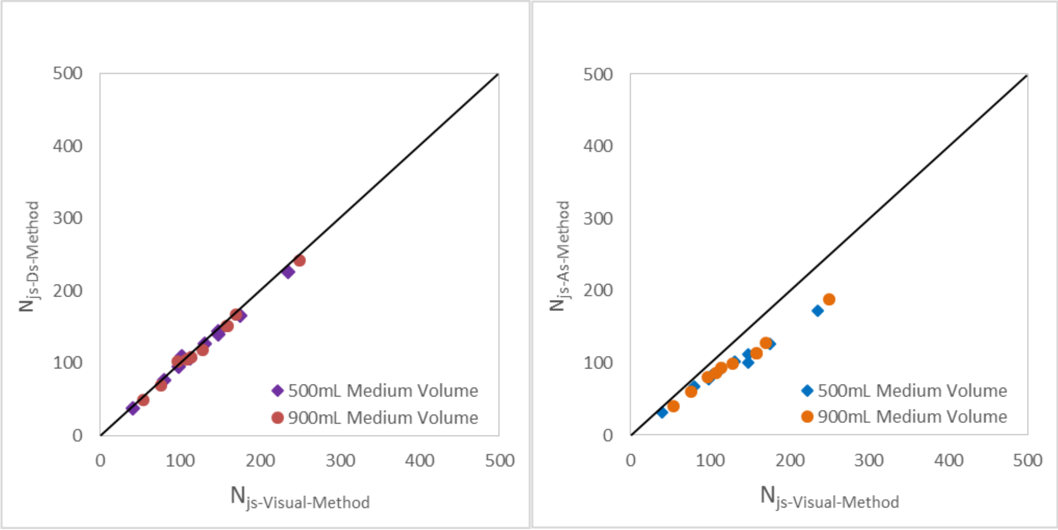

Figure 3.6 Parity Plots for all the experiments results for solution volume of 500mL and 900mL in USP Apparatus 2 system: Left panel Njs-Ds-Method data vs. Njs-visual-Method Data; Right panel: Njs-Ds-Method data vs. Njs-visual-Method data.

These parity plots show that the D_S method is more reliable as a novel method to obtain Njs and can produce much more accurate determination for N_{js} of the USP 2 system than the A_S method.

According to the pioneering work of Zwietering (1958), his data analysis resulted in an empirical expression for N_{js}:

$$N_{js} = S\frac{v^{0.1} d_p^{0.2} \left(\frac{g\Delta\rho}{\rho_L}\right)^{0.45} X^{0.13}}{D^{0.85}} \tag{3.1}$$

Base on this equation, S-values were obtained for USP 2 standard system by fitting the experimental N_{js}-D_S data to this equation using different sizes and densities of particles and 997.537kg/m^3 for water, respectively. The USP 2 system is usually operated with 500mL or 900mL solution volumes. Therefore, the S-value could be calculated for both of the different operating conditions, by fitting different particle properties with the Njs experiment results to the equation above. The operating and physical parameters for the USP 2 system is standard and as following: Cb which was the clearance of the impeller from the vessel bottom is 25mm, H is the liquid height which was 78.6mm and 131.2mm for 500mL and 900mL respectively, and T is the diameter of the vessel which is 100.16mm. The liquid volume associated with each liquid height are shown in Table 3.3. The S-values are listed in Table 3.4 under different operation conditions for different particles in the USP 2 system.

Table 3.3 Ratios of Cb/T and H/T for Different Operating Conditions in USP 2 System

Volume Systems	Impeller Clearance (Cb)	Liquid Height (H)	Vessel Diameter (T)	Ratio Cb/T	Ratio H/T
500	25mm	78.6mm	100.16mm	0.25	0.78
900	25mm	131.2mm	100.16mm	0.25	1.31

Table 3.4 Fitted Zwietering S-values for Different Solid Particles in USP 2 System

Particle Size	Particle Density	Cb/T=0.25 V=500mL	Cb/T=0.25 V=900mL
30	2.072	2.494639138	2.754497381
20	3.197	3.583896484	3.353541404
12	2.600	3.309284091	3.402943075
11.3	1.830	1.200276085	1.547724425
40.3	1.830	2.130941310	2.155434888
112.5	1.830	2.190206587	2.054565378
250.2	1.830	2.448038684	2.567040564
40	2.332	3.435008670	3.704902208
60	2.332	3.755689138	3.778313771
75	2.332	3.743222568	4.067779438

3.4 Conclusion

In this work, the minimum agitation speed for complete off-bottom solid suspension in the USP 2 vessel was experimentally obtained with two novel methods, i.e., the N_{js}- D_S-Method and N_{js}- A_S-Method [64]. Triplicates experiments were conducted and the experiments were highly reproducible. The results for Njs obtained with the Ds method agree well with the values of visualization method as shown by parity plots.

Conversely, the method based on A_S measurement resulted in significant difference with the data obtained with the visual method. The results obtained in this work showed that the novel method for determining N_{js} from previous work of our lab could also be used for the USP Apparatus 2 system. In summary, the novel method of N_{js}- D_S-Method could produce highly agreed results with the conventional method for the USP 2 system, which could be directly applicable to the pharmaceutical industry.

CHAPTER 4

COMPUTATIONAL AND EXPERIMENTAL DETERMINATION OF THE HYDRODYNAMICS OF MINI VESSEL SYSTEMS

4.1 Background and Objective

In recent years, dissolution testing has become a powerful tool to evaluate different drug formulations during the initial drug development stages and therefore to improve the whole product development process. For this purpose, numerous dissolution test devices exist, although the USP Apparatus 2 system is still the most commonly used device in industry, particularly for immediate release (IR) of solid dosage forms [94, 95]. Generally, successful dissolution testing during product development is preceded by the preparation of test drug products and is followed by drug analysis of the samples collected during the dissolution tests. The first step is often conducted in a standard dissolution apparatus, such as the classical USP 2 system.

However, this approach may not be appropriate for all dissolution situations, especially during the early stages of product development. For example, initially the availability of API is typically limited: therefore test drug products may contain only microgram or nanogram quantities of active ingredient. Upon dissolution in a conventional USP Apparatus 2 this in turn results in very low concentrations of the dissolved drug. Therefore, available analytical methods may not be sensitive enough for such low-dose dissolution testing, and this approach may not be practical to obtain reliable dissolution testing data. Low drug concentrations in the dissolving medium may additionally result from the development of more potent drug substances. Furthermore, for some bio-relevant studies during drug formulation, dissolution should be ideally conducted in a specific dissolution medium, such as the animal gastrointestinal medium, with a similar medium volume as in the animal physiology [96-100]. This may require large volumes of dissolution medium, with additional costs.

In order to overcome limitations in drug dissolution testing caused by low drug availability, novel high-potency low-dose compounds, analytical sensitivity, and the lack of bio-relevant dissolution medium or materials, standard dissolution devices such as the widely used USP Apparatus 2 system may not be fully appropriate for the task. A small volume apparatus is needed in such cases, and various types of miniaturized paddle apparatuses inserted in mini vessel systems have been developed to achieve this purpose. These apparatuses are scale-down versions of the standard USP Apparatus 2 system. The most common mini vessel system includes a small volume vessel (maximum to 200mL), a mini paddle impeller, and a small lid, as shown in Figure 4.1. However, before such a mini vessel system can be widely and reliably used in industry, dissolution tests conducted in such systems need to be shown to be accurate and reproducible. In addition, the operating characteristics of this device should be studied in greater detail, as is has happened before for the standard USP Apparatus 2, and the dissolution performance of mini vessel systems should be compared to that of the USP Apparatus 2 in order to be able to correlate the dissolution profiles obtained with the two systems and avoid duplication of tests.

Figure 4.1 Mini vessel dissolution apparatus system, including mini vessel, mini paddle impeller and small lid.

Although significant information is available in the literature on the standard USP Apparatus 2 system, the same is not true for mini vessel systems, which have been much more rarely studied. In addition, the hydrodynamics of mini vessels has not been studied at all, to the best of our knowledge, and the operating conditions for this system has not been defined. Furthermore, comparison of dissolution results obtained with mini vessel and with standard USP 2 apparatuses is lacking.

Therefore, the overall objective of this work was to determine the operating characteristics of mini vessels and compare them to those of the standard USP Apparatus 2 so that dissolution tests performed in this system could be “scaled down” without losing the reliability and the predictability of the standard method. This was accomplished in this work by conducting CFD simulations and PIV experiments to investigate the hydrodynamics of the mini vessel system shown in Figure 4.1. The hydrodynamics of mini vessel was studied at four different agitation speeds and the velocity distributions were compared with those in the standard USP Apparatus 2 system. CFD simulations were first conducted without a tablet on the bottom of the mini vessel. Special attention was paid to the determination of the velocity distribution in the region below the impeller in order to compare the fluid dynamic regime experienced by tablets in both the mini vessel system and the USP 2 apparatus.

Furthermore, CFD simulations for mini vessel system with non-disintegrating tablets centered at the vessel bottom were also conducted to predict the velocities and the strain rates on the surface of tablets. By using the velocity predictions from CFD method, the mass transfer coefficients for non-disintegrating tablets were also calculated, and these results were compared to those predicted in previous work by this group for the standard USP 2 system [7]. Mass transfer coefficients were obtained for different agitation speeds and compared with the standard system based on previous work by this group, in order to determine at which agitation speed mass transfer coefficient in the mini vessel and in the standard system are the closest.

4.2 CFD Simulation Method

4.2.1 System Geometry

The exact dimensions of mini vessel system studied here are presented in Table. 4.1 and Figure 4.2. These dimensions were obtained by direct measurements of experimental mini vessel provided by Merck Company, Summit, NJ, courtesy of Mr. Gerard Bredael. The paddle clearance used in this work is 10 mm, which is different from that used in the standard USP Apparatus 2 system. This is the clearance usually used in industry, and was also suggested by the manufacturer of the dissolution testing equipment (Distek Company).

Table 4.1 Dimensions of Impeller and Shaft in Mini Vessel System

Component of impeller or shaft	Dimension (mm)
Shaft Diameter	6.40
Length of Top Edge of Impeller Blade	27.58
Length of Bottom Edge of Impeller Blade	17.00
Height of Impeller Blade	8.08
Thickness of Impeller Blade	1.60

Simulations were conducted for systems in the absence and in the presence of a “virtual” tablet placed in the center of vessel bottom. In the latter case, a tablet with a diameter of 9.57 mm and a height of 2.71 mm was assumed.

4.2.2 Mesh

In the CFD simulations, the computational domain was discretized into a finite number of contiguous control volumes, and for each control volume the conservation equations of mass and momentum were solved. Therefore, the physical geometry of the mini vessel and mini paddle were modeled using the software GAMBIT 2.4.6.

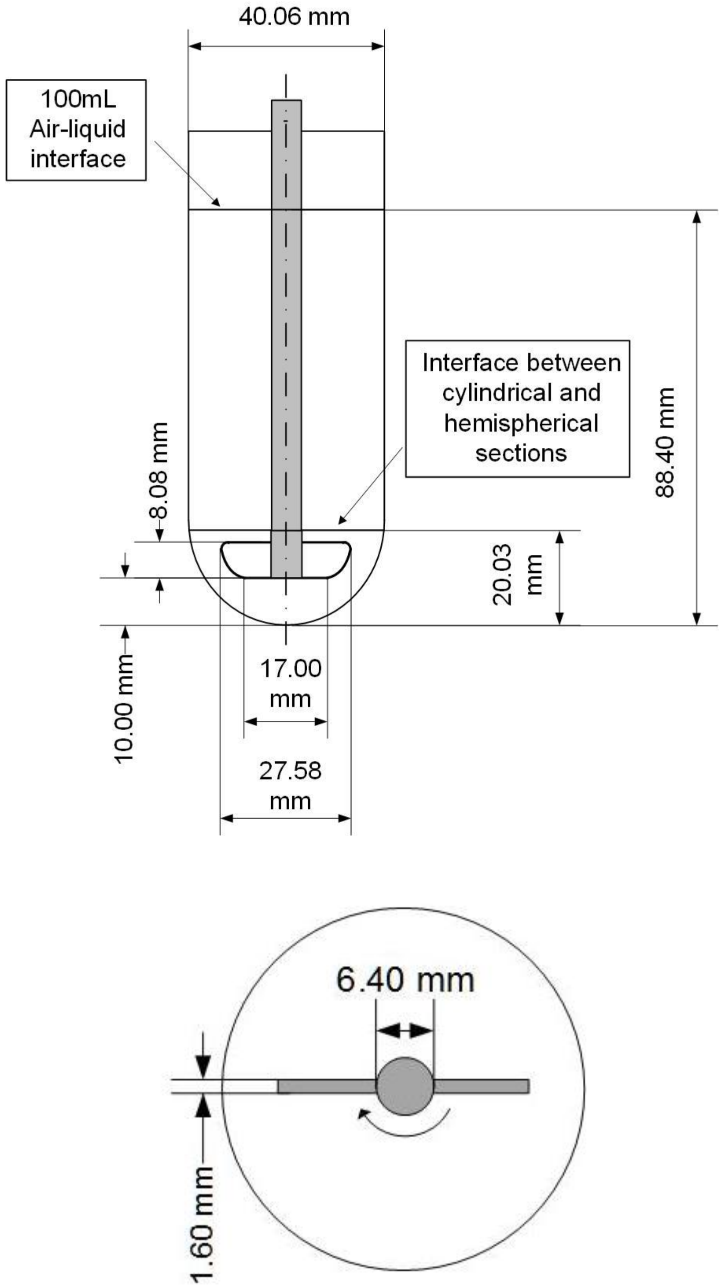

Figure 4.2 The dimensions of mini vessel and mini impeller used in this work.

In all simulations, a structured Cooper-type hex mesh was created for most parts of the vessel as shown in Figure 4.3. However, the vessel bottom section was meshed with an unstructured tetrahedral mesh because it could follow the curved shape more closely.

Significant attention was paid to constructing a high quality mesh, which directly impacted simulation time and convergence stability. The mesh not incorporating the tablet typically contained 97,603 cells, 281,004 faces and 88,175 nodes, while, the mesh with the tablet centered on the bottom of the vessel contained 96,450 cells, 276,861 faces and 88,019 codes. In both cases, the average EquiSize Skew parameter ranged from 0.3 to 0.4 (0-best; 1-worst), which was one of the most important parameters to determine the mesh quality. No individual cell had a value of this parameter larger than 0.748. The meshes for both of the two cases are shown in Figure 4.3.

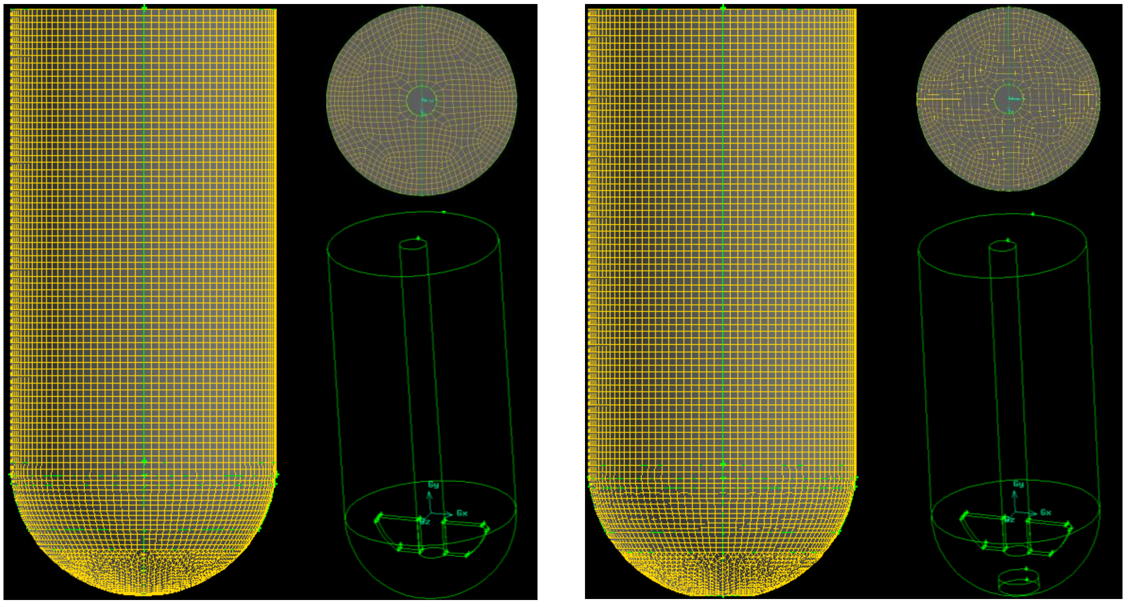
(A) (B)

Figure 4.3 Mesh structure of mini vessel system generated by GAMBIT software: (A) mini vessel system without tablet; (B) mini vessel system with tablet in the center of bottom.

4.2.3 Turbulence Model and Reference Frame Method

Simulations were conducted in FLUENT 6.3.26. A number of different turbulence models can be incorporated in the simulations, such as the k-ω model with low Reynolds number correction, RNG k-ε model, and Realizable k-ε model. In previous study by this group [6] it was shown that the k-ω model with low Reynolds turbulence model resulted in the most accurate results for the USP Apparatus 2. Therefore this turbulence model was chosen here to model mini vessel systems.

The single reference frame (SRF) approach was used, because the systems (with or without tablet) are all symmetric. Accordingly, the wall and tablet were assumed to be rotating, while the impeller was stationary. In order to represent correctly the flow in the real system (where the impeller is actually rotating) the simulations included the non-inertial forces appearing in the rotating frame of reference.

4.2.4 Boundary Conditions and Additional Details of the Simulations

In the simulations for the two systems, the boundary conditions were as following: the no-slip condition was assumed at all solid surfaces; the air-water interface was assumed to be flat, and was modeled as a frictionless surface, i.e., the normal gradients of all variables are zero at this interface. Simulations were conducted at agitation speeds equal to 50rpm, 100rpm, 125rpm, or 200rpm.

All simulations were carried out on a MacBook Pro, equipped with Intel Core I7-3615QM CPU and 16 gigabytes of random access memory (RAM). A typical simulation required 28000 iterations and about 7 h of CPU time to achieve conversion. The simulation results were compared with the PIV measurements, and were also used in the mass transfer coefficient study.

4.3 Experimental PIV Measurements of Velocity Distribution

PIV experiments were conducted as mentioned in the previous chapter. A Dantec FlowMap 1500 2D Particle Image Velocimetry (PIV) apparatus (Dantec Dynamics A/S, Tonsbakken 16-18, DK – 2740 Skovlunde, Denmark) was used to measure the velocity distribution on the 2D central plane inside the vessel. Silver-coated hollow borosilicate glass spheres (Dantec Measurement Technology USA, Mahwah, NJ, USA) with density of 1.4 g/cm^3 and size range from 2 to 20 μm (mean particle size: 10 μm) were used as seed particles to follow the fluid flow and scatter the laser light for flow velocity measurement.

For the mini vessel system, which is a symmetric system, it was assumed that the hydrodynamics of medium flowing was the same on each cross section of the vessel, therefore, velocity map on only one cross plane needed to be measured, as shown in Figure 4.4. For each agitation speed, three repeated experiments were conducted, each consisting of taking 200 image pairs to obtain the average velocity distribution. The results were averaged and plotted with the standard error bar also shown.

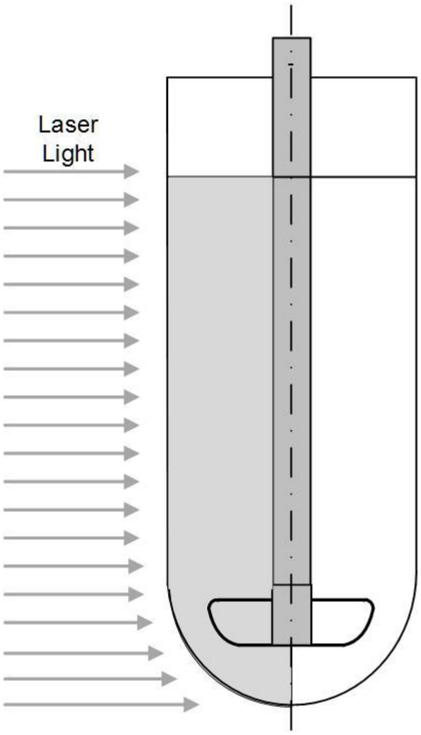

Figure 4.4 The cross section in the middle of mini vessel for PIV measurements.

In order to compare the experimental PIV results with the simulation prediction, six horizontal surfaces (iso-surfaces) were selected inside the vessel, as shown in Figure 4.5. The lowest point at the bottom of the vessel was defined as Y=0 mm. Two of the iso-surfaces were located above the impeller, i.e., at y = 62 mm and y = 38 mm; one iso-surfaces in the impeller region, i.e., y = 16 mm; and the other three planes below the impeller, i.e., y = 9 mm, y = 6 mm, and y = 3 mm.

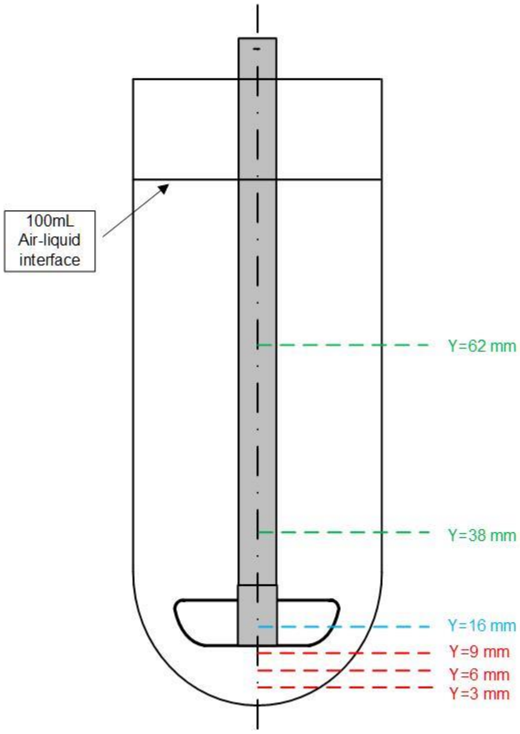

Figure 4.5 Iso-surface lines inside the mini vessel for axial and radial velocity comparison of CFD and PIV results.

For each iso-surface, the radial velocity and axial velocity obtained from PIV measurements and also from CFD predictions were scaled by the tip velocity, and compared with each other at each agitation speed. In the hydrodynamics comparison between mini vessel and the standard USP 2 system, the absolute values of the velocity were compared in order to determine the flow field around the tablet in both cases.

4.4 Mass Transfer Model

In order to fully compare the mini vessel system and the standard USP Apparatus 2 system, not only the hydrodynamics and strain rate were analyzed, but the tablet-medium mass transfer process was also modeled. The mass transfer coefficient was calculated for each agitation speed and compared with the corresponding values previously calculated for the standard USP Apparatus 2 system [7]. This approach enabled us to compare the two systems and help determine under which operating conditions the two systems can be expected to generate similar dissolution profiles bases on similar mass transfer rate at the tablet surface.

In this theoretical modeling approach, the rotating disk model was used to predict the mass transfer process occurring at the tablet top surface between the tablet and the surrounding fluid, although in this study the tablet is stationary at the vessel bottom and the incoming fluid is rotating. Since this mass transfer model is based on boundary layer theory, the velocity of the fluid flowing around the tablet needed to be used as an input. Therefore, the velocity prediction from CFD simulation for non-disintegrating salicylic acid tablet centered in the mini vessel bottom could be used as an input in this mass transfer computation. The rotating disk model predicts that the mass transfer coefficient on the top surface of a tablet is the same as that on the surface of rotating disk [101, 102]:

$$k_{top} = 0.62 D_{AB}^{2/3} \upsilon^{-1/6} \omega^{1/2} \tag{4.1}$$

Where k_{top} is the mass transfer in m/s, D_{AB} is the diffusivity between the solute and the solvent in cm^2/s, υ is the kinematic viscosity of the liquid in cm^2/s, and ω is the angular velocity of the rotating disk in rad/s.

The rotating disk model requires the knowledge of some of the physical properties or the fluid and the dissolving solids (salicylic acid). The diffusivity of the salicylic acid in water was estimated from Wilke-Chang correlation [102, 103]:

$$D_{AB} = 1.173 \times 10^{-16}(\Phi M)^{1/2}\frac{T}{\mu V_A^{0.6}} \tag{4.2}$$

Where M is the molecular weight of the water which is equal to 18.02 kg/kg-mol, Φ is an association parameter of the solvent (2.6 for water), T is the temperature (310 K), V_A is the solute molar volume at its normal boiling point (0.09592 m^3/kg-mol in this study, assuming the molar volume of salicylic acid at boiling point is the same as that at room temperature). After substituting the diffusivity value D_{AB}, for salicylic acid–water system was then calculated to be 1.47×10^{-5} cm^2/s.

The kinematic viscosity of water (at 37 °C) was used for υ, which was 0.70×10^{-2} cm^2/s and ω was calculated from the tangential velocity of the fluid layer which was the closest fluid layer to the top of tablet, which is :

$$\omega = \frac{u_{\Omega}}{r} \tag{4.3}$$

Where u_{Ω} is the tangential velocity of fluid layer just above the tablet for 1mm, and r is the radial distance between the fluid location and the vessel centerline.

In addition, the mass transfer coefficient of the side surface of the tablet was predicted as well. It was assumed that this process was similar to the mass transfer between a rotating cylinder and the surrounding fluid, although the tablet was stationary and fluid was rotating. In the rotating cylinder model, the mass transfer coefficient k_{side} was calculated as following [104]:

$$\frac{k_{side} d_T}{D_{AB}} = 0.135[0.5 Re_{\Omega}^{2} Sc]^{1/3} \tag{4.4}$$

Where d_T is the diameter of tablet, D_{AB} is defined as mentioned above, Sc is the Schmidt Number, and Re is the Reynolds number, defined representatively as [101, 103]:

$$Sc = \mu/(D_{AB}\rho_L) \tag{4.5}$$

$$Re_{\Omega} = \frac{d_T u_{\Omega} \rho_L}{\mu} \tag{4.6}$$

Where u_{Ω} is the tangential velocity of the medium at the periphery of the tablet for 1mm obtained from CFD simulation. The properties of the tablet and medium (water) are summarized in Table 4.2.

Table 4.2 Properties of Salicylic Acid Tablet and Medium (Water) Used in the Mass Transfer Coefficient Prediction

Diameter of tablet	d_T	9.57×10^{-3} m
height of tablet	h_T	2.71×10^{-3} m
Density of water	ρ_L	995.73 kg/m^3
Viscosity of water	μ	6.92×10^{-4} kg/ms
Diffusivity of the salicylic acid in water	D_{AB}	1.47×10^{-5} cm^2/s
Association parameter of the solvent (water)	Φ	2.6
Molecular weight of the water	M	18.02 kg/kg-mol
Solute molar volume	V_A	0.09592 m^3/kg-mol
Kinematic viscosity of water	υ	0.70×10^{-2} cm^2/s

k_{top} and k_{side} could be predicted by this mass transfer model using as input the velocities obtained from the CFD simulations. Furthermore, the area-average k_{prd} for the entire tablet-medium mass transfer coefficient could be calculated from k_{top} and k_{side}, which was calculated as follows:

$$k_{prd} = \frac{k_{top}A_{top} + k_{side}A_{side}}{A_{top} + A_{side}} \tag{4.7}$$

Where A_{top} and A_{side} are the top and side surface area of the tablet, which could be calculated from the tablet dimension. k_{prd} was the entire mass transfer coefficient predicted for the salicylic acid tablet-medium, which could be also compared with that of standard system.

4.5 Results

4.5.1 CFD and PIV Results Comparison of Mini Vessel System

Velocity Contour and Vectors. The CFD simulation results were compared and validated with the PIV measurements for the four agitation speeds in mini vessel system. Figure 4.6 presents the overall contour map from CFD simulations, and Figure 4.7 shows the velocity vectors from CFD predictions and PIV measurements. All of these results were generated on a vertical cross section through the middle of impeller shaft.

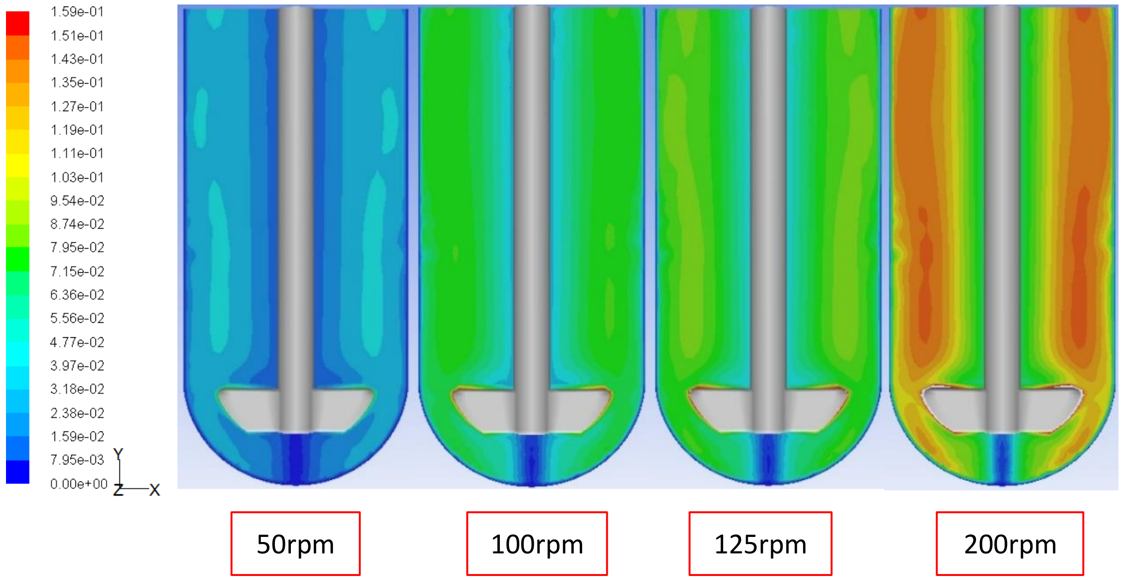

Figure 4.6 CFD predictions of the velocity magnitude on a vertical cross section through the impeller shaft at 50rpm, 100rpm, 125rpm, and 200rpm. The tip velocity at those agitation speeds were 0.0788 m/s, 0.151m/s, 0.182m/s, and 0.287m/s, representatively. Velocities equal to, or higher than, 0.159 m/s are represented by the red color.

In general, the overall flow velocity magnitude increased with the agitation speed. However, the velocities in the inner core region below the impeller, where the tablet is typically located, were still very low, as represented by the blue color. Although the velocity in inner zone increased slightly with increasing agitation speed, the extent of increase was lower than anywhere else inside the vessel.

A comparison of the velocity vector results obtained with both CFD and PIV, shown in Figure 4.7, indicate that the predicted general flow pattern was similar to that measured at each agitation speed. Additionally, the fluid flow pattern was somewhat similar to that of the standard USP 2 system shown in previous work [6]. In all the CFD and PIV results, one can see that the impeller agitation produced a horizontal radial fluid jet that impacted the vessel wall and then formed upward flow and downward flows. The upward fluid flow resulted in a re circulation loop in the axial direction above the impeller. The downward flow below the impeller zone was more complex. In the vessel bottom, the downward flow which originated form the radial jet caused by the impeller rotation formed a recirculation flow loop in outer flow zone under the impeller and closing back in the center of the vessel, under the impeller. This flow loop magnitude increased as the agitation speed increased, because it was originated by the impeller agitation flow jet.

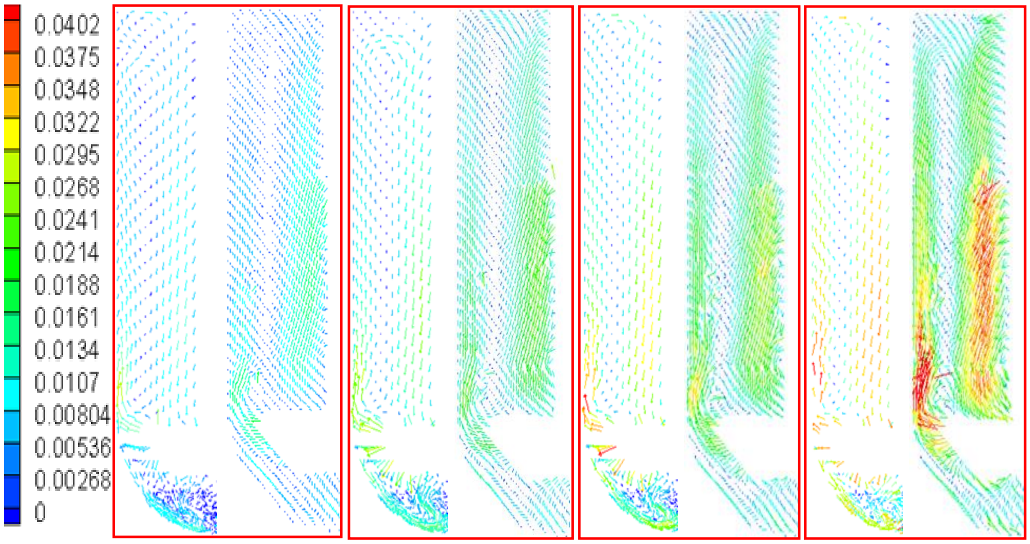

50rpm 100rpm 125rpm 200rpm

Figure 4.7 Velocity vectors of 2D on the cross section from CFD simulation and PIV measurements in mini vessel system at four agitation speeds of 50rpm, 100rpm, 125rpm, and 200rpm.

However, this downward outer flow loop did not penetrate the inner core zone which was just under the impeller, implying that the flow in the inner zone was still weak and unstable. The velocities in this inner zone were slightly higher at higher agitation speeds, as shown in CFD and PIV results, but this appears to be a common feature of the flow velocity in this system, independently of the agitation speed. This region was the most important zone in the vessel because it is usually where the tablet is located.

Figure 4.17 clearly shows that the overall flow in the mini vessel system is dominated by a strong tangential flow caused by the absence of baffles and the central location of the paddle agitator. In order to compare the results from the CFD and PIV methods for the mini vessel system, the axial velocity and radial velocity were plotted on each iso-surface at different agitation speeds, as shown next.

Velocity Profiles. Figure 4.8 and Figure 4.9 present the axial velocity and radial velocity on each iso-surface for different agitation speeds, as obtained by CFD simulations and PIV measurements. In these figures, the ordinates represent the axial velocity or the radial velocity, and the abscissas represent the radial position from the center of the vessel.

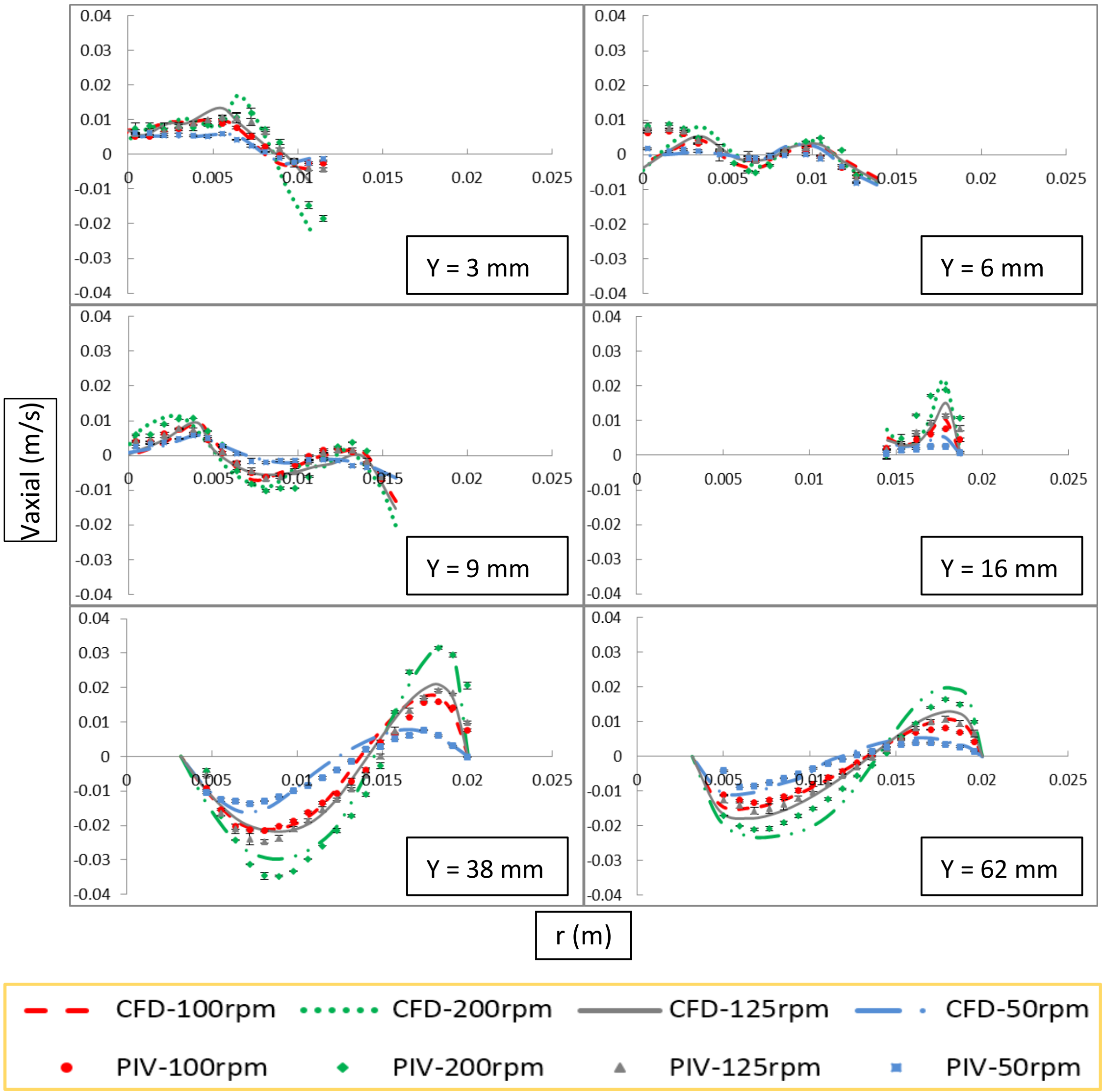

Figure 4.8 Comparison between CFD prediction and PIV experiment for axial velocities on different iso-surfaces at agitation speeds of 50, 100, 125, and 200 rpm.

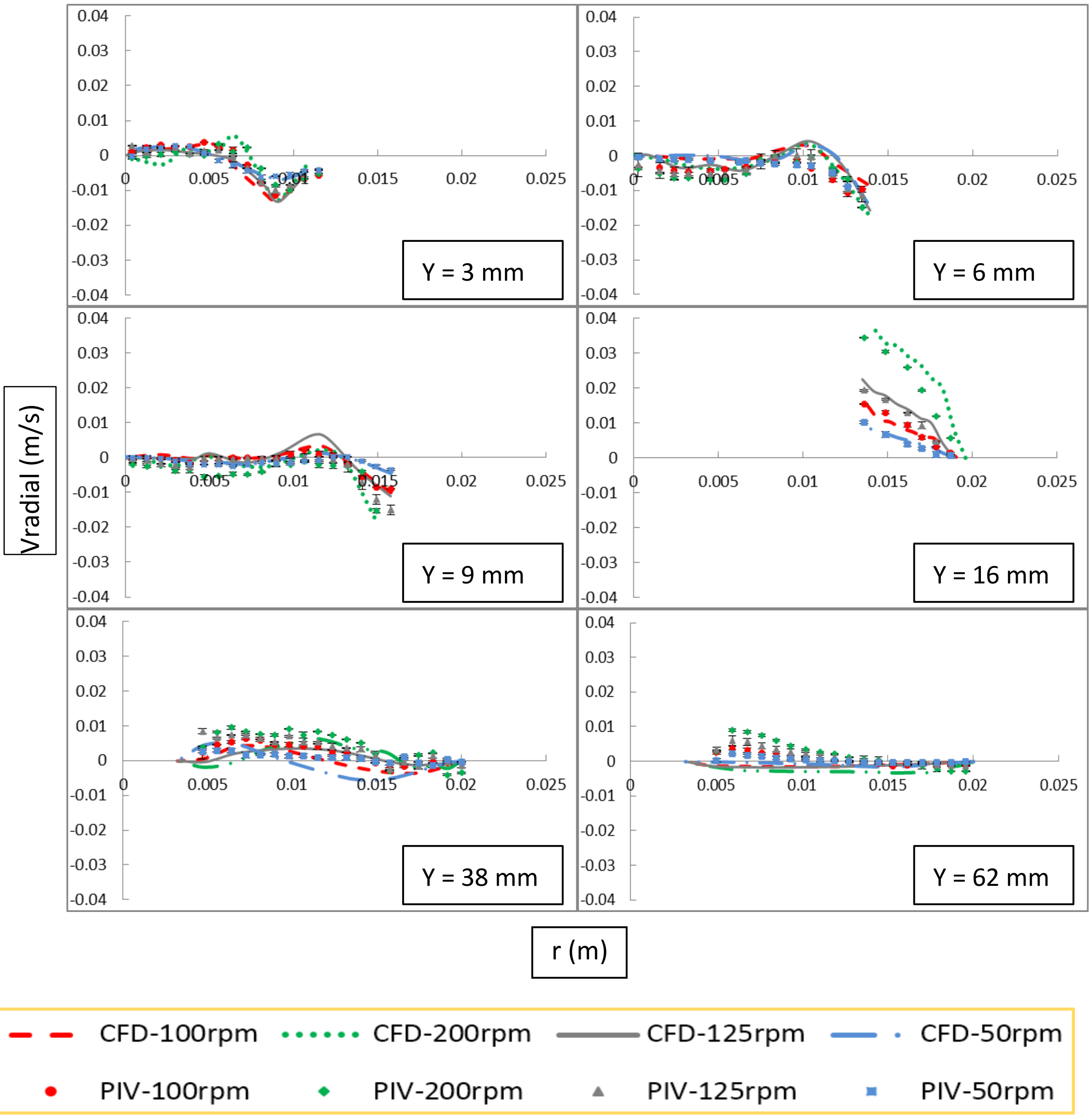

Figure 4.9 Comparison between CFD prediction and PIV experiment for radial velocities on different iso-surfaces at agitation speeds of 50, 100, 125, and 200 rpm.

In the region above the impeller, the axial velocity was negative for r < 0.015 m, which was about a 75% portion of the radius in mini vessel. In the outer region (0.015 m<r< 0.020 m), the velocity became positive. This indicated the presence of a recirculation loop above the impeller, where the upward fluid coming from the impeller rotation flowed along the vessel wall, then formed a loop and flowed downward in the center of the vessel converging back to the impeller area. The flow was qualitatively similar at all four agitation speeds, but the velocity intensity increased as the agitation speed increased. The radial velocity in the above impeller zone were smaller than the axial velocity, since the circulation loop here was driven by the axial velocity, as indicated by the velocity vector map in Figure 4.7. For each agitation speed, the CFD and PIV results generally agreed well.

In the region around the impeller, the vertical flow was split when the fluid jet impacted the vessel wall, generating an upward flow in the top portion of the vessel and a downward flow below the impeller. The iso-surface in this zone was at y = 16mm, where the fluid flow was dominated by the upward flow. Therefore the axial velocity started at zero at the impeller tip, and increased rapidly in the positive direction with radial distance, indicating that an upward flow was generated next to the wall. The radial velocity started from the highest value at the impeller tip as the fluid was pushed away toward the wall. As the radial distance from impeller to the vessel wall increased, the radial velocity became increasingly smaller and went to zero at the wall where the fluid flow split. The axial and radial velocities clearly increased as the agitation speed increased, also verified by the PIV experiment results.

In general, good agreement between the PIV results and the CFD predictions was observed. Some differences could be observed in region of extremely low velocities or when the flow direction changed rapidly over very small distances, as, for example, in the gap region between the impeller blade and the wall, where even moving upwards or upward by millimeters involves rapid changes in the velocity profiles.

For the region below the impeller, which was the most important zone in the dissolution test, the CFD results were compared with PIV data on the iso-surfaces at Y=3mm, 6mm, and 9mm. For most of them, the simulation and experiment were in agreement. As mentioned before, the velocity just below the impeller increased slightly as the agitation increased, but not as much as in the zone around impeller and above the impeller. The inner core zone was not penetrated by the flow, and the velocity there was still very low at any agitation speed, as shown in Figure 4.8 and Figure 4.9. Moreover, the fluid flow in this vessel is dominated by the tangential flow component. Therefore, the tangential flow velocities increase much more directly with the agitation speed, as shown in the velocity contour maps of Figure 4.6.

4.5.2 Hydrodynamics Comparison between Mini vessels and the Standard USP 2 System

By comparing the results obtained here and those obtained previously by our research group for the standard USP Apparatus 2 (from Chapter 2) one can see that significant similarities exist between the flow patter in the mini vessel system and the standard USP Apparatus 2 system. This is additionally shown in Figure 4.10.

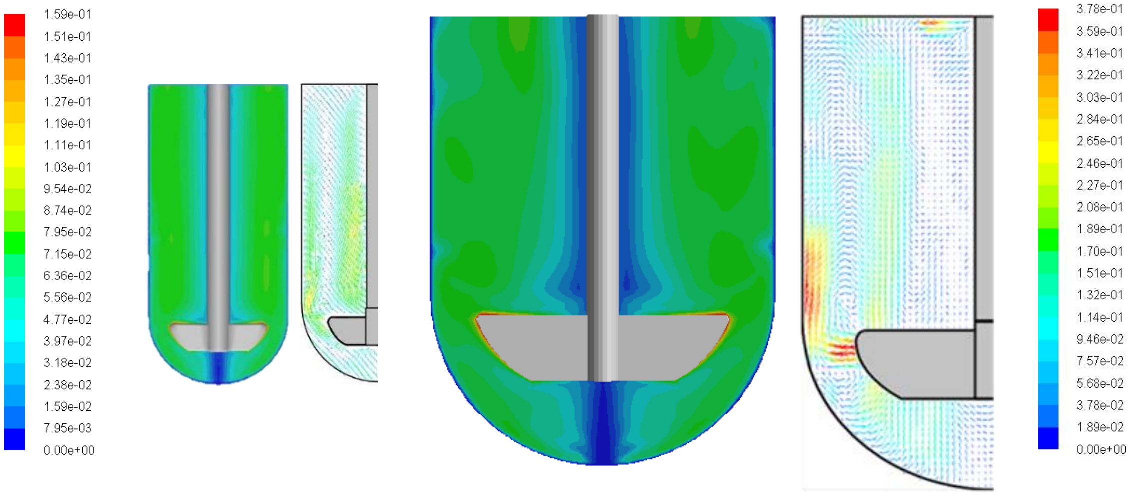

Figure 4.10 Velocity contour maps comparison between two systems of CFD prediction and PIV experiment at agitation speeds of 100rpm in mini vessel system and 100rpm in standard system.

The velocity profiles in the two systems can be compared. The axial and radial velocities were scaled by the tip speed for each system, at the same relative iso-surfaces for each system, scaled by the radius for system (i.e., Y/R), as shown in Table 4.3 and Figure 4.11. The CFD-predicted scaled axial velocity and radial velocities for the two systems are compared in Figures 4.12 and 4.13.

Table 4.3 Different Iso-Surfaces in the Two Systems at the Same Y/T Ratio

Ratio of Y/R	Mini Veseel System	Standard USP 2 System
	Iso-Surface Absolute Height (mm)	Iso-Surface Absolute Height (mm)
0.15	3	7.5
0.3	6	15
0.45	9	22
0.79	16	40
1.89	38	95
2.19	44	110

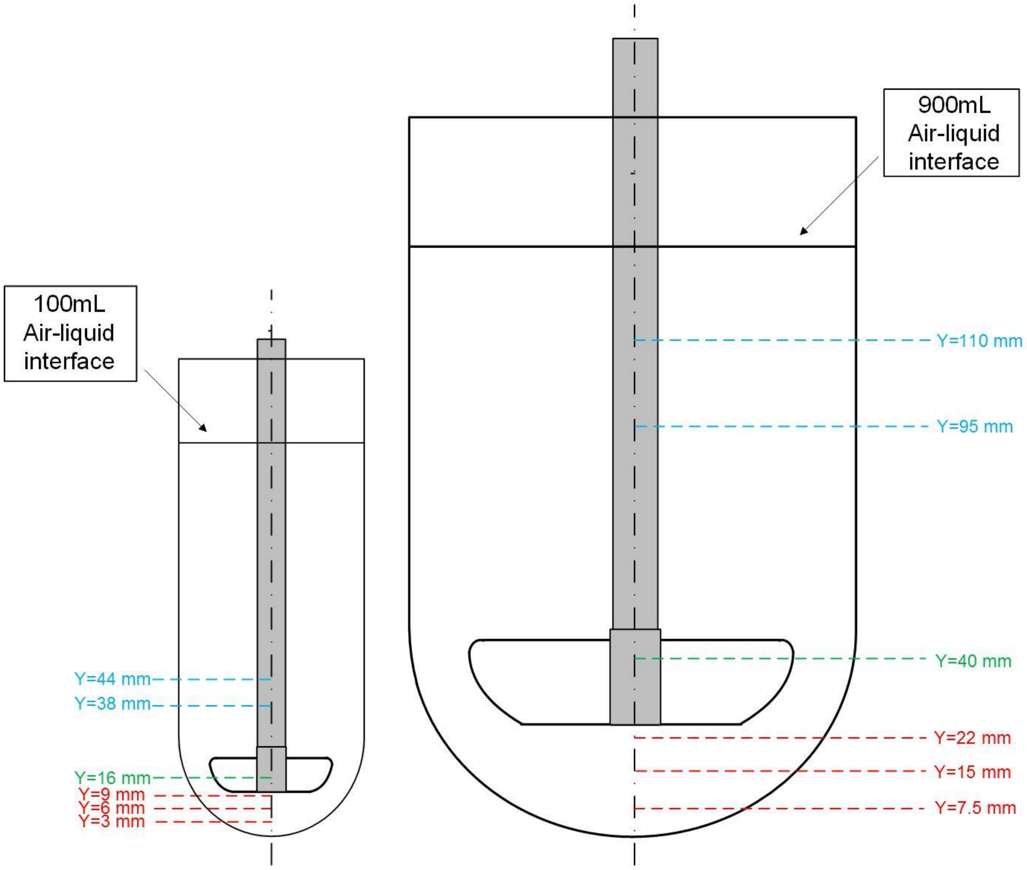

Figure 4.11 Iso-surface lines inside the mini vessel and standard USP 2 system with the same Y/R ratio.

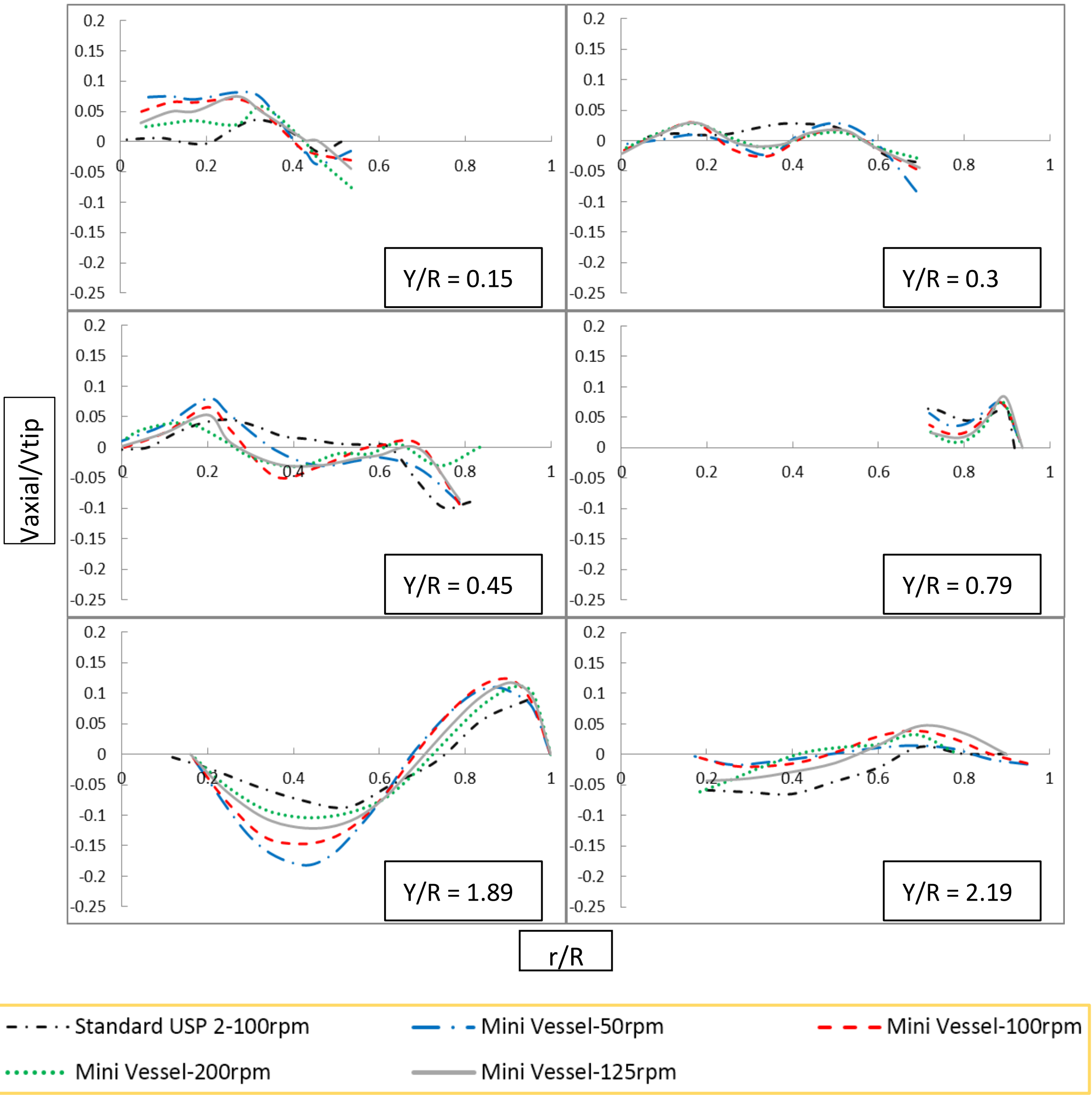

Figure 4.12 Comparison between mini vessel and USP 2 standard system of CFD results for scaled axial velocities on the iso-surfaces with the same Y/R ratio.

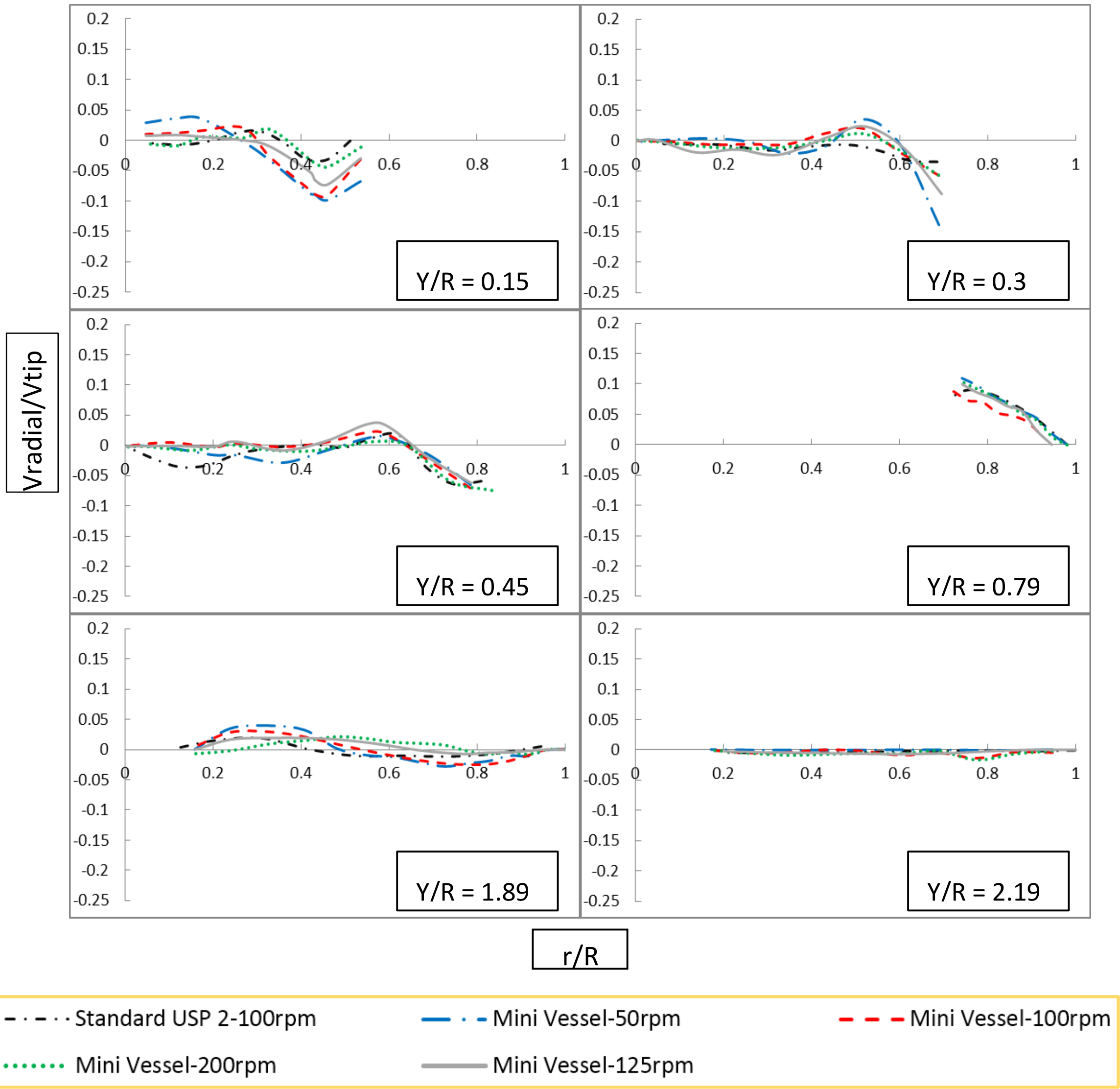

Figure 4.13 Comparison between mini vessel and USP 2 standard system of CFD results for scaled radial velocities on the iso-surfaces with the same Y/R ratio.

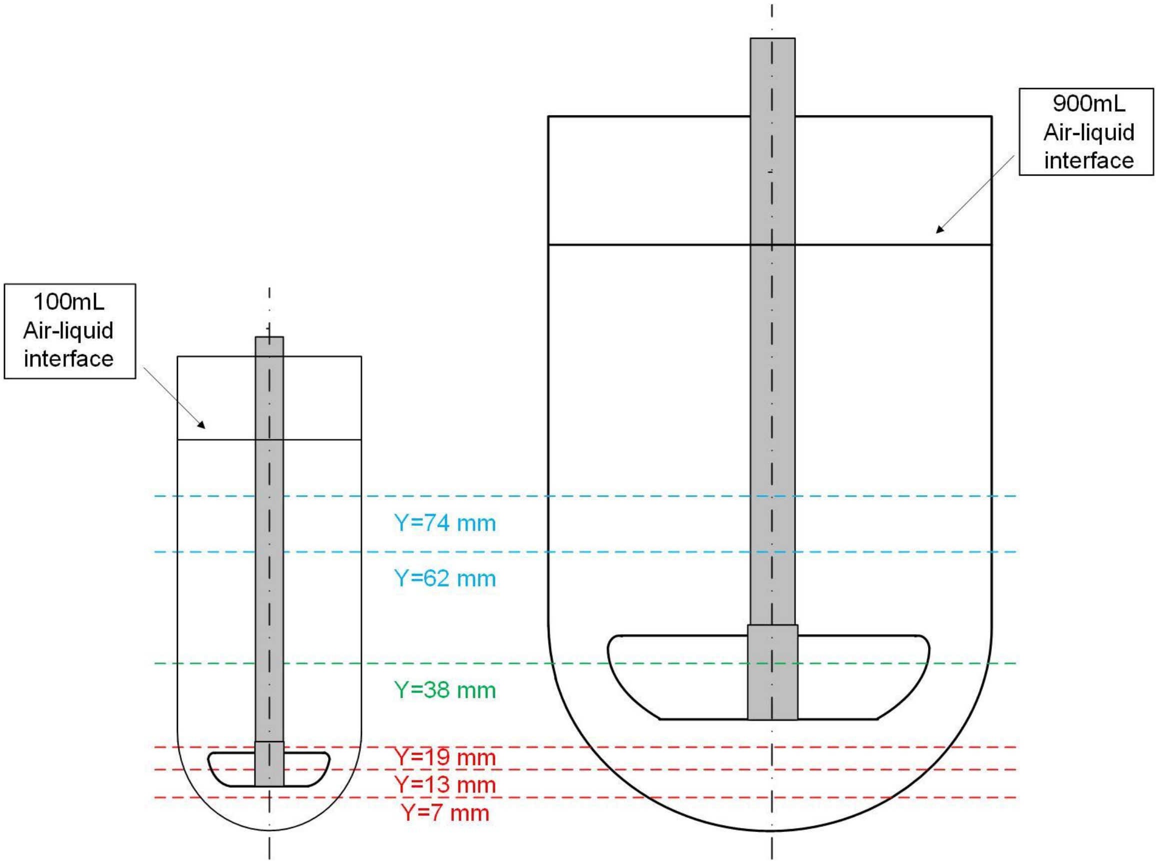

Figure 4.14 Iso-surface lines inside the mini vessel and standard USP 2 system for velocity comparison.

In addition, the actual values of CFD-predicted axial velocity and radial velocity were compared for the two systems shown in Figure 4.15 and 4.16 on six iso-surfaces. Because the different impeller clearance distance of the two systems, some iso-surfaces were not in the same zone of the two systems. For example, as shown in Figure 4.14, the iso-surfaces a Y=13mm and Y=19mm were in the impeller zone in mini vessel, but were in the bottom zone of standard system. The velocity in these iso-surfaces may have very different trend, but they were still plotted and compared between two systems as shown in Figures 4.15 and 4.16.

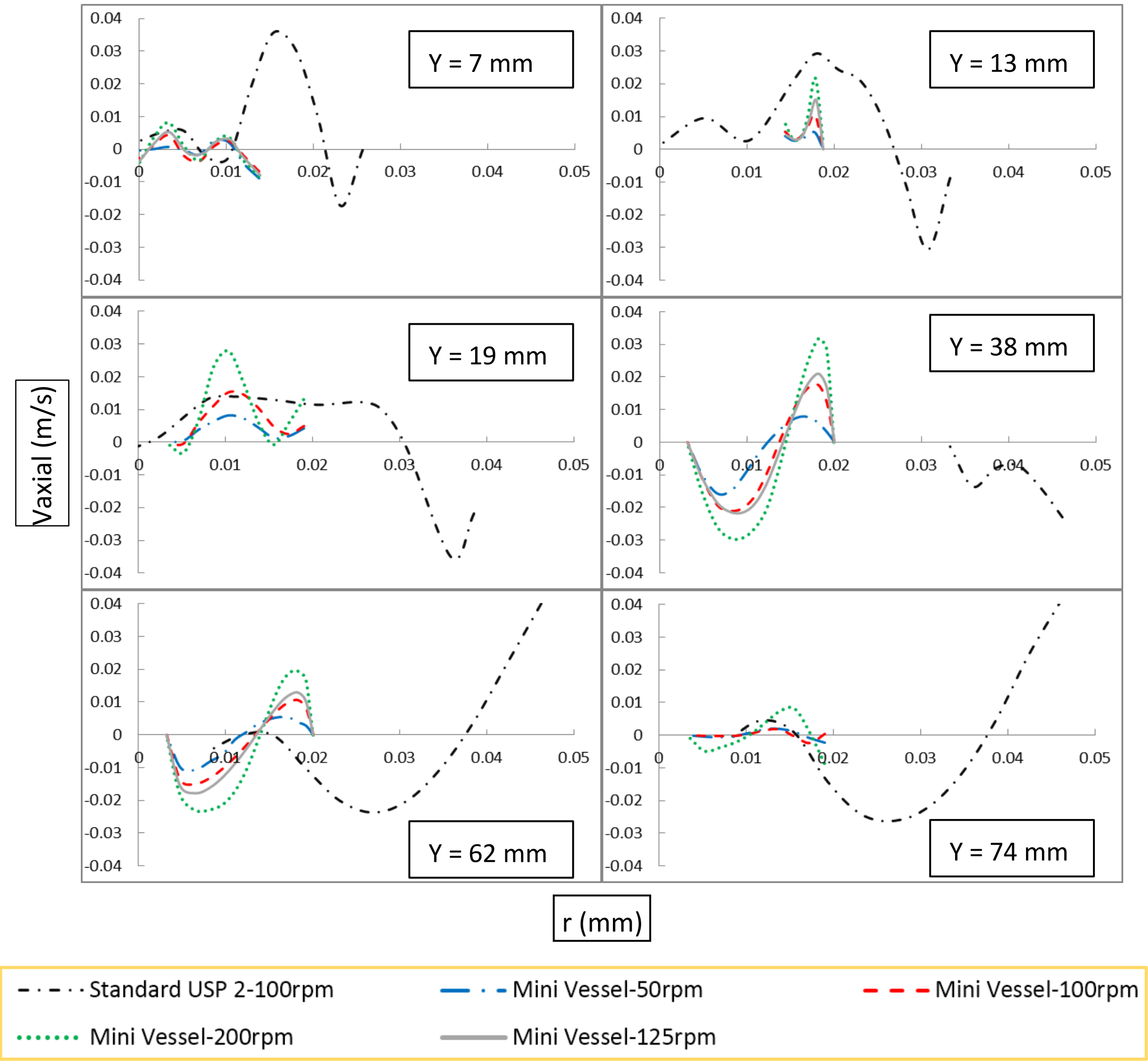

Figure 4.15 Comparison between mini vessel and USP 2 standard system of CFD results for actual axial velocities on different iso-surfaces.

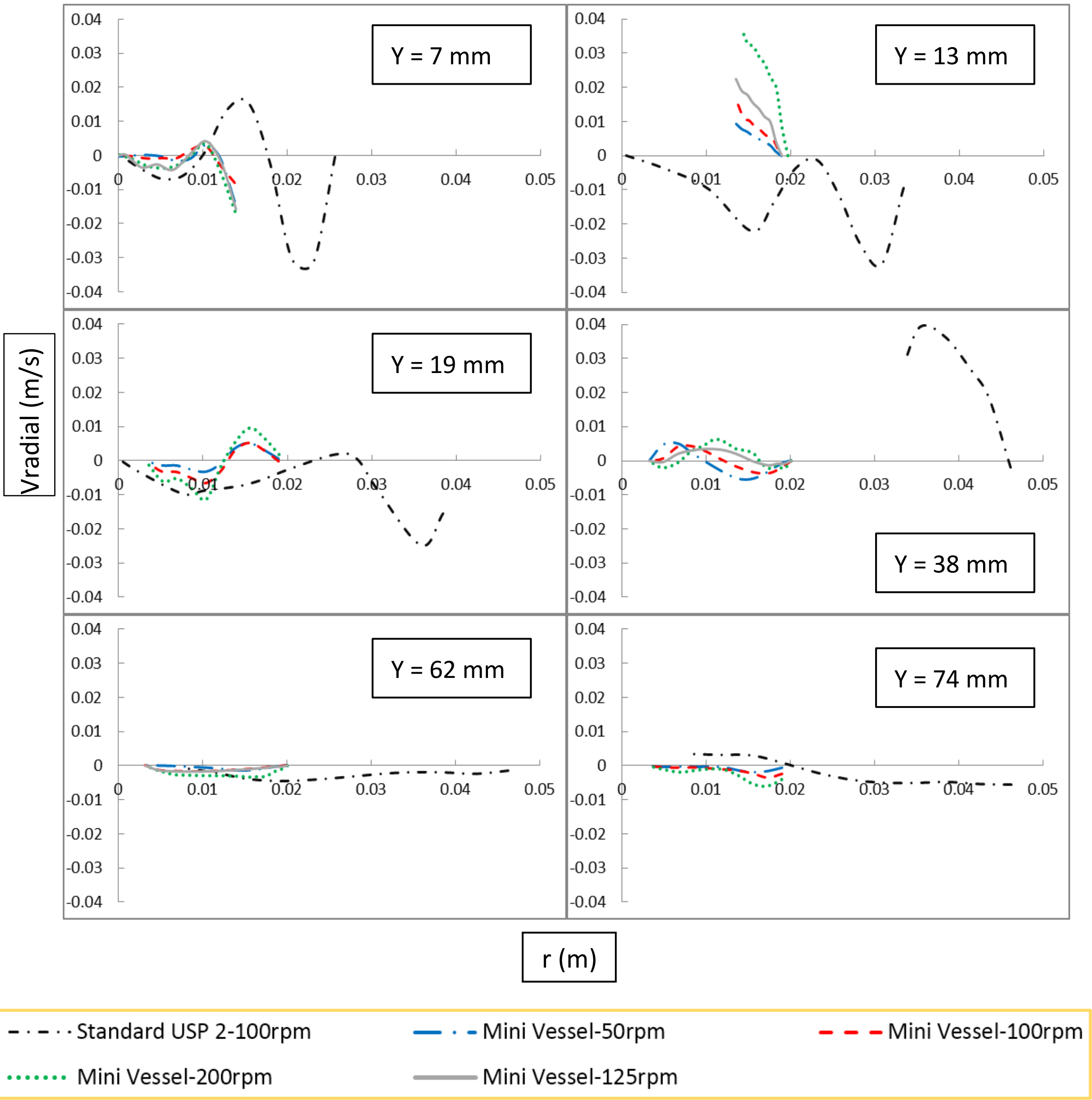

Figure 4.16 Comparison between mini vessel and USP 2 standard system of CFD results for actual radial velocities on different iso-surfaces.

On the iso-surfaces at Y=62mm and Y=74mm, i.e., above the impeller in both systems, the velocity were distributed in a smaller radial distance in mini vessel than the standard system because of its smaller vessel size. For the mini vessel, the velocity for r/R<0.02m included the entire flow loop velocity from the impeller to the vessel wall, but for the standard system, it was only a small portion of the entire flow loop which was about 40% of the whole radial distance. Although only the velocities for r/R<0.02m could be compared between the two systems, it indicated that the axial velocity was weaker in the mini vessel than in the standard system. For r/R<0.02m, the axial velocity was close to zero in the mini vessel, and in standard system the axial velocity increase then decrease in the positive direction which was also a small turbulence. However, for r/R >0.2m, the standard system had a large increase in the axial velocity in the negative direction and then become positive. The axial velocity in this radial distance was more than three times than that in mini vessel, which indicated the standard system had a stronger flow above the impeller. The radial velocities for these two iso-surfaces were close to zero in both systems, indicated a very weak radial velocity in this zone which was dominated by the flow loop upwards along the vessel wall and then flow downwards around the impeller shaft.

On the iso-surface at Y=19mm, which was just a little above the impeller in mini vessel but near the bottom in the standard system, the axial and radial velocities depended on the agitation speed. As the agitation speed increased, the axial and radial velocity obviously increased. Because this iso-surface was near the bottom in the standard system, the flow trend was different between two systems, but the magnitude was similar. The iso-surface at Y=13mm was in the impeller zone in the mini vessel but in the bottom zone in the standard system: therefore the velocity distribution was very different in the two systems. The axial velocity in the mini vessel was negative because of the downwards flow to the bottom zone. Because the velocity in this zone was driven by the impeller agitation, the velocity depended strongly on the agitation speed in the mini vessel. The velocity distribution was very different in the two systems because of different relative location of the the iso-surface. On the iso-surface Y=13mm and Y=19mm, the velocity had different trend in two systems, but the same magnitude, therefore it could not generate a dramatic effect on the dissolution test.

The most important zone for both systems is the inner bottom zone where a tablet may be located irrespective of which system is used. Therefore, it is important to examine this zone in greater detail and determine what velocity distribution profile the two systems generate. On the iso-surface at Y=7mm, which was near the bottom for both systems, the axial velocity was generally positive, generating an upward flow below the impeller in mini vessel and a similar trend in the standard system. When the radial distance was closer to the vessel wall, the axial velocity became negative in both systems, implying a downward flow near the wall, which originated from the impeller.

As shown in Figure 4.15, the velocity could be plotted only for r<0.013m in mini vessel because of the presence of the wall. The standard system had a relative weak flow for r<0.013m compared to the r>0.015m. However, the most important zone was the zone closer to the central position because most tablet tablets do not have radii on the order of 0.013 mm. Therefore, the velocity distribution for r<0.013m can be expected to be very important for dissolution testing in both systems. For this reason, the absolute axial and radial velocities at Y=7mm are re-plotted in Figure 4.17.

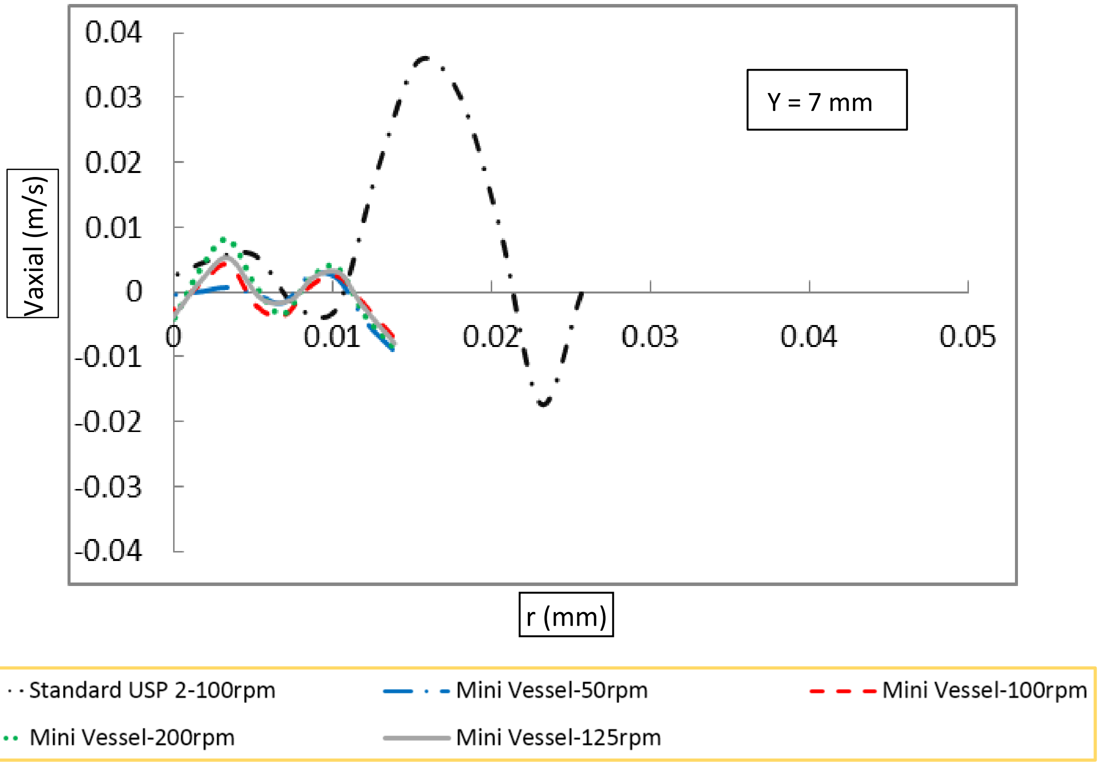

Figure 4.17 Comparison between the CFD results for axial velocities on the iso-surfaces at Y = 7mm in the mini vessel and the USP 2 standard system.

In this zone, around r=0.004mm, the axial velocities for 50 rpm and 100rpm in the mini vessel systems were typically smaller than in the standard system. At 125rpm, the velocities in the mini vessel were close to those in the standard system, and for 200rpm they were larger than in the standard system. However, in general, for N>100 rpm the axial velocities in the mini vessel systems were on the same order of magnitude as those in the USP 2 system in this inner core zone. This may imply that a tablet at the center of the vessel could experience a similar fluid velocity distribution around its side surface, which could direct affect the tablet-medium mass transfer process.

In addition, as the agitation speed increased in mini vessel, the axial velocity increased more sharply and quickly, and the radial distance where the first peak appeared decreased. This indicated that the inner core zone area shrank as the agitation speed increased in the mini vessel. As shown in Figure 4.11, the axial velocity had a second peak in both systems, which indicated the presence of an outer flow loop in the bottom zone. It was interesting that in the mini vessel, the two peak axial velocity values where similar in intensity, whereas in the standard system the first peak was much smaller than the second peak, indicating that in the standard system the inner core zone velocity was much smaller than the outer flow loop velocity. Therefore, in the mini vessel system, the axial velocity in inner core zone was enhanced because it reached the same value as the outer bottom zone. This may be because in mini vessel system, the impeller clearance distance was only 10mm which was much smaller than in the standard system, i.e., the impeller was much closer to the vessel bottom.

On the other hand, the radial velocities in the inner core at $Y = 7$ mm were inwards directed and extremely weak, and they increased proportionally to the agitation speed. The corresponding velocities in the standard system for $r < 0.01$m were also weak but always higher than those in the mini vessel system.

4.5.3 Strain Rate

The strain rate is the rate of change in deformation of the material with respect to time. In this study, the most relevant strain rate was at the tablet surface. The expression for strain rate magnitude value can be defined as following [102]:

$$\dot{\gamma} = |S| = \sqrt{\frac{1}{2}\sum_{i}\sum_{j} S_{ij}^{2}} \tag{4.8}$$

Where S_{ij} is the components of rate-of-deformation tensor, which, for an incompressible Newtonian fluid, can be expressed as:

$$S_{ij} = \frac{\partial u_i}{\partial x_j} + \frac{\partial u_j}{\partial x_i} \tag{4.9}$$

Then, the strain rate tensor, τ, can be related to the rate-of-deformation tensor, **S**, by the equation:

$$\tau = -\mu \boldsymbol{S} \tag{4.10}$$

As per the definition, the magnitude of the strain rate at any point of interest provides important information on how rapidly the velocity changes with distance, and this is especially relevant on the tablet surface, since the higher the shear rate, the higher the tablet-medium mass transfer process can be expected to be. Obviously, the strain rate can be another important variable to be considered to estimate the tablet-fluid mass transfer rate.

Figure 4.18 shows the distribution of strain rates in the mini vessels at different agitation speeds compared to those in the USP Apparatus 2 in the *absence* of a tablet. Figure 4.19 shows a magnified version of the same figure only for the region below the impeller.

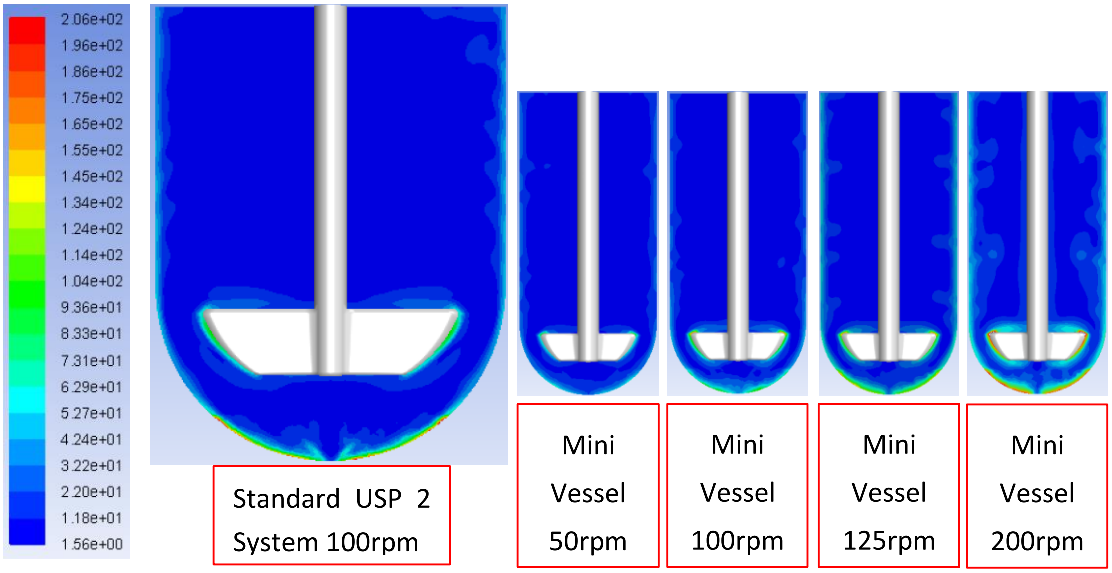

Figure 4.18 CFD predictions of strain rates on a vertical cross section through the impeller shaft for the entire region of standard USP 2 system and the mini vessel at different agitation speeds (50rpm, 100rpm, 125rpm, and 200rpm). Red color represents strain rates equal to, or higher than, 206 s^{-1}.

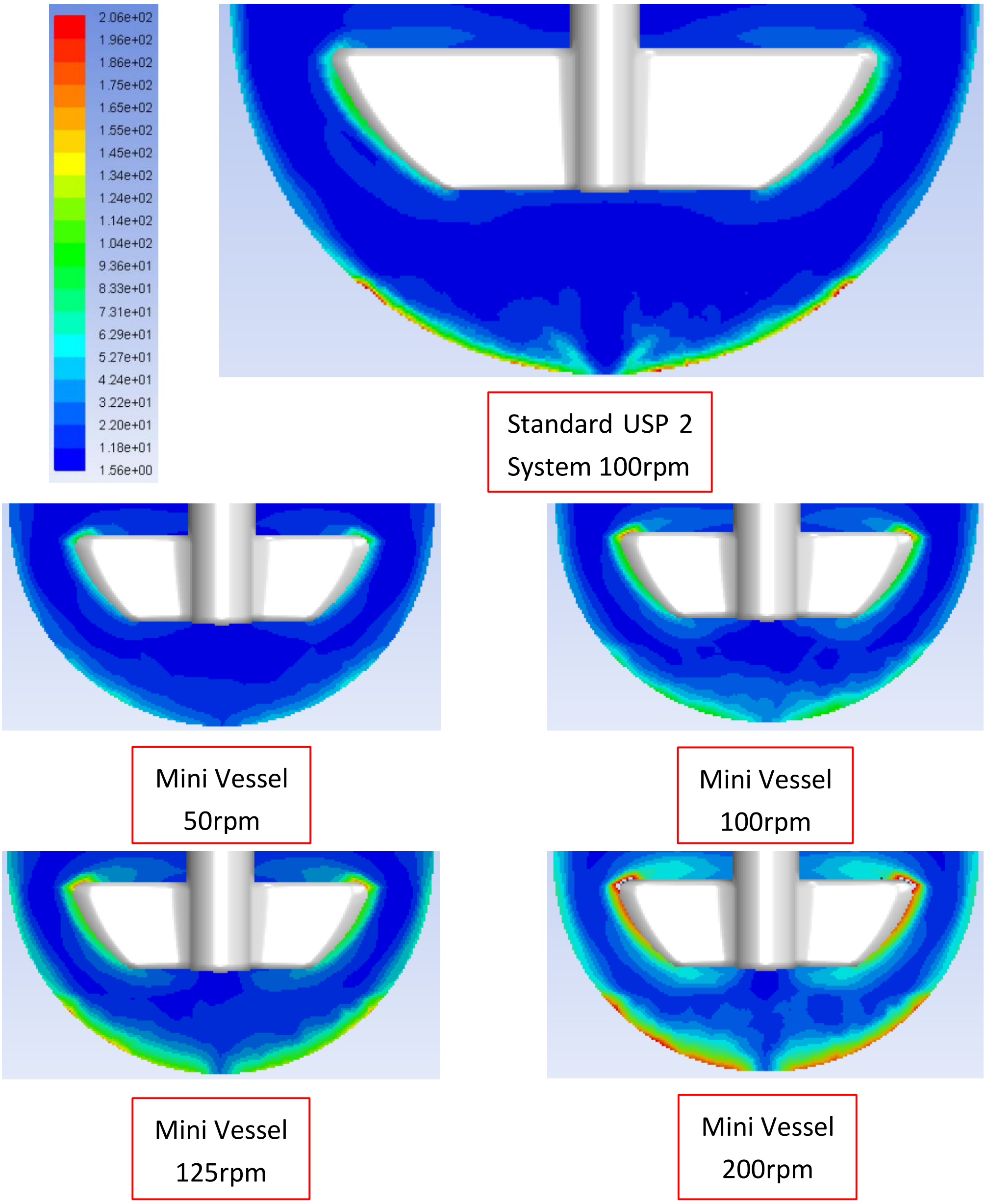

Standard USP 2 System 100rpm

Mini Vessel 50rpm

Mini Vessel 100rpm

Mini Vessel 125rpm

Mini Vessel 200rpm

Figure 4.19 CFD predictions of strain rates on a vertical cross section through the impeller shaft for the bottom region of vessel with a magnified version in USP 2 system and mini vessel system at different agitation speeds (50 rpm, 100rpm, 125rpm, and 200rpm). Red color represents strain rates equal to, or higher than, 206 s^{-1}.

From the CFD simulation, the strain rate distribution on the surfaces of tablets (top surface and side surface) could be obtained for the mini vessel system. For each agitation speed, the strain rate distribution on the impeller cross section of the entire vessel and expanded contour maps for the bottom region for the case in which the *tablet is present* are shown in Figure 4.20 and Figure 4.21. Moreover, the average strain rate on the tablet surface was obtained and it is reported in Table 4.3.

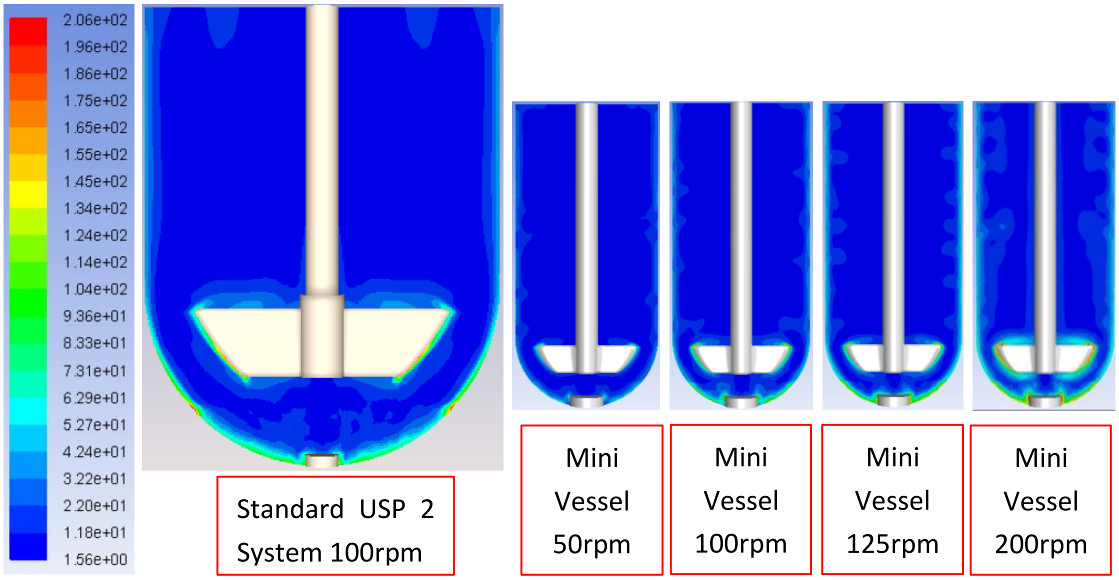

Figure 4.20 CFD predictions of strain rates on a vertical cross section through the impeller shaft for the entire region of vessel with tablet centered located in USP 2 system and mini vessel system at different agitation speeds (50 rpm, 100rpm, 125rpm, and 200rpm). Red color represents strain rates equal to, or higher than, 206 s^{-1}.

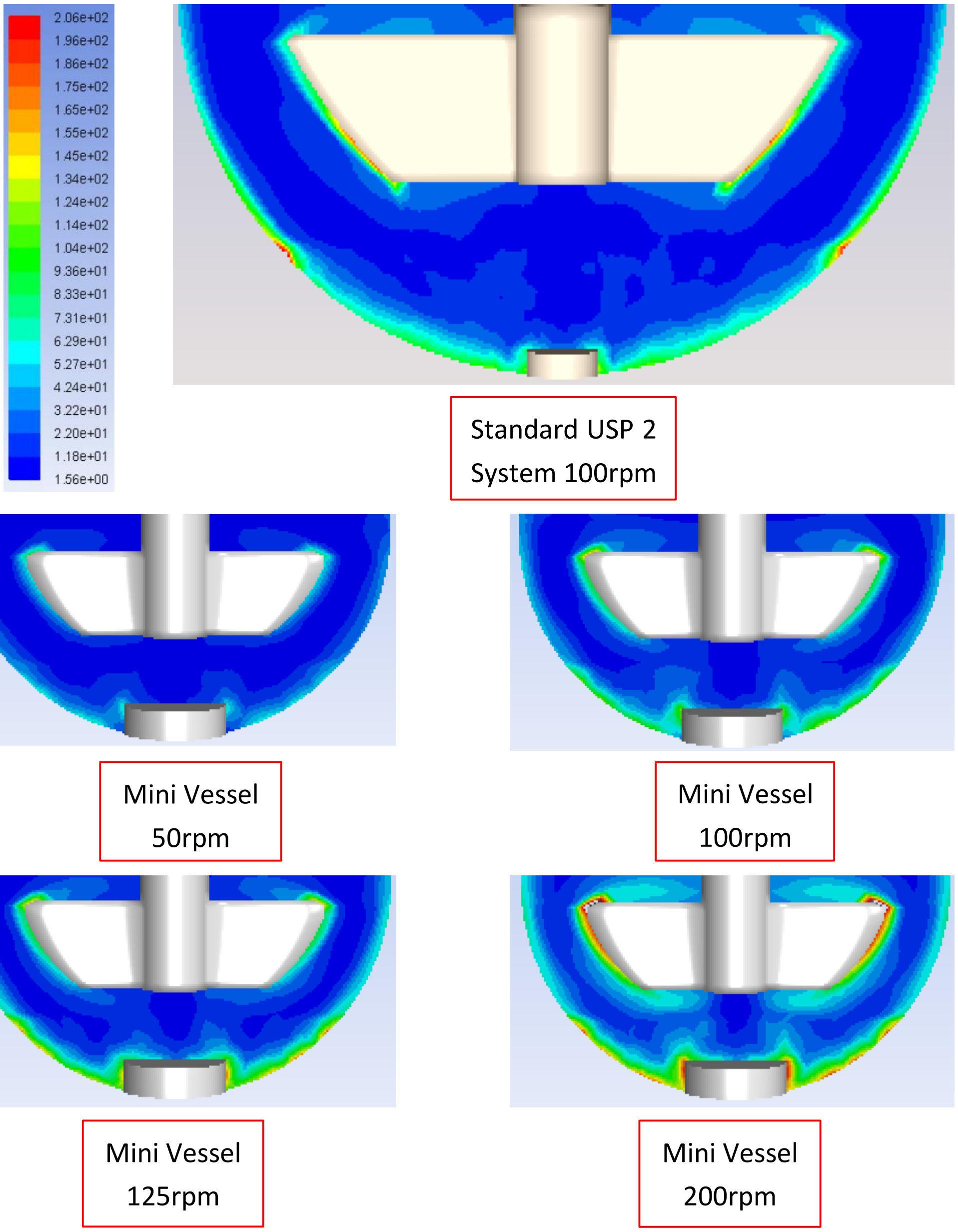

Figure 4.21 CFD predictions of strain rates on a vertical cross section through the impeller shaft with a magnified version for the bottom region of vessel with tablet centered located in USP 2 system and mini vessel system at different agitation speeds (50 rpm, 100rpm, 125rpm, and 200rpm). Red color represents strain rates equal to, or higher than, 206 s^{-1}.

The strain rate for each different operating condition (different agitation speed) could be analyzed and compared with the standard USP 2 system data to compare the strain rates and mass transfer process for the two systems.

Figure 4.20 and Figure 4.21 show that the strain rate value was large around the impeller blades and the vessel bottom compared to other regions of the vessel, because the velocity had large gradients in these areas. By increasing the agitation speed from 50rpm to 200rpm, the strain rate layer become thicker and had a higher value. For example, the strain rate layer at 100rpm was much larger and more extensive (light green color) than that at 50rpm (blue color). However, strain rate at the 125rpm was much closes to the 100rpm case, and very different from that at 200rpm. The strain rate clearly depended on the agitation speed.

By comparing the strain rate contour maps for different agitation speeds, one can see that the tablet surface strain rate increased as the agitation speed increased, which was significant for this study because it could be directly representing the mass transfer process and dissolution rate. Therefore, the average strain rate on the tablet surfaces was also calculated and compared with that in the standard system. The strain rates in the mini vessel were, respectively, 54.57% smaller (at 50rpm) and 10.76% smaller (at 100rpm) than the strain rate in the standard USP 2 system at 100 rpm, while, 9.63% higher (at 125rpm) and 77.11% higher (200rpm) in the mini vessel than that in standard USP 2 system at 100 rpm (Table 4.3).

Table 4.3 CFD predicted average strain rate on the tablet surface in USP 2 system and mini vessel system at different agitation speeds.

Systems with Different Operating Conditions	CFD-Predicted Average Strain Rate on Tablet Surface (s^{-1})	Strain Rate difference between two systems
Mini Vessel-100mL 50rpm	36.36	-54.57%
Mini Vessel-100mL 100rpm	71.42	-10.76%
Mini Vessel-100mL 125rpm	87.75	+9.63%
Mini Vessel-100mL 200rpm	141.76	+77.11%
Standard USP2 Vessel-900mL 100rpm	80.04	0

The strain rates at 50rpm and 200rpm in the mini vessel system were very different from those in the standard system. However, the strain rates at 100rpm and 125rpm were very close to the standard system, especially for the 125rpm case. This implies that the tablet-medium mass transfer coefficient could change appreciably in the mini vessels depending on the agitation speed, but that the strain rate and the mass transfer coefficient in the mini vessel and the USP Apparatus 2 could be made to match at the appropriate agitation speed in the mini vessels.

4.5.4 Mass Transfer Coefficient

In order to provide a full comparison between the mini vessel system and standard USP 2 system, the mass transfer coefficient was predicted by using the mass transfer model reported above. In this mass transfer model, fluid velocities were used as an input which was predicted from the CFD simulation results. In the USP 2 vessel, the tablet is not rotating but the fluid around the tablet had strong tangential flow. Therefore, in this mass transfer model the velocity of the fluid layer which was just next to the top and side of tablet was considered and used here (about 1 mm near the tablet surface). At the surface of the tablet, the velocity was equal to zero since the tablet is not considered to move in this work. The velocity vectors are shown in Figure 4.22, showing that a center-positioned tablet experiences a rotating fluid flow above its top surface and side surface, and indicates that it was appropriate to use the rotating disk model above the top surface for the mass transfer coefficient on this surface and the rotating cylinder model for the mass transfer coefficient on the tablet side.

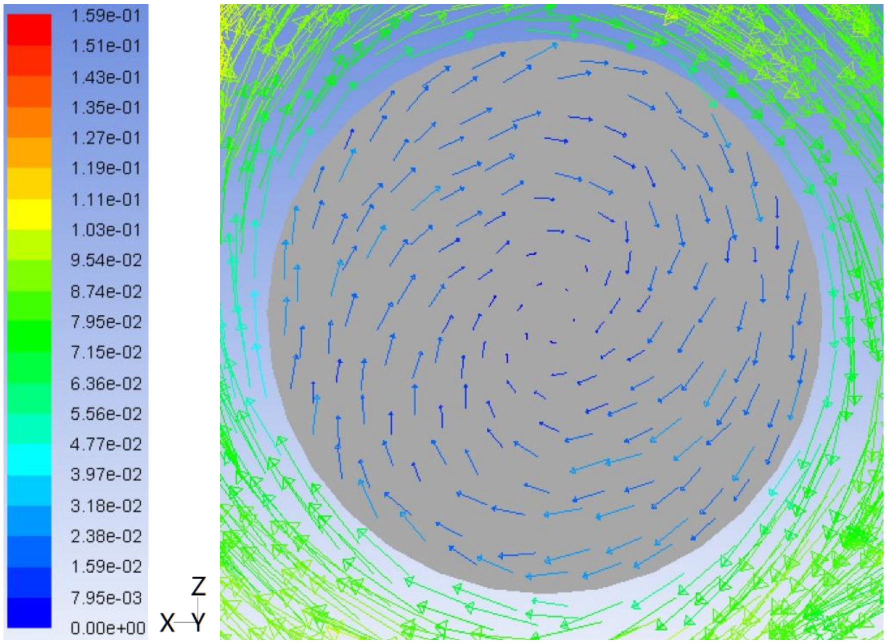

Figure 4.22 CFD-predicted velocity vectors (m/s) above the top surface for 1mm of the centrally located salicylic acid tablet in the mini vessel at 125rpm.

The mass transfer coefficient was calculated for each agitation speed in the mini vessel system as well as for the standard system. The results are shown in Table 4.4. The area-averaged mass transfer coefficient was also calculated using Equation 4.7 and the results are presented in the last column of Table 4.4.

Table 4.4 Predicted Mass Transfer Coefficient for Salicylic Acid Tablet Center Located in Mini Vessel at Different Agitation Speeds Compared with USP 2 Standard System.

Systems with Different Operating Conditions	Predicted Mass Transfer Coefficient at Top Surface of Tablet, k_{top} (m/s)	Predicted Mass Transfer Coefficient at Side Surface of Tablet, k_{side} (m/s)	Predicted Area-Averaged Mass Transfer Coefficient for Tablet, k_{prd} (m/s)
Mini Vessel-100mL 50rpm	1.77E-05	5.56E-06	7.99E-06
Mini Vessel-100mL 100rpm	2.76E-05	1.01E-05	1.36E-05
Mini Vessel-100mL 125rpm	3.23E-05	1.24E-05	1.64E-05
Mini Vessel-100mL 200rpm	4.95E-05	1.19E-05	2.74E-05
Standard USP2 Vessel-900mL 100rpm	3.06E-05	1.31E-05	1.66E-05

As mentioned before, the strain rate could be related to the mass transfer coefficient, according to the boundary layer theory [101]. Since the strain rate was defined as the rate of velocity changes with distance when moving away from the point of interest, and the fluid velocity gradient in the boundary layer surrounding the solid tablet could directly affect the mass transfer coefficient. Therefore, a high strain rate indicates that high velocity change rate, which can directly increase the tablet-medium mass transfer process. The strain rates for different agitation speed in mini vessel were plotted against the area-averaged mass transfer coefficients values, which were shown in Figure 4.19. The data were regressed and a straight line with R=0.99 was obtained. This regression line indicates that there is a direct proportionality between the mass transfer coefficient and the strain rate for the center-positioned tablet in the mini vessel.

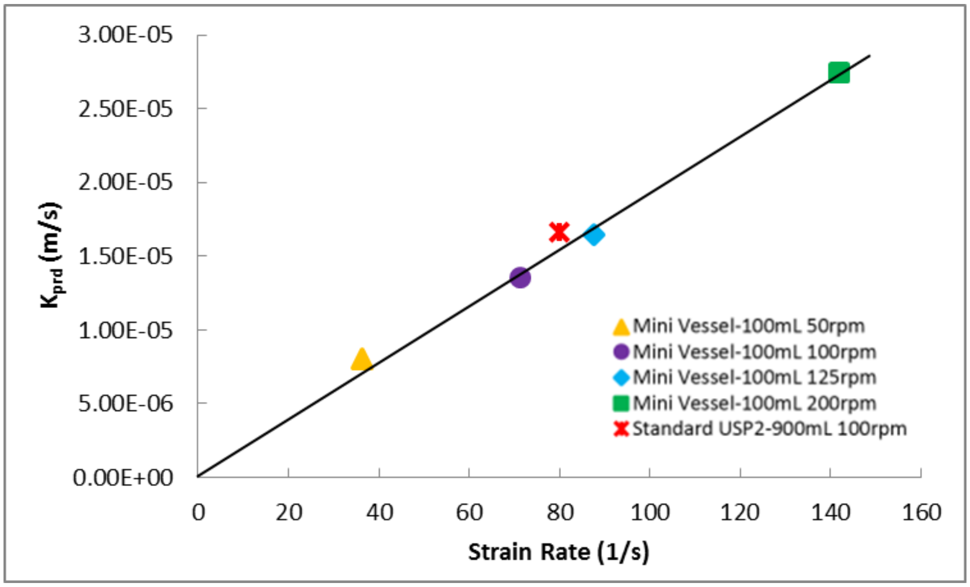

Figure 4.23 Correlation between the CFD-predicted overall mass transfer coefficient for salicylic acid tablets and the CFD-predicted average strain rate values on the surfaces of tablets.

A comparison of the strain rate and mass transfer coefficients for mini vessels with those in the USP Apparatus 2 also showed that a similar relation existed between these two parameters in the mini vessel system as in the standard system, similarly to presented in previous work for the USP 2 system [7], indicating that these two systems have similar hydrodynamics. Furthermore, the predicted mass transfer coefficient data in mini vessel was compared with the standard system for different agitation speeds in order to obtain the operating condition at which the mass transfer coefficient was closer to the case in standard system. The data in Table 4.4 show that under different operating condition for the case of a centered salicylic acid tablet immersed in a mini vessel at 50rpm, 100rpm, 125rpm, and 200rpm, the overall mass transfer coefficient was 7.99×10^{-6} m/s, 1.36×10^{-5} m/s, 1.64×10^{-5} m/s, and 2.74×10^{-5} m/s, respectively; while that in the standard USP 2 system at 100 rpm was 1.66×10^{-5} m/s. By comparing these data, one can see that the mini vessel mass transfer coefficients at 50rpm, 100rpm and 125rpm were 51.86%, 18.07% and 1.20% smaller than the that of standard system, representatively. The mass transfer coefficients at 200rpm was 65.06% larger than the value in standard system. The mass transfer coefficient results for the mini vessel and the standard system were quantitatively compared and plotted in Table 4.4 and Figure 4.23. This plot clearly indicates that at 125rpm, the mass transfer coefficient in the mini vessel was very close to that in standard system at 100 rpm. Among the other three agitation speeds, mass transfer coefficient of 100rpm was also close to the standard system, but for 50rpm and 200rpm, the mass transfer coefficients were appreciably different from that for the standard system. The same conclusion can be shown to apply to in the strain rate results.

4.5.5 Discussion

The experimental results for the hydrodynamics study in mini vessel at different agitation speeds agreed well with the results of the CFD simulations. The velocity vector maps showed that the flow pattern on a cross section in both systems was substantially similar, although the velocity magnitude in mini vessels was typically lower.

The radial velocities and axial velocities were plotted on several iso-surfaces for different agitation speeds in the mini vessel system and compared with those in standard system. The CFD and PIV results for mini vessel systems generally matched well. On the iso-surface around the impeller, the velocity from both methods were very different at different agitation speeds. However, in the bottom region, different agitation speeds did not result in very different velocity profiles, especially in the core region below the impeller where the flow next to the wall could not penetrate the core region. This also posed a challenge for the PIV measurements since the velocity intensity was extremely low in this region.

The velocity below the impeller can be expected to affect strongly the tablet dissolution rate. In this zone, and especially near the vessel bottom, the region for r<5mm was the most important zone because the tablet is typically located here. The mini vessel system and standard system both generated velocities that were comparable to each other in this region, which implies that the tablet could experience similar mass transfer rates. However, different agitation speeds resulted in slightly different velocity value, although for the cases of 100rpm and 125rpm, the axial velocities were close to the standard system, while the radial velocity in all cases was very small in mini vessel and close to zero.

As the agitation speed increased, the tangential flow velocity increased significantly and this could enhance the strain rate around the impeller and in the outer region near the bottom. Additionally, the inner core region shrank as the agitation speed increased and this could also contribute to increase the mass transfer coefficient for the tablet and the corresponding dissolution rate.

The strain rate in the 200rpm case was less homogeneous in the bottom than that of 50rpm in mini vessel, which was similar to what observed in the standard system of previous work [6]. In this situation, the tablet at the center of the vessel bottom could experience different strain rate because this rate was more uneven at higher agitation speeds.

The strain rate and mass transfer coefficient were highly correlated. The strain rate and mass transfer coefficient in the mini vessel at 100 rpm and 125rpm were closest to those in the standard system at 100 rpm. This result could provide basic guidance on how to choose the agitation speed for the tablet dissolution in the mini vessel system, since no official recommendations for this system currently exist.

4.6 Conclusion

The mini vessel system design originated from the USP Apparatus 2. However, before the mini vessel can become widely used in industry, the hydrodynamics must be understood system since no information is available from the USP. Here, the flow pattern in mini vessels was obtained by both CFD simulations and PIV velocity measurements for four different agitation speeds in the mini vessel, and it was shown to result in flow patterns qualitatively similar to those in the standard USP 2 system. The velocity profiles were also compared on several iso-surfaces for the mini vessel system and the standard system, showing difference between two systems.

In the most important zone, i.e., the inner core zone at the vessel bottom, the velocities were similar on the lowest iso-surface, especially for the axial velocity at 100rpm and 125rpm in the mini vessel compared with 100rpm in the 900mL USP 2 system. This was not clearly the case for iso-surfaces above the bottom zone.

In order to further study the parameters which have a direct effect on the dissolution rate, the strain rates were obtained from the CFD simulations for different agitation speeds in the mini vessel and compared with those in the standard system. Additionally, the mass transfer coefficient between a virtual tablet place at the vessel bottom and the surrounding fluid was calculated based on a rotating disk and rotating cylinder models and compared with mass transfer similarly obtained previously in the USP 2 system. In general, the values of the strain rate at the wall in mini vessels increased as the agitation speed increased. At 125rpm and 100rpm the strain rates on the surface of the virtual tablet in in the mini vessel, were similar to the corresponding strain rate values at 100rpm in the 900mL USP 2 system.

The mass transfer coefficient at the tablet was additionally calculated from the tablet-medium mass transfer models by using the velocity values obtained from the CFD simulation. The predicted mass transfer coefficients were shown to depend on the agitation speeds in mini vessel which were also compared that in USP 2 system under 100rpm. The results clearly showed that the mass transfer coefficient was highly correlated with the strain rate, and that at 100rpm and 125rpm, the mass transfer coefficients in the in mini vessels were similar to those in the standard system at 100 rpm.

In summary, the general flow pattern in the mini vessel is similar to that in the standard USP 2 system. The magnitude of the velocity distribution on the critical iso-surface near the vessel bottom is similar in both systems, but obviously weaker above the impeller in the mini vessel system than the in standard system.

The poorly mixed central inner core zone below the impeller persisted even under 200rpm in mini vessel, although this zone shrank as the agitation speed increased. The predicted strain rate and mass transfer coefficients from a virtual tablet to the fluid also increased as the agitation increased. It was found that at 125rpm the strain rate and mass transfer coefficient in the in mini vessel were very close to those in the standard USP 2 system at 100rpm.

To the best of our knowledge, this first study focused on the basic hydrodynamics of mini vessel systems. The result of this work can provide guidance to their application in industry and help in comparing dissolution testing data obtained in different dissolution testing apparatuses.

CHAPTER 5

CHARACTERIZATION OF MIXING IN THE EPA BAFFLED FLASK FOR DISPERSION EFFECTIVENESS TESTING

5.1 Background and Objective

Oil spills, due to their potential large sizes, are one of the worst environmental disasters causing both short term and long term adverse effects on the environment and wild life. Once a spill event occur, various countermeasures are considered including the use of chemical dispersants to cause the oil to spread in the water column (labelled oil dispersion), which would prevent the slick from reaching the shorelines where it could cause the most damage [65, 66, 67]. Oil dispersant is a mixture of surfactants and solvents to help oil slick break into small droplets in a process known as dispersion [5, 68, 69]. The term "dispersion" used here is from the oil literature and is different from the spreading of chemicals due to the spatial variation of velocity. The mixing energy imposed by waves, especially breaking waves will enhance the dispersion process [70].

Field and laboratory experiments have been conducted to study the dispersant effectiveness (DE) under different turbulence intensity of the sea state. Because of the complex environment in the sea, field studies often introduce experimental uncertainties in the measurements and are also very difficult and expensive to implement. Alternatively, the standard laboratory flask test has been widely used in oil spill research to study dispersant effectiveness on oil [65, 71]. To better understand the representative of these flask tests to various sea states, it is necessary to fully understand the flow dynamics and turbulence structures in the flask tests.

Prior investigations on this issue were conducted by Kaku et al. [5, 68]. They used Hot Wire Anemometer (HWA) to characterize mixing dynamics in the swirling flask (SF) and the baffled flask (BF). They concluded that the turbulence in the baffled flask closely resembles the turbulence occurring in the top few centimeters of a breaking wave, hence, the baffled flask is more representative of mixing at sea due to breaking waves than the swirling flask [5, 68]. Based on their studies, the baffled flask test was proposed to be adopted as the official standard protocol replacing the Swirling Flask Test by U.S. Environmental Protection Agency (EPA) [72]. Generally, the instrument they used for the measurement of the velocity, HWA (adopts single-point velocity measurement technique), can only measure time series of point velocities and cannot provide a whole field (or a cross section) spatial velocity variations in the flasks. This method gives the temporal spectrum and needs to rely on Taylor’s frozen turbulence hypothesis [73] to convert temporal series into spatial data. The hypothesis states that turbulence is advected with space without change. This hypothesis is achievable in unidirectional flows where the turbulence velocity is less than 10% to 20% of the advection velocity. In a rotating fluid, there might be difficulty in using the hypothesis; also, this method could also limit the estimation approaches of energy dissipation. For this reason, we are using herein the PIV to measure turbulence structures in the BF.

The particle image velocimetry (PIV) has been widely used for the measurement of spatial phenomena in flows, which uses an optical imaging technique to obtain simultaneous measurement of two components of the velocity at many points (normally over thousands of points) in a flow field. For example, Liu et al. [74] used a high resolution PIV to measure the turbulent velocity field for fully developed flow in an enclosed channel and the statistical properties of the velocity were in good agreement with laser-Doppler velocimetry (LDV) measurements and with direct numerical simulations. Hyun et al. [75] evaluated the performance of PIV in the open-channel flow and concluded that PIV is fast reaching a stage where it can be applied with a level of confidence similar to LDV. Cheng et al. [76] was the first to use PIV technique to study flow related to water treatment processes in a stirred tank. Since then, studies of mixing energy in stirred tank or reactors using PIV data have been well tested and evaluated [77, 78, 79, 80].

In this study, the particle-image velocimetry (PIV) was used for the measurements of velocity fields (velocities at thousands of points within a chosen cross section) in the baffled flask used for dispersant effectiveness testing. Most of the stirred vessels investigated in previous studies are a cylindrical or square tank (has an amount of over 1 L liquids) with an impeller inside. This is the first time to use PIV techniques to evaluate the flow dynamics and turbulent structures in a laboratory flask with a volume of 200 mL. Seven rotation speeds were measured during the experiments, which were Ω=100, 125, 150, 160, 170, 200, and 250 rpm. The measured spatial velocity data were then used to evaluate the overall energy structures in the baffled flask.

5.2 Evaluation of Energy Dissipation

The baffled flask has four baffles in it, resulting in an irregular geometry in the flask. Such geometry forms an over-and-under motion of water flow which could represent more characteristic of the type of mixing that occurs from breaking waves at sea [5, 68, 81]. To study the turbulent structure in the flask, there are several characteristic parameters of interest in the turbulent mixing process. The energy dissipation rate, ε, can be used as an appropriate scaling parameter to characterize the intensity of the mixing energy [82]. The integral length based on the velocity field characterizes the size of eddies containing most of the turbulence mixing energy [83]. The Kolmogorov microscale provides an estimate for the smallest eddy that can exist in the turbulent flow.

For calculation of these characteristic parameters from PIV data, a turbulent velocity field must first be obtained. Considering a 2D velocity field obtained from PIV, the velocity at each location can be expressed as:

$$u_i(x,y) = \overline{U}(x,y) + u_i^{'}(x,y) \qquad \text{i = 1, 2, 3…N} \tag{5.1}$$

Where the index ‘i’ represents different realizations (replicates from PIV measurements); $\overline{U}$ is the average of N realizations at each location (m/s); u_i' is the turbulent component of velocity (m/s); x, y are the coordinates of each point in the measured cross section (m).

The internal dynamics of turbulence transfer energy from large scale to small scale. This energy transfer proceeds at a rate dictated by the energy of the large eddies (of order u^2) and their time scale (of order l/u), where l is characteristic length scale and u is velocity [83]. Thus, the evaluation of energy dissipation rate ε could be estimated using the dimensional argument analysis [76, 83, 84], which is based on the relationship between dissipation rate and integral length scale. The energy dissipation rate can be written as:

$$\varepsilon_j = A\frac{(u'_{rmsj})^3}{\tau_l} \tag{5.2}$$

Where u_{rmsj}’ is the root mean square of turbulent component of velocity at each measuring location j (m/s); A is constant of order unity; τ_l is the integral length scale of turbulence (m) which can be estimated [83] as:

$$\tau_l = \int_0^{\infty} R_l \, dl \tag{5.3}$$

Where R_l is the spatial autocorrelation function as a function of distance class l. The isotropic turbulence is assumed in this study; therefore, only 1D autocorrelation function is obtained as:

$$R_l = \frac{\overline{u_i^{'}(x,y)u_i^{'}(x+\tau,y)}}{\overline{(u_i^{'})^2}} \text{ or } R_l = \frac{\overline{u_i^{'}(x,y)u_i^{'}(x,y+\tau)}}{\overline{(u_i^{'})^2}} \tag{5.4}$$

Where τ is the distance lag. In the calculation of Eq. 5.3, the point of first zero crossing is used to replace the upper limit of the integration. The Kolmogorov microscale is estimated based on dimensional arguments [83] as:

$$\eta = \left(\frac{\nu^3}{\varepsilon}\right)^{1/4} \tag{5.5}$$

The velocity gradient is estimated as:

$$G = \left(\frac{\varepsilon}{\nu}\right)^{1/2} \tag{5.6}$$

5.3 Experiment Setup

A particle image velocimetry (PIV) system was employed to measure the velocity field in the baffled flask at different rotation speeds. A 200 mL baffled trypsinizing flask was used during the experiments. The flask contained 120 mL of tap water and was mounted in the center of a transparent cubic container which was filled with tap water to eliminate optical distortion. The cubic container with the flask inside was then mounted on the center of an orbital shaker (MAXQ 2000, Thermo Scientific Inc.). The shaking speed can be varied from approximately 40-400 rpm. An orbital diameter, d_0=20 mm was traced by the shaker. Seven rotation speeds were tested during the experiments: 100, 125, 150, 160, 170, 200, 250 rpm. All the experiments were conducted under room temperature (about 20 ℃).

The Dantec PIV system was employed consisting of a Dantec Dynamics HiSense PIV/PLIF CCD camera (Model No. C4742-53-12NRB, Dantec Dynamics A/S). A double pulsed 120 mJ Nd: YAG laser (New Wave Research model Solo 120 15 Hz, Fremont CA, USA) was used to produce a 5 mm thick light sheet, which illuminated a thin vertical sheet passing through the center of the baffled flask. Silver-coated hollow borosilicate glass spherical particles with a density of 1.4 g/cm^3 and median diameter of 10 μm were seeded in the flask to identify the velocity field at each cycle. The seeding density is maintained as 15-25 particles/interrogation cell [80] during all the experiments. The schematic of the PIV system is shown in Figure 5.1. Measurements were taken when the container (with the baffled flask in the center) reached its position furthest to the left side as shown in Figure 5.1 (A). The axial and radial velocity components were measured.

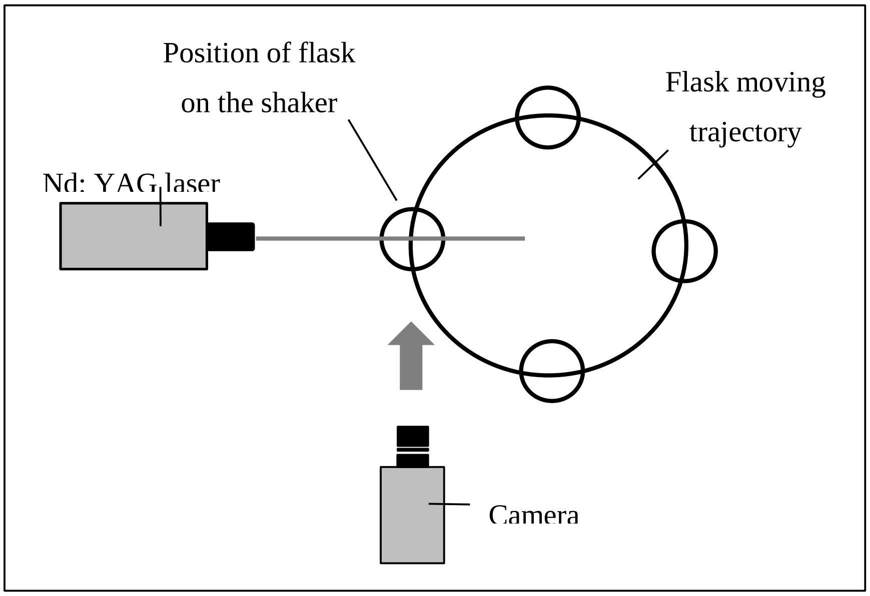

(A)

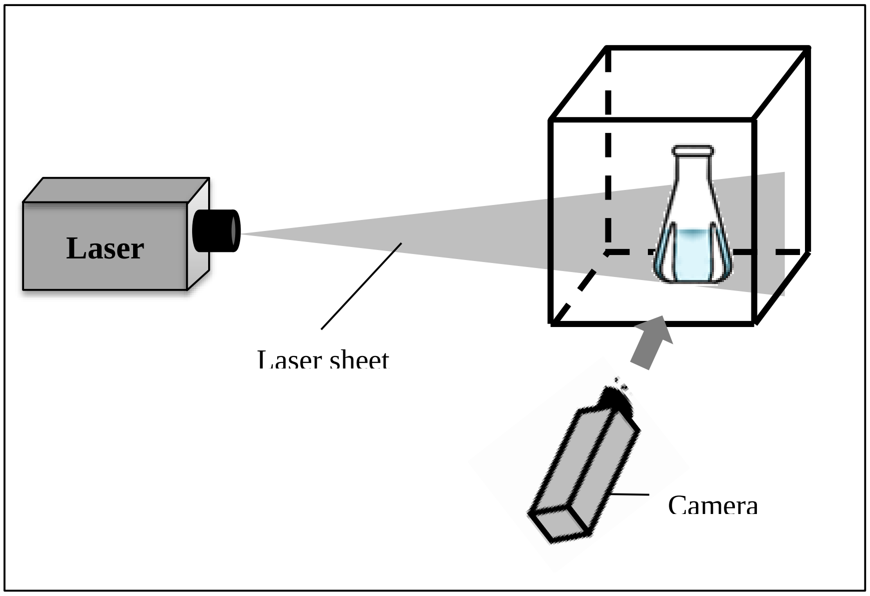

(B)

Figure 5.1 Schematic of PIV experimental setup to measure the water velocity in the Baffled Flask (BF): (A) position of the flask on the shaker; and (B) illustration how the PIV is used to measure the water velocity in vertical planes within the BF.

The camera we used provided a resolution of 1264 × 1008 pixels per frame, with a compact Nikon lens of AF Micro-Nikkor 60 mm f/2.8D for extreme close-up/macro shooting. Although the camera could be positioned at different distances from the flask, in order to have the best spatial resolution within the capacity of the camera and lenses, data reported herein were obtained with the camera approximately 25 cm (the minimum distance that the lens required) from the plane of the laser sheet. This provided a viewing area of 37.5 mm × 29.9 mm. The images were processed using the Dantec's FlowManager software provided by Dantec Dynamics A/S. Adaptive cross-correlation technique was employed. To maintain high measurement accuracy, a compromise between spatial resolution and velocity dynamic range had to be made. Based on the suggestions from Dantec Dynamics A/S (2002) [85], to maximize the number of vectors in the PIV vector map, a 32 pixel × 32 pixel interrogation areas (about 0.95 mm width) with a 75% overlap were chosen in this study, which gave 0.24 mm step size. Though the overlapping of the interrogation areas does not mean an increase in the fundamental spatial resolution, it may provide some inherent correlation among the adjacent vectors [76]. A total of 19625 (157 × 125 in the x, z plane) vectors were generated within each frame.

The time between pulses is a critical data acquisition parameter which is generally selected to suit the velocity of the flow field and the size of the interrogation area so there is no loss-of-pairs [85]. For a given measurement scenario, the higher the velocity the shorter the time between pulses. The recommended maximum displacement is ±1/4 of the length of the side of the interrogation cell [85]. For our experiments, the time between pulses were chosen from 100 μs – 900 μs for the seven rotation speeds (250 rpm – 100 rpm) evaluated to obtain suitable particle displacement for each flow field.

Two vertical planes were measured for each rotation speed. Figure 5.2 shows the positions and dimensions of the large cross section (A_{large}) and the small cross section (A_{small}). Images in Figure 5.2 (B) and 5.2 (C) were captured from the experiment of Ω = 100 rpm, where the large cross section has the dimension of roughly 76 mm × 44 mm, and the small cross section of about 57 mm × 43 mm. Both cross sections are larger than the viewing area (37.5 mm × 29.9 mm) from the camera. To obtain a full picture of the velocity field in the flask, the A_{large} was divided into 6 viewing areas (Figure 5.2 (B)), and A_{small} was divided into 4 viewing areas (Figure 5.2 (C)). Each viewing area was measured independently. This gives a total 10 individual experiments for each rotation speed. For each viewing area, 200 PIV realizations were obtained, which means 200 instantaneous velocity fields were generated for each viewing area at each rotation speed. Data of these small viewing areas were integrated together to present the whole flow fields in the flask. All the analysis presented below used the integrated data.

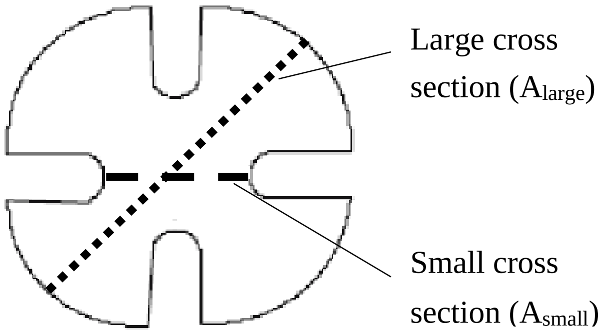

(A) Plan View

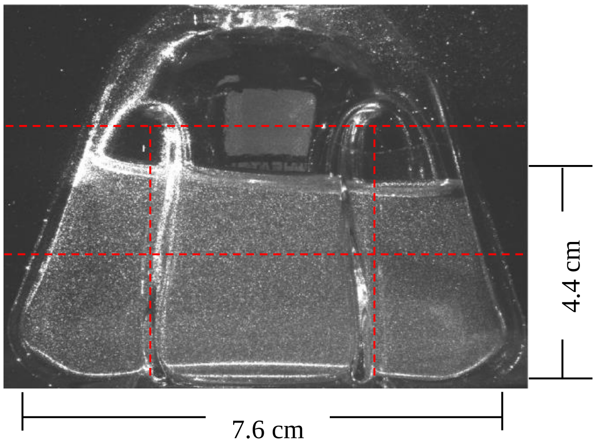

(B) Dimension of A_{large}

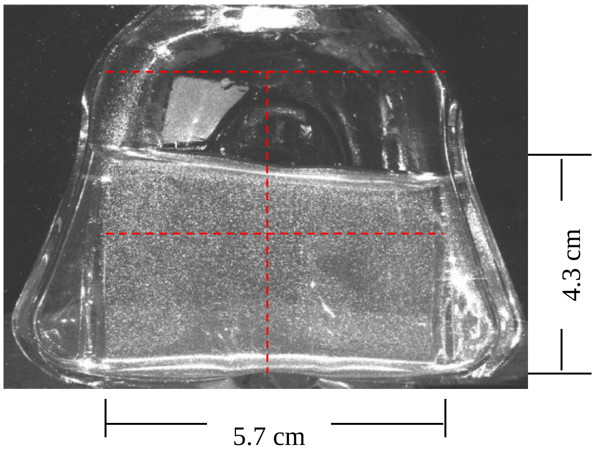

(C) Dimension of A_{small}

Figure 5.2 Specifications of the large cross section and the small cross section of the velocity field: A) plane view; B) and C) are the vertical views of the large and small cross section, respectively.

5.4 Results

5.4.1 Velocity Fields in Baffled Flask

The average flow fields in the baffled flask are plotted in Figure 5.3 for all seven rotation speeds (Ω = 100, 125, 150, 160, 170, 200, 250 rpm). As stated in Section 5.3, the large and small cross sections are divided into small viewing areas, as shown in Figure 5.2, there are six areas for A_{large}, and four areas for A_{small}. The integrated data of these small viewing areas were used for results analysis. Though velocity fields of these viewing areas were measured independently, only small data discrepancies were observed in the boundaries between viewing areas during the integration as shown in Figure 5.3. Integrated velocity fields can generally present the whole-field velocity fields in the flask.

The vector map obtained from PIV is a square field with 157 × 125 points in the x, z plane for each small viewing area. However, the map of each viewing area contains vectors outside the domain of interest (fluid inside the flask) (Figure 5.2 (B) and Figure 5.2 (C)). These vectors (vectors above the water surface and beyond the flask boundaries) were found and masked based on the images captured from the experiments for each rotation speed. To avoid any possible measurement affects by the water surface, especially for high rotation speed that the splash of water could affect the PIV recordings (movement of the seeding particles within the splash regions may not follow or represent the real motion of water flow and also the splash of water may trap air bubbles in the water), the vector mask of water surface was taken a few millimeters below the real surface. The same methods were also employed for the three wall boundaries, and vectors (inside the flask) about 1 mm away from the wall was removed to mask the wall boundaries. Only vectors inside the mask covering the fluid in the flask were used for result analysis.

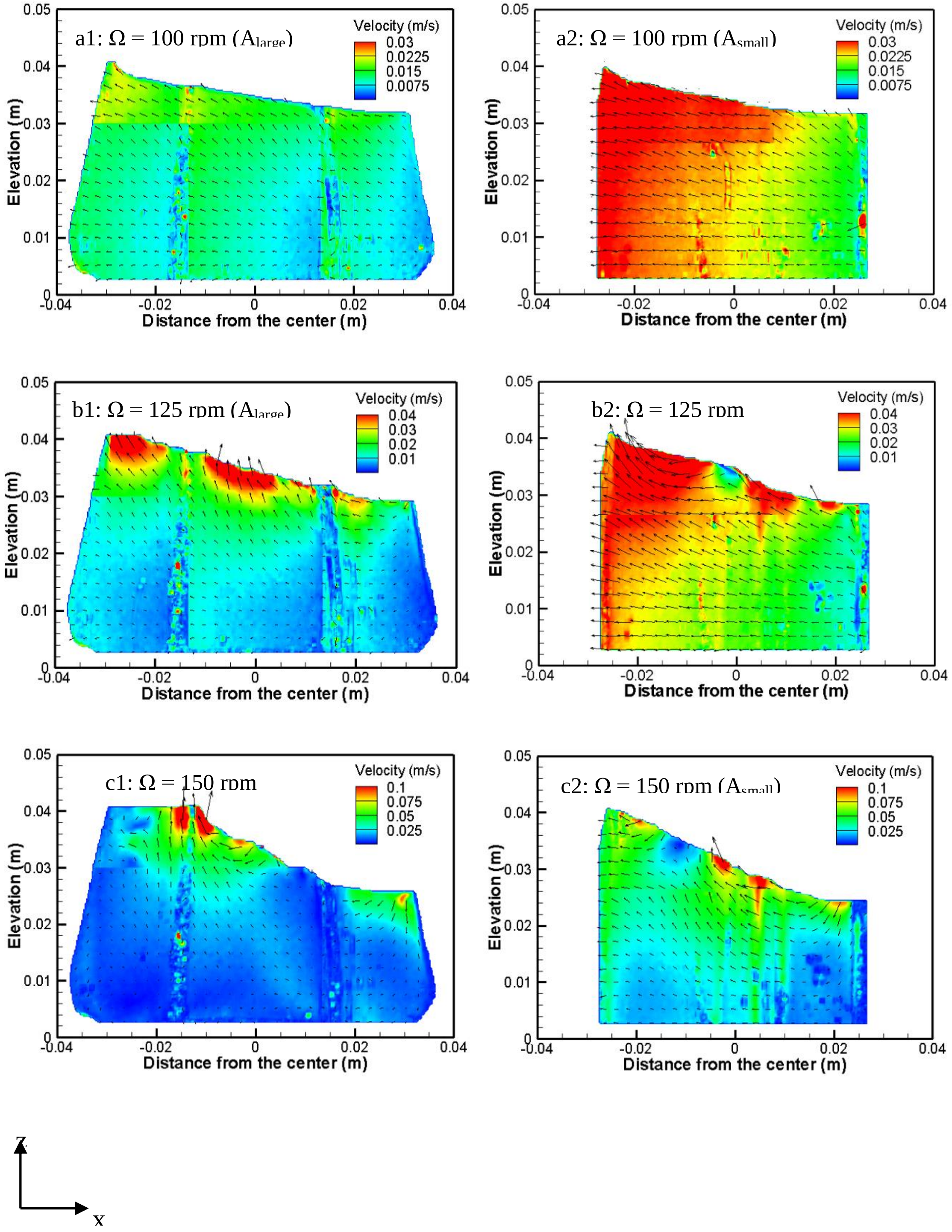

Figure 5.3 Average velocity fields in the baffled flask for both large cross section (left panel) and small cross section (right panel) at seven rotation speeds of the orbital shaker: 100, 125, 150, 160, 170, 200, and 250 rpm. The water surface was found and masked for each rotation speed based on the images captured during the experiments (continued).

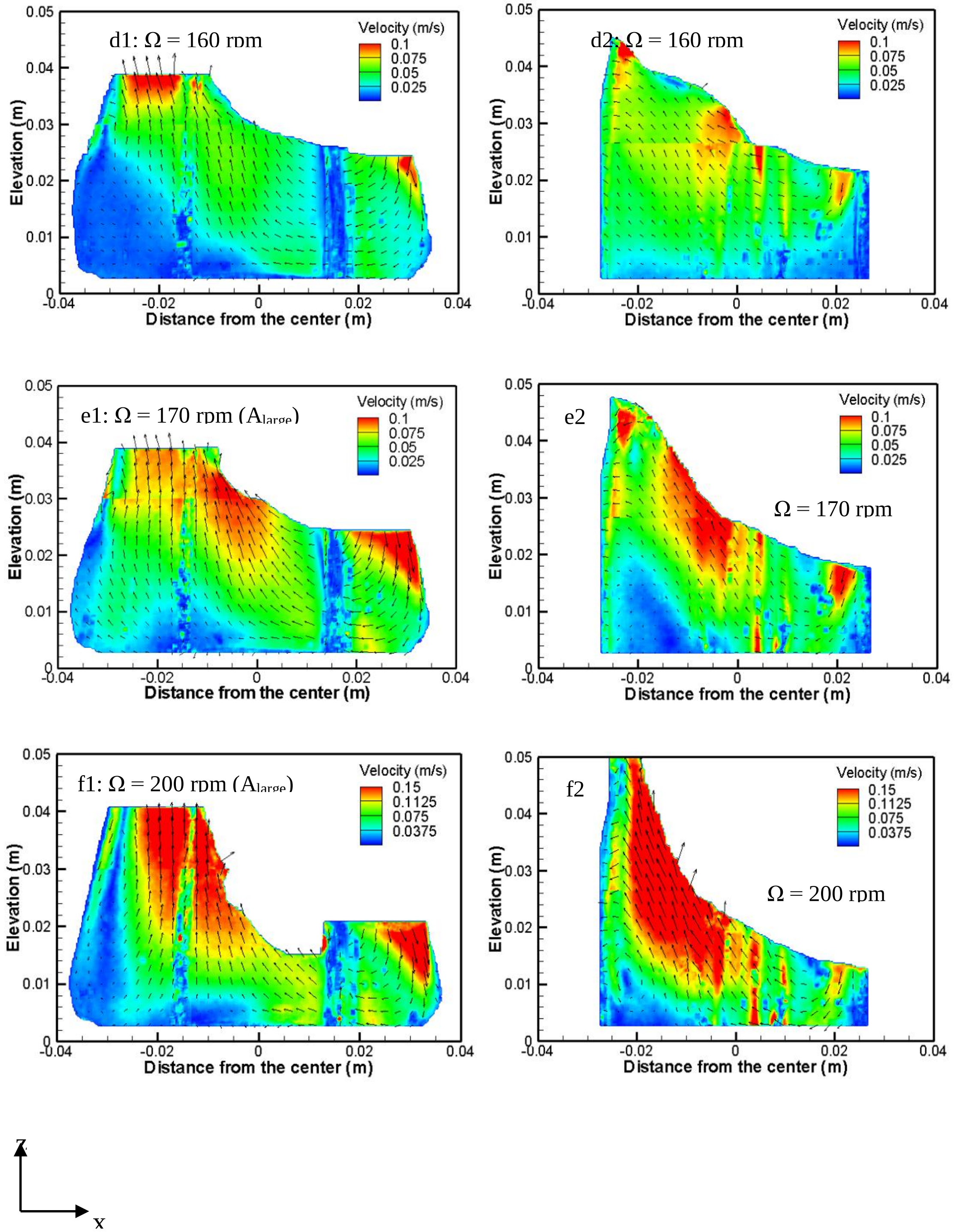

Figure 5.3 (Continued) Average velocity fields in the baffled flask for both large cross section (left panel) and small cross section (right panel) at seven rotation speeds of the orbital shaker: 100, 125, 150, 160, 170, 200, and 250 rpm. The water surface was found and masked for each rotation speed based on the images captured during the experiments.

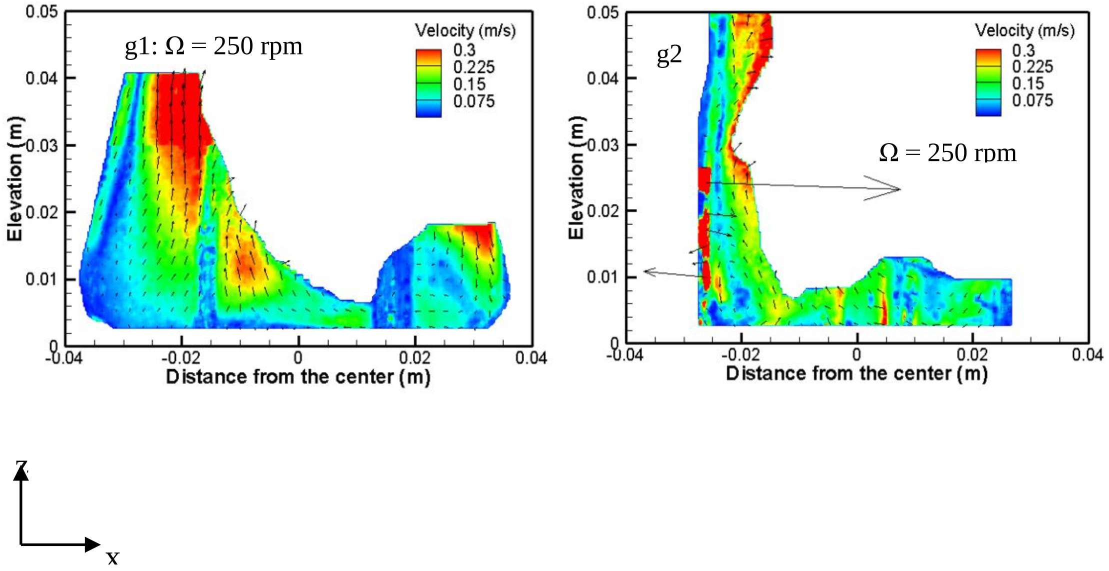

Figure 5.3 (Continued) Average velocity fields in the baffled flask for both large cross section (left panel) and small cross section (right panel) at seven rotation speeds of the orbital shaker: 100, 125, 150, 160, 170, 200, and 250 rpm. The water surface was found and masked for each rotation speed based on the images captured during the experiments.

The average velocities shown in Figure 5.3 were computed by taking the average over 200 realizations for both radial and axial water speeds. For large cross section (Figure 5.3, left panel), the zone of high speed velocity is essentially observed near the water surface, and moving downward as rotation speed increases. A zone of low speed occupies the lower portion of the flask at Ω ≤ 150 rpm. With the increase of the rotation speed, the water is more agitated throughout the flask. For Ω ≥ 170 rpm, the high speeds occur from the water surface down to the bottom and walls of the flask. Note that the flow in the flask is towards up left side of the wall because the measuring position is the furthest left side that the shaker moved to (Figure 5.1 (A)). The right and middle portion of the water surface decrease and the water flow are going more upwards on the left portion as the rotation speed increases also indicate that more intense turbulence occurs in the flask.

For small cross section (Figure 5.3, right panel), the high speed zone occurs on the left and middle portion from surface to bottom at Ω ≤ 200 rpm. The water flowing directions in the small cross section are similar to that in the large cross section (Figure 5.3, left panel), which are towards up left side of the flask wall, and going more upwards as Ω increases. Note that the average velocities in A_{small} appear to be larger than that in A_{large} for all rotation speeds. The relative differences of average velocities in the large and small cross sections are in the range of about 20-50% from large to small Ω. The simple explanation is that: as shown in Figure 5.2 (B) and 5.2 (C), A_{small} is about 30% smaller than A_{large}. Based on the mass conservations expressed as:

$$\overline{U}_{large}A_{large} = \overline{U}_{small}A_{small} \tag{5.7}$$

The mean velocity in the small cross section should be about 30% larger than that in the large cross section. Also, there exist dead zones with very small velocities (e.g. the bottom-left corner of the flask as shown in Figure 5.3 left panel) in the large cross section, which could also cause smaller average velocity in the large cross section. At Ω = 250 rpm, the water surface is very close to the wall and because of that, the wall and surface may have more impacts on the PIV measurements. Note that some high speed values are observed close to the left wall. Because of the boundary effects (water surface and wall) due to the extreme rotation speed, results shown in Figure 5.3 (g2) (Ω = 250 rpm in small cross section) may not present the real flow speed in the small cross section. The water were also highly aerated (more air bubbles are trapped in the water which could give extra reflection lights and may cause optical distortion) causing obstructions of the optical paths. Figure 5.4 shows an image of the bottom-left viewing area captured during the experiment at Ω = 250 rpm in the small cross section. The air bubbles are clearly shown in the water. The air bubbles and the agitated surface seem to give extra light reflections. Because of the effects of the wall and surface, measurements at Ω = 250 rpm for small cross section may not be eligible to present the water flow in the flask.

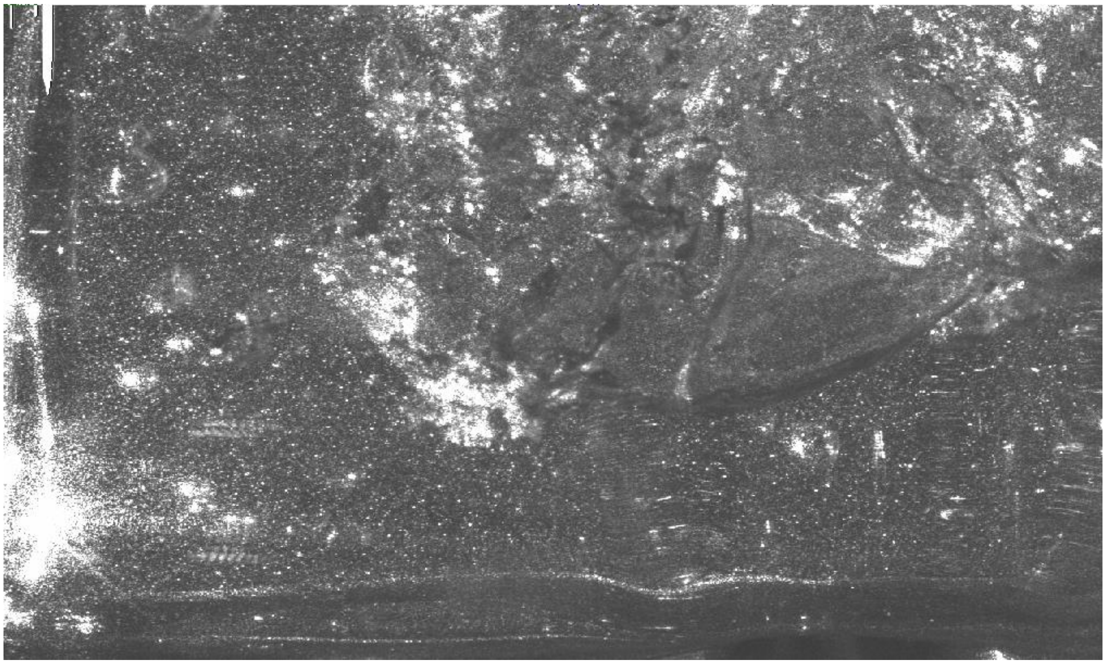

Figure 5.4 Image of the bottom-left viewing area in the small cross section captured from the experiment of Ω = 250 rpm.

Figure 5.5 shows the average velocity and its standard deviation at each realization. This average velocity (Figure 5.5 (A)) was calculated by averaging the magnitude of the two velocity components at each interrogation cell for each realization. The average velocities (Figure 5.5 (A)) are not deviate far from each other over the 200 realizations for each rotation speed, demonstrating the representative samples of these 200 replicates. The standard deviation of these 200 average velocities at each rotation speed is within the range of 3.12%-5.53% of the mean speed values (this mean was calculated by averaging the 200 average velocities shown in Figure 5.5 (A) for each rotation speed). Note that the deviations slightly increase as Ω increases, indicating that high speed flows introduce more uncertainties in the sampling. The standard deviation as shown in Figure 5.5 (B) is subject to the calculated velocity magnitude at each interrogation cell to the average for each realization. Similar to average velocities in Figure 5.5 (A), the evolution of standard deviation over the 200 realizations (Figure 5.5 (B)) shows the increases of standard deviation with the increase of Ω. This indicates that for small rotation speed, more uniform flow occur in the flask, but with the increase of rotation speed, the turbulent behavior is more intense, speed values are more random in the instantaneous velocity field。

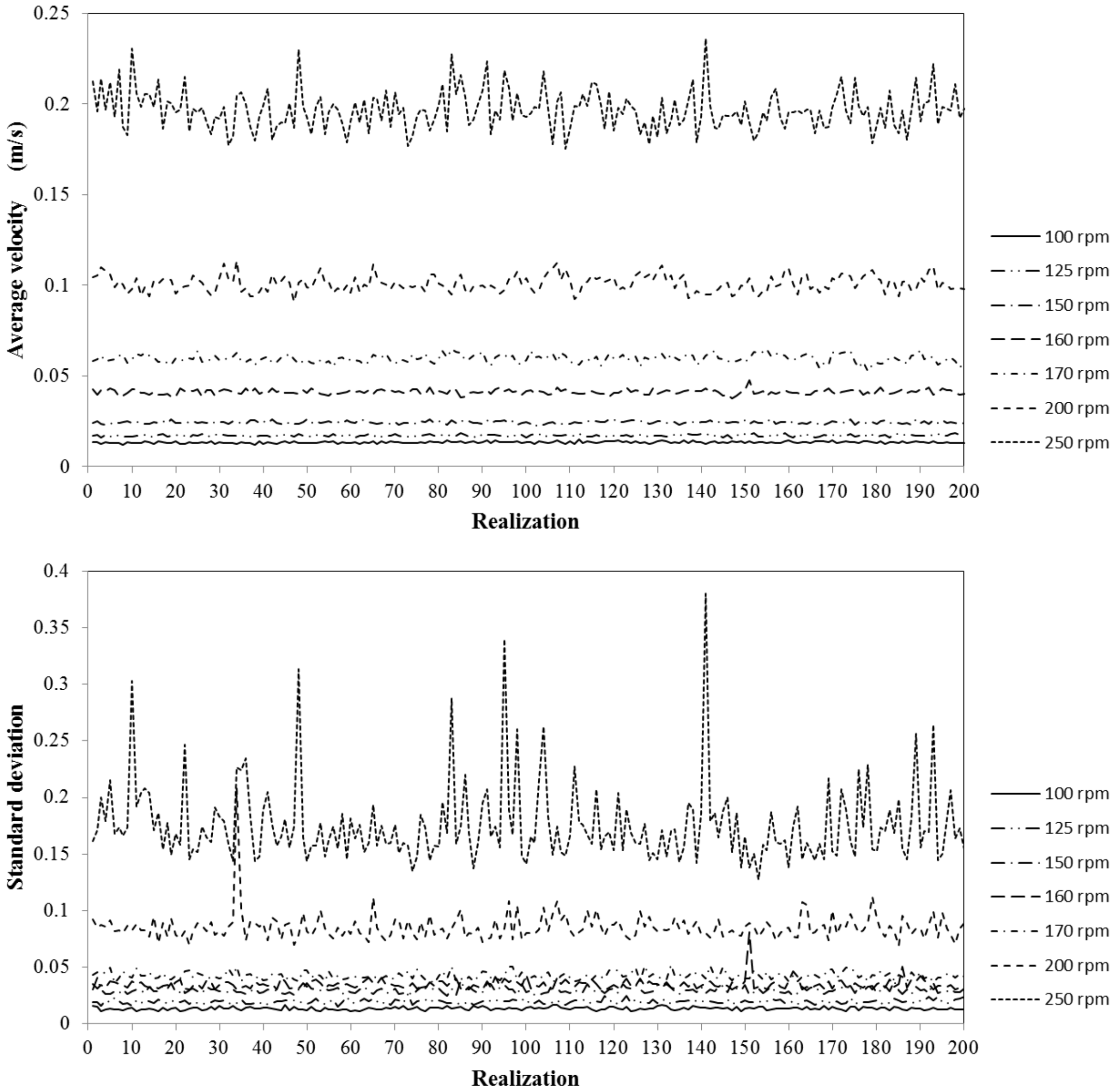

Figure 5.5 Average velocity $\overline{U}$ and its standard deviation as a function of the PIV realizations for the seven rotation speeds.

5.4.2 Energy Spectra Analysis

A quantitative means to detect the presence of turbulence is through evaluation of the Fourier spectrum, which represents the kinetic energy content at various scales. Based on Kolmogorov-Kraichnana predictions, for the inverse (energy) cascade of 2D turbulence, the spectra has the following property [86, 87]:

$$E(k) \propto k^{-5/3} \tag{5.8}$$

Where k is wave number (/m). Eq. 5.8 characterizes the existence of the inertial sub-range [78, 84].

Figure 5.6 contains plots of the logarithm of the energy spectra as a function of the wave number for the large cross section based on the magnitude of the velocity U (speed $U = \sqrt{U_x^2 + U_z^2}$) (Figure 5.6, left panel) and radial U_x and axial U_z velocities (Figure 5.6, right panel). The energy spectra of the small cross section are very similar to that of the large cross section and are not reported here for brevity. The calculations of 1D Fourier transform of the spatial data are obtained from velocity values on horizontal lines (in x direction of the cross section). The spectra are averaged along y according to a homogeneity hypothesis. Then averaging the spectral amplitudes on the 200 realizations is computed and presented in Figure 5.6. The theoretical – (5/3) slope based on Kolmogorov theory [87] is also plotted in the figures. At low wave number (large length scale), the spectrum scales in a different way and the energy decreases slower than – (5/3). The fluctuation energy is produced at the large eddies which also absorb some energy directly from the mean flow. This region is also called energy-producing or energy-containing range [83, 88]. The energy exchange between the mean flow and the turbulence is governed by the dynamics of the large eddies which contribute most to the turbulent production. Then the large eddies break down to smaller and smaller eddies and the energy cascade down the spectrum to high wave number region. For all spectra obtained from PIV measurements as shown in Figure 5.6, one could tell that there exists a region with – (5/3) slope which demonstrate the existence of the inertial sub-range and the presence of turbulent flow.

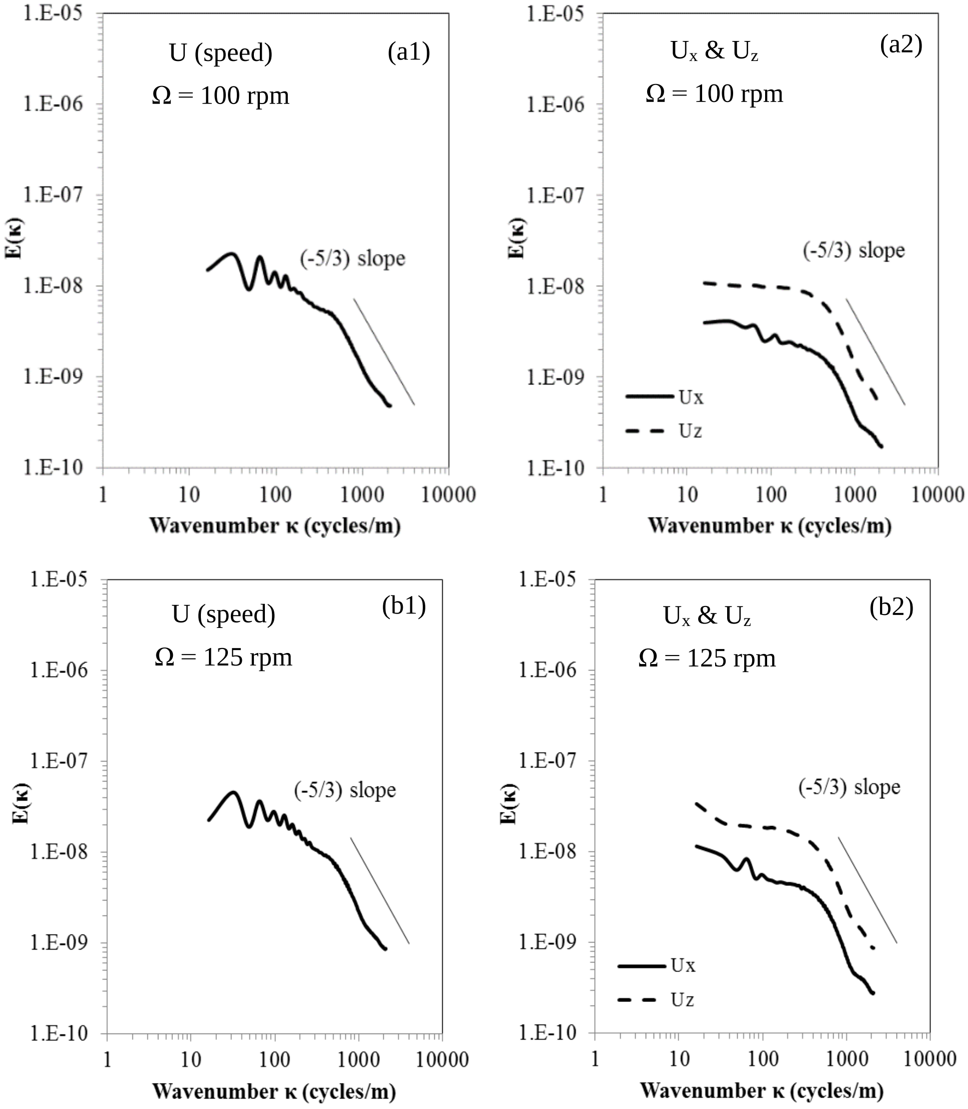

Figure 5.6 Average energy spectra over 200 realizations as a function of wavenumber in the large cross section (A_{large}) for all rotation speeds Ω = 100-250 rpm. Spectra were calculated horizontally (in x direction of the cross section) based on the spatial data of turbulent velocities in the baffle flasks. The left panel is the average spectra of the velocity speed, and the right panel is the average spectral of the radial (U_x) and axial (U_z) velocities (continued).

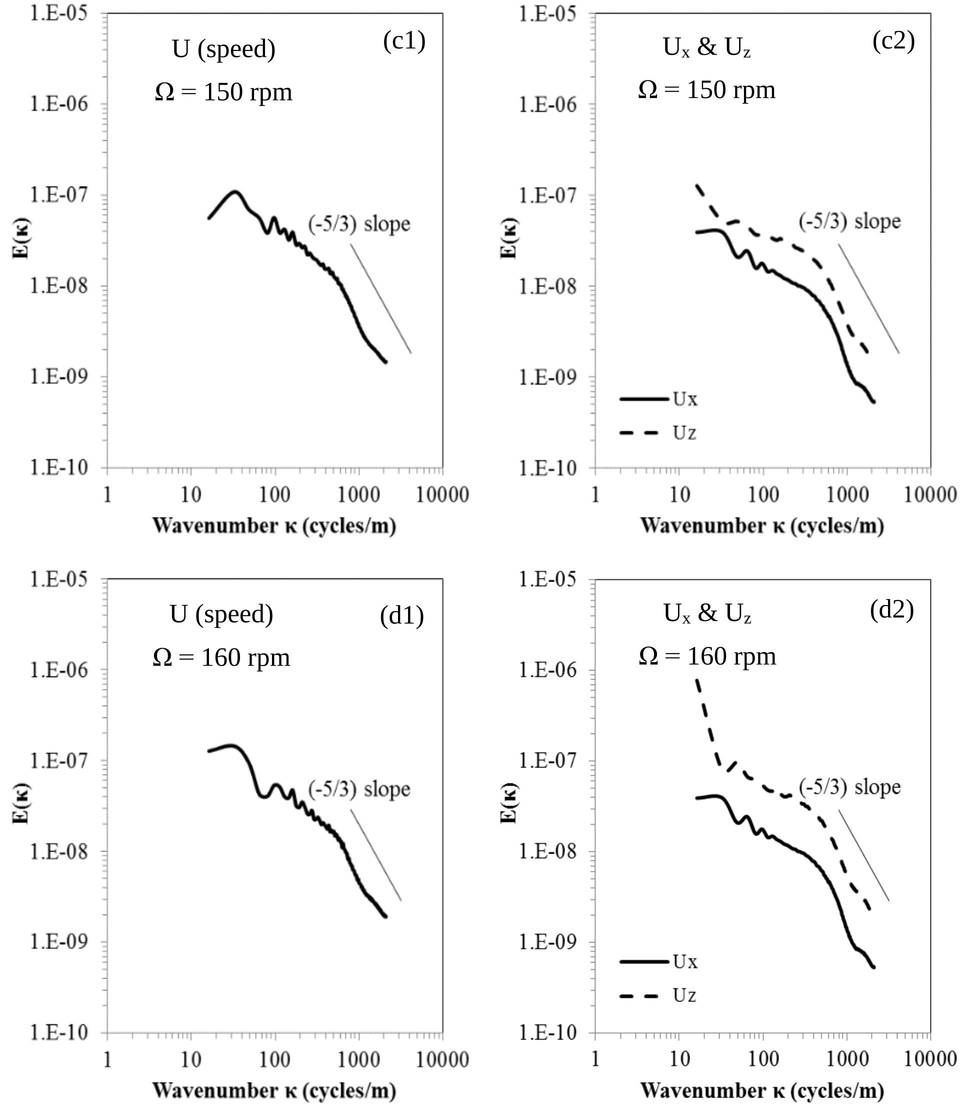

Figure 5.6 (Continued) Average energy spectra over 200 realizations as a function of wavenumber in the large cross section (A_{large}) for all rotation speeds $\Omega = 100$-250 rpm. Spectra were calculated horizontally (in x direction of the cross section) based on the spatial data of turbulent velocities in the baffle flasks. The left panel is the average spectra of the velocity speed, and the right panel is the average spectral of the radial (U_x) and axial (U_z) velocities.

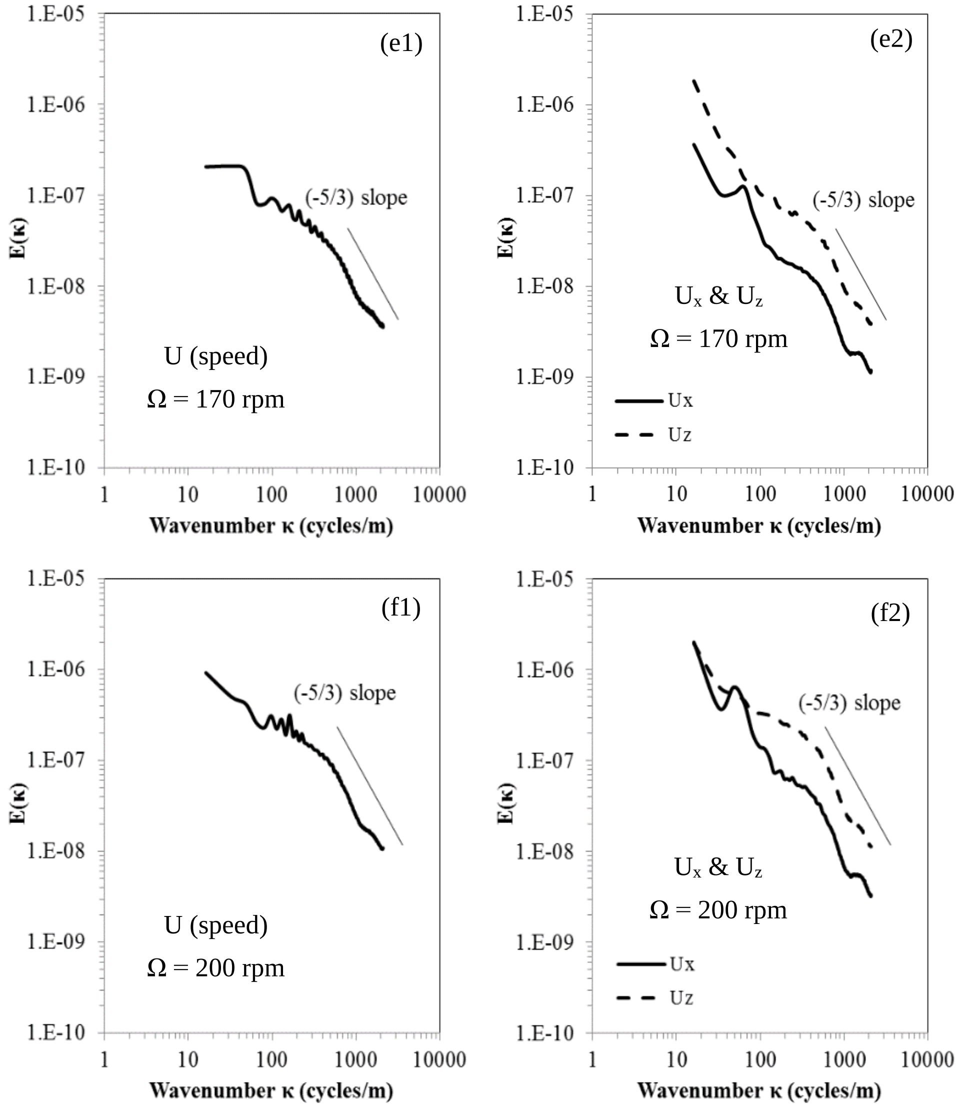

Figure 5.6 (Continued) Average energy spectra over 200 realizations as a function of wavenumber in the large cross section (A_{large}) for all rotation speeds Ω = 100-250 rpm. Spectra were calculated horizontally (in x direction of the cross section) based on the spatial data of turbulent velocities in the baffle flasks. The left panel is the average spectra of the velocity speed, and the right panel is the average spectral of the radial (U_x) and axial (U_z) velocities.

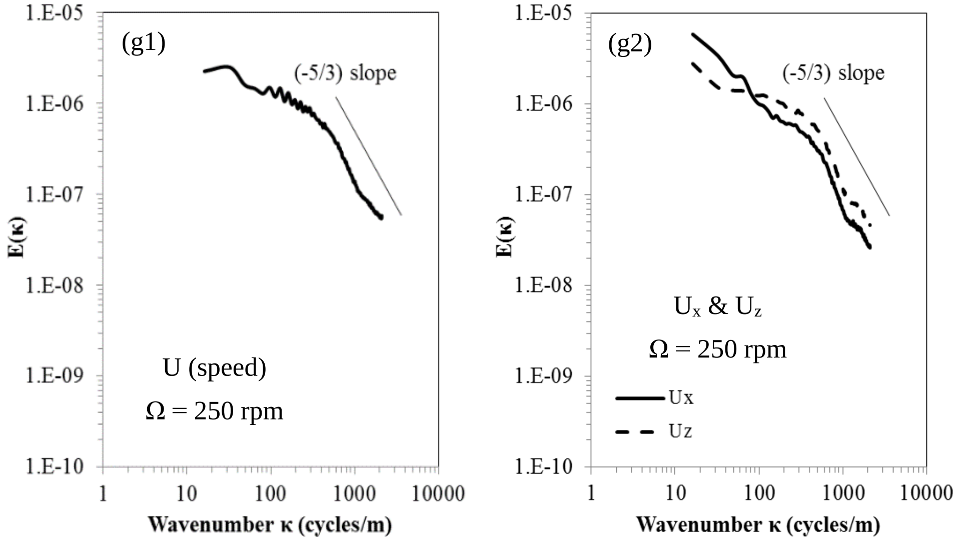

Figure 5.6 (Continued) Average energy spectra over 200 realizations as a function of wavenumber in the large cross section (A_{large}) for all rotation speeds Ω = 100-250 rpm. Spectra were calculated horizontally (in x direction of the cross section) based on the spatial data of turbulent velocities in the baffle flasks. The left panel is the average spectra of the velocity speed, and the right panel is the average spectral of the radial (U_x) and axial (U_z) velocities.

The energy spectra of the radial U_x and axial U_z velocities (Figure 5.6, right panel) are not exact the same, but they are comparable. The energy from U_z is slightly larger than that from U_x. The relative differences of log (E) between radial and axial velocities are in the range of 3.2-6.9% for all rotation speeds. This may indicate nearly isotropic turbulence in the plane. Note that the energy spectra of radial and axial velocities at Ω = 250 rpm (Figure 5.6 (g2)) are very close, which could demonstrate the local isotropy exists at the highest intensity flow in this study. It is also noticed that the energy increases with the increases of the rotation speed. As noted that for all the rotation speed, the scale of the energy spectrum is changed at a small wavelength λ of about 1 mm (the wavenumber κ ≈

1000 cycles/m). This may be caused by the fundamental spatial resolution of the PIV measurement (about 0.95 mm width of the interrogation cell) that the turbulent behavior in the smaller scale is not properly captured due to the limitations of the instrument in the current study, which gives a white noise in the small wavelength of the spectra. The scale exponent of turbulent structure could be different for spatial large scale and small scale flows in the baffled flask [89]. A further investigation on the scaling exponents of structure functions in the baffled flask is still needed in future studies.

Figure 5.7 shows the average energy spectra on one realization for $\Omega = 100$ rpm (top figures) and $\Omega = 200$ rpm (bottom figures) for both velocity speed and two velocity components. Compare to the spectra in Figure 5.6 (a) and 5.6 (f), the spectra of one realization are noisier due to the more random behavior of instantaneous velocity at one realization. The energy spectra at small scale wavelength $\lambda < 1$ mm (the wavenumber $\kappa >$ 1000 cycles/m) appear to be more like noises. This may well confirm the early statement that the change of turbulent structure scale observed in the average spectra over 200 realizations is due to the fundamental spatial resolution of the PIV measurements adopted in the current study.

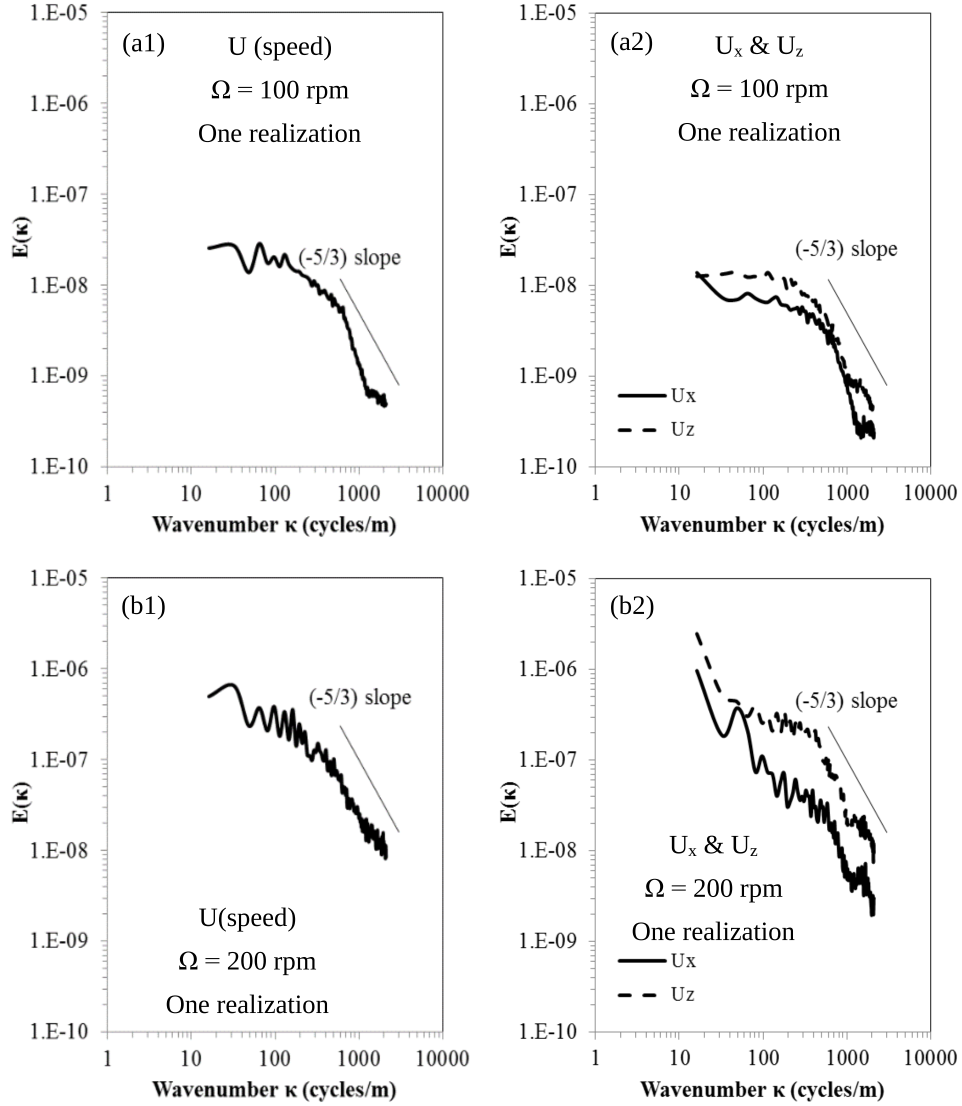

Figure 5.7 Average energy spectra of one realization as a function of wavenumber in the large cross section (A_{large}) for Ω = 100 (top) and Ω = 200 rpm (bottom). Spectra were calculated horizontally (in x direction of the cross section) based on the spatial data of turbulent velocities in the baffled flasks. The left panel is the average spectra the velocity speed, and the right panel is the average spectral of the radial (U_x) and axial (U_z) velocities.

Figure 5.8 shows the 1D average energy spectra of 200 realizations calculated from velocities on the vertical lines (in z direction of the cross section) for Ω = 100 rpm (top figures) and Ω = 200 rpm (bottom figures). Comparing with the average spectra in

Figure 5.6 (a) and 5.6 (f) (calculated from the velocities on the horizontal lines), the spectra are similar. The energy-producing region (low wave number) is smoother (less fluctuated) than the spectra calculated from the horizontal lines. This is because the rotational behavior of the large eddies in the horizontal direction (the flask is mounted on the rotational shaker as shown in Figure 5.1 (A)). Note that the slope of the energy spectra for the axial velocities U_z is closer to the – (5/3) slope than that for the radial velocities U_x. This could be reasonable because the radial velocity exhibit more rotational movement of the flow, while the axial velocity presents more of the energy cascade of 2D turbulence.

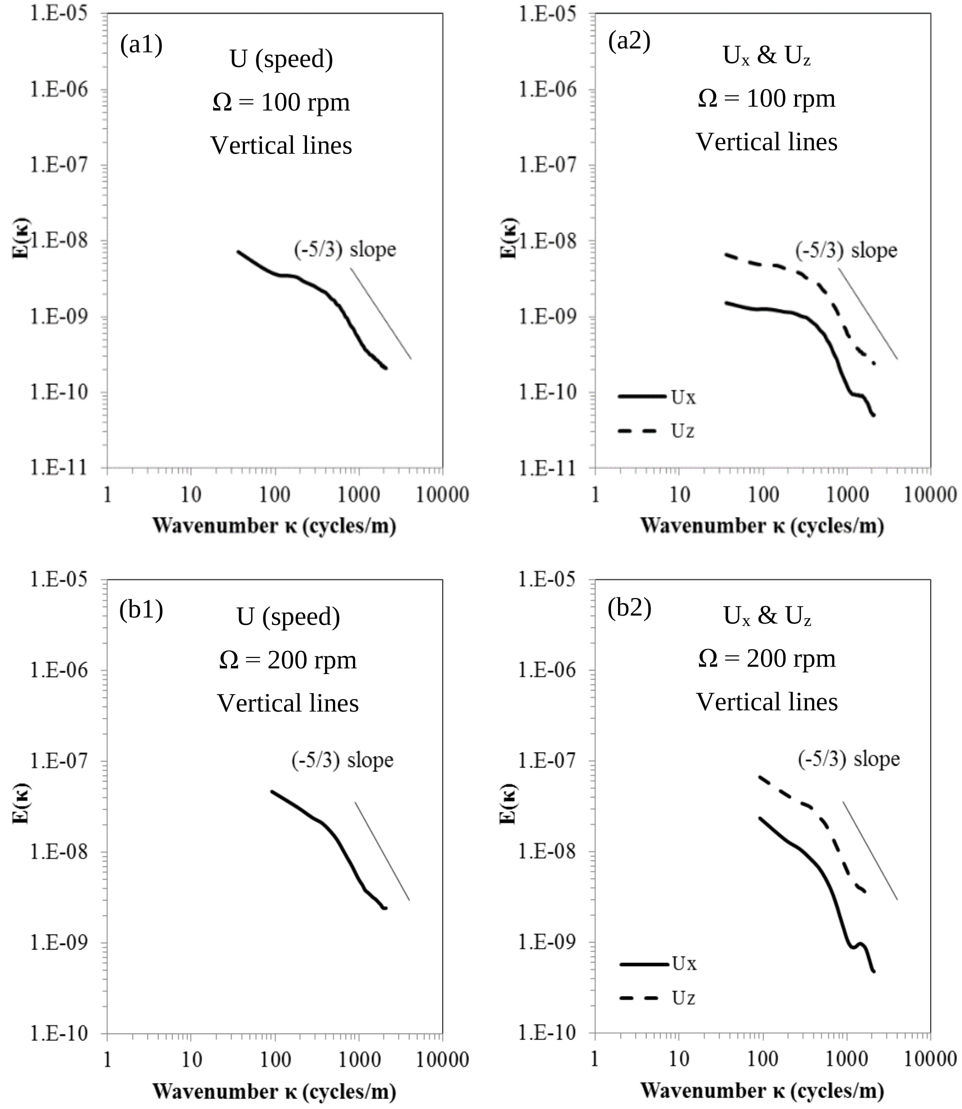

Figure 5.8 Average energy spectra over 200 realizations as a function of wavenumber in the large cross section (A_{large}) for Ω = 100 (top) and Ω = 200 rpm (bottom). Spectra were calculated vertically (in z direction of the cross section) based on the spatial data of turbulent velocities in the baffle flasks. The left panel is the average spectra the velocity speed, and the right panel is the average spectral of the radial (U_x) and axial (U_z) velocities.

5.4.3 Energy Dissipation

The energy dissipation rate, ε, was estimated using Equation 5.2 with the coefficient "A" set equal to 1.0. To obtain integral length scale, the autocorrelation coefficient was calculated based on 1D spatial turbulent velocity for each realization. Figure 5.9 shows the normalized autocorrelation functions in all direction of the large cross section for $\Omega = 100$, 125, 150, 170, 200, and 250 rpm. Similar results were obtained for all other cases (small cross section and other rotation speeds). The autocorrelation function rapidly descends to zero within 5-20 mm distance lag, indicating that the autocorrelation function is not periodical rather presents chaotic (or random) behavior. The functions in the two directions (horizontal and vertical) of the cross section for each velocity components are similar to each other, may also indicating the validity of isotropic flow. The integral length scale was evaluated for each realization by integrating from length zero to the length of first zero crossing of the autocorrelation function. The trapezoidal rule was used for the numerical integration of Eq. 5.3. Then the average integral length scale was obtained by taking the average of integral length scales in the two directions for all 200 realizations.

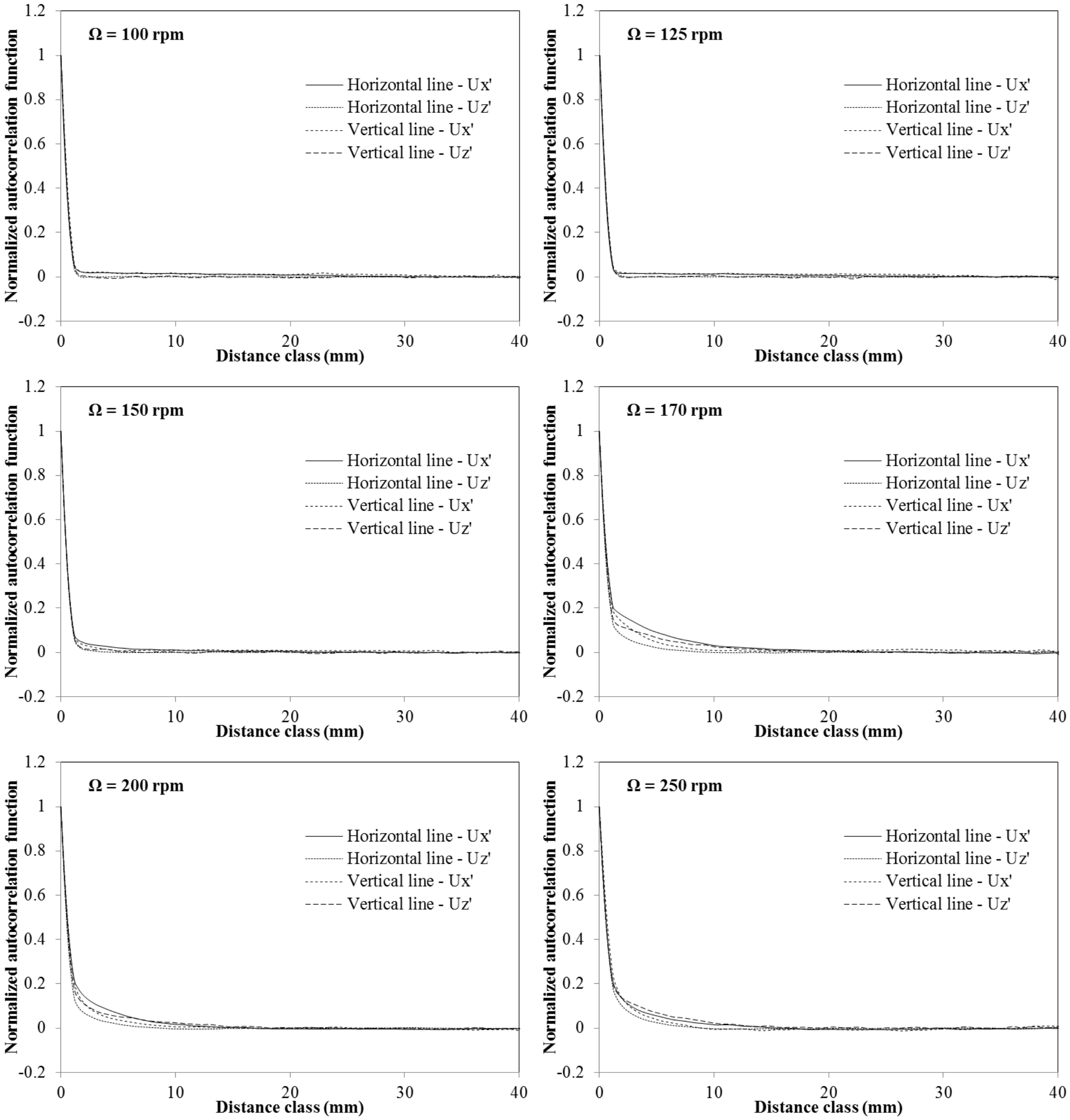

Figure 5.9 Autocorrelation functions calculated based on the turbulent components of the velocities in the large cross section for rotation speeds of 100, 125, 150, 170, 200, and 250 rpm. Integration of Eq. 5.3 occurs until the first zero crossing on the distance lag axis.

Energy dissipation rate was estimated based on Equation 5.2 for both radial (U_x) and axial velocities (U_z). The root mean square of turbulent component of radial and axial velocities were computed based on the speed values of 200 PIV realizations at each interrogation cell. Then the energy dissipation rate was calculated for both radial and axial velocities at each interrogation cell based on the corresponding root mean square velocity and the average integral length scale. The average energy dissipation rate is the average of the two velocity components (radial and axial).

Figure 5.10 shows the contour plots of the average energy dissipation rate in the large (left panel) and small cross section (right panel). In the large cross section, the energy distribution is similar for Ω = 100 rpm and Ω = 125 rpm, where the zone with high ε is distributed along the baffles. At Ω = 150, 160 rpm, high ε zone shows on the top-left portion close to the surface which is expected because that is the high velocity zone located (Figure 5.3). At Ω ≥ 170 rpm, high ε is distributed downwards and throughout the cross section, especially on the left and right portion. For small cross section, similar to the findings from velocity fields of the turbulent components, relatively high ε is observed at the area close to the center of the flask. Future studies of the energy distribution on the horizontal plane (horizontal cross sections at different elevations) may provide more insights on this. The distributions are similar at Ω ≤ 160 rpm with slight increase of ε on the water surface as Ω increases. At Ω ≥ 170 rpm, as in the large cross section, high ε is also distributed throughout the cross section, demonstrating that the turbulence is intense under such high rotation speed. At the extreme case of Ω = 250 rpm in the small cross section, the water is basically accumulated close to the left wall of the cross section, and very high ε is generated in that region. However, as discussed above, because the high intensity of the turbulence and the water is so close to the wall and water surface, also with the air bubbles trapped in the water (Figure 5.4), the quality of the PIV measurements for this extreme case is in questioning. Therefore, results of Ω = 250 rpm in the small cross section will not be presented below. Further investigations are needed for this case and new technology may be needed.

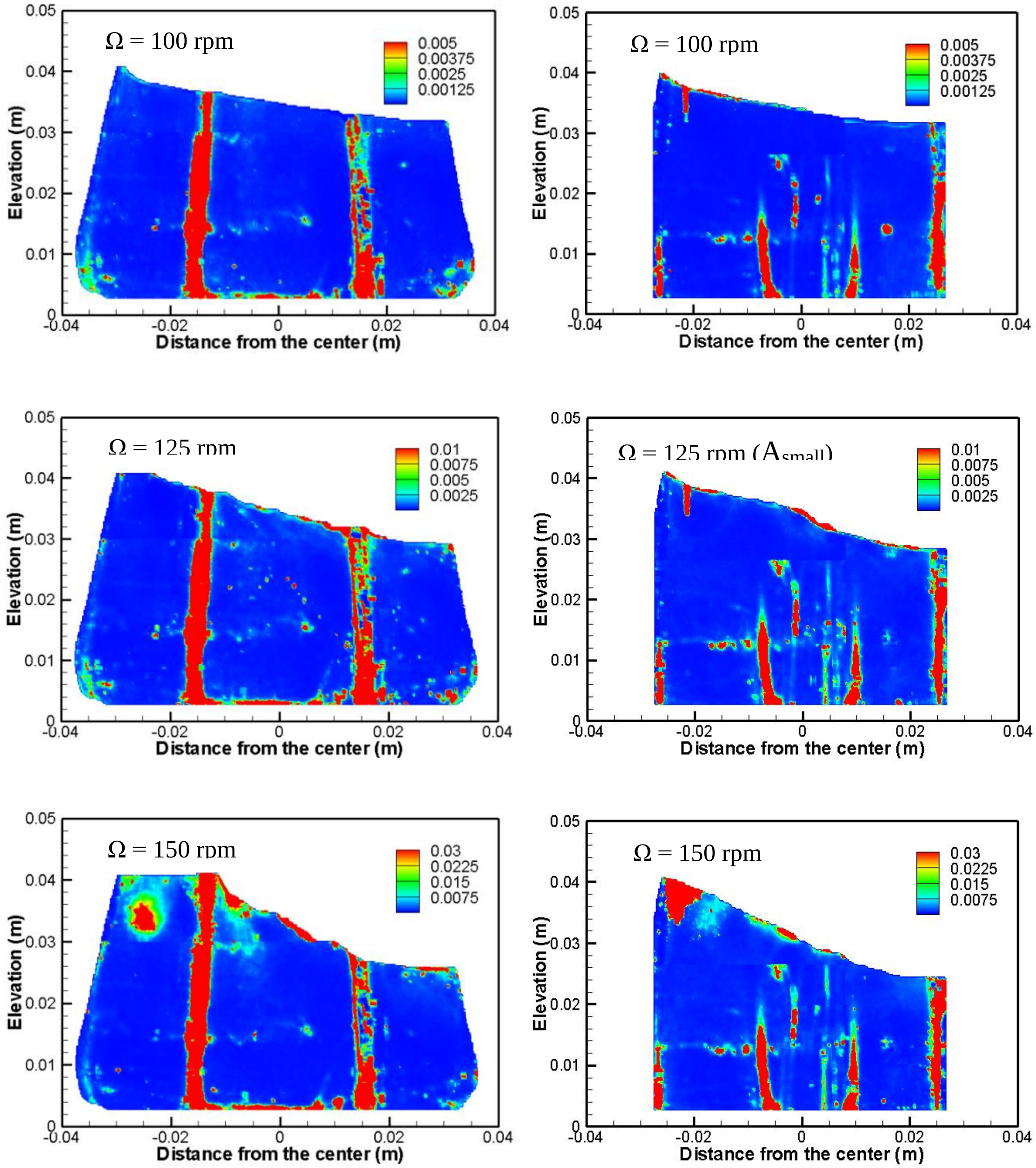

Figure 5.10 Contour plots of average energy dissipation rate in the baffled flask for all rotation speeds in the large cross section (left panel) and small cross section (right panel). Labels represent values of ε (W/kg) (continued).

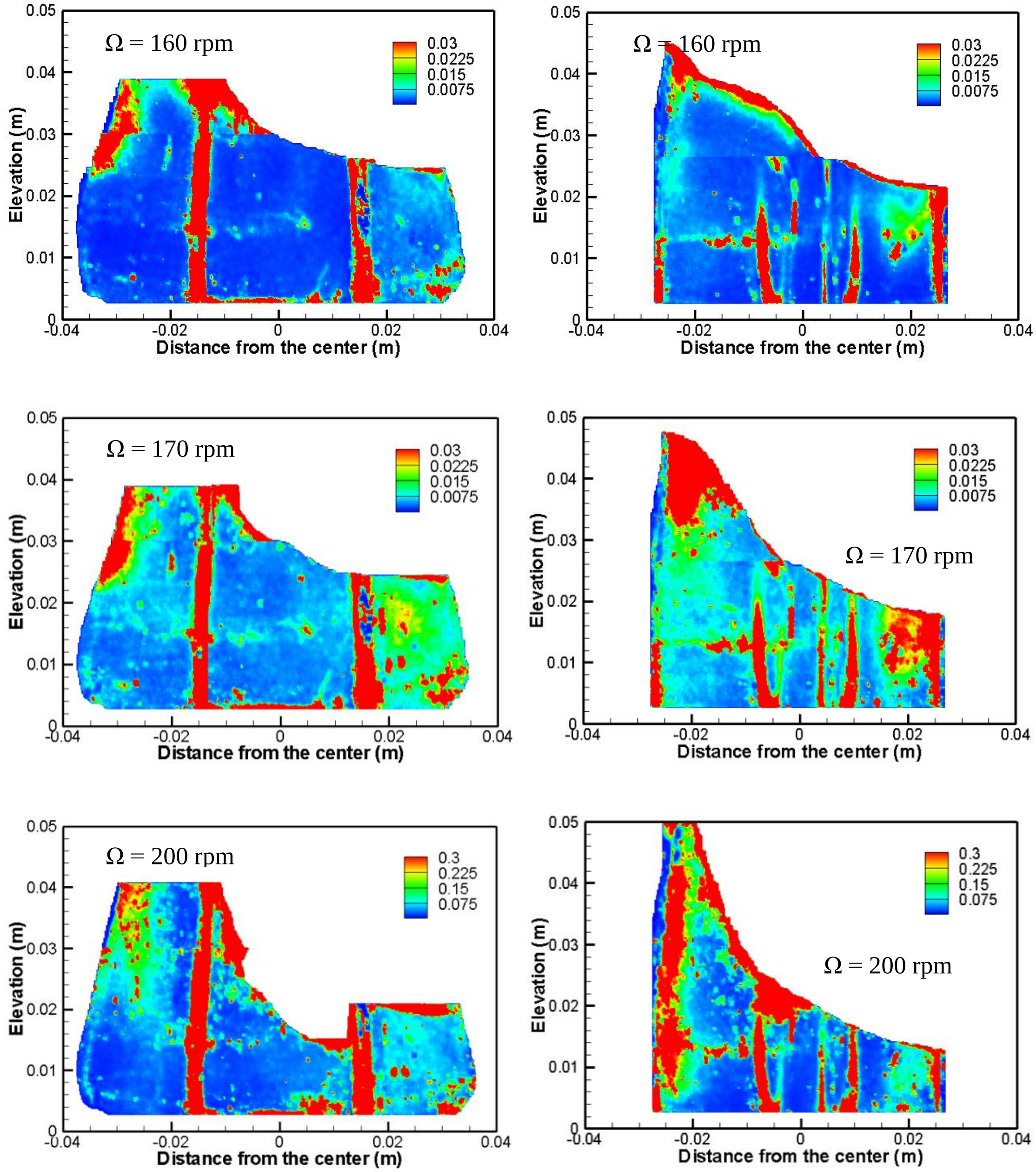

Figure 5.10 (Continued) Contour plots of average energy dissipation rate in the baffled flask for all rotation speeds in the large cross section (left panel) and small cross section (right panel). Labels represent values of ε (W/kg).

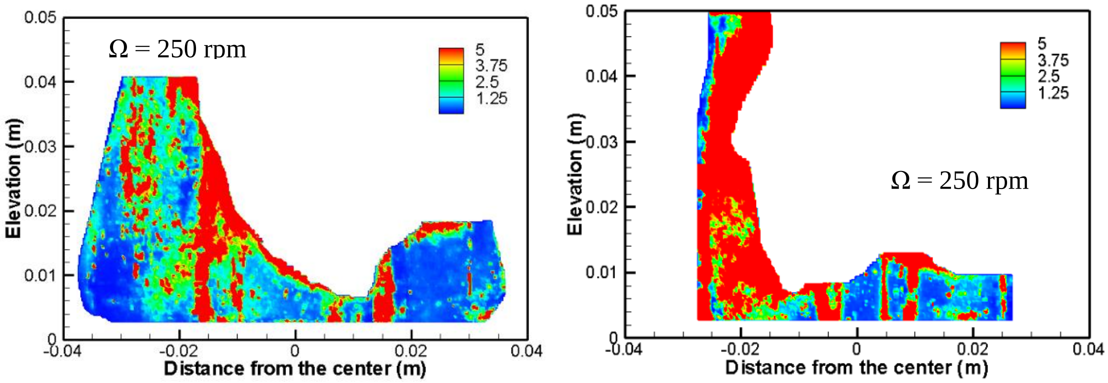

Figure 5.10 (Continued) Contour plots of average energy dissipation rate in the baffled flask for all rotation speeds in the large cross section (left panel) and small cross section (right panel). Labels represent values of ε (W/kg).

The average energy dissipation rate was obtained for each rotation speed by taking the ε values of all interrogation cells in the cross section and plotted in Figure 5.11 as a function of rotation speed. The average ε in the baffled flask increase with the increases of rotation speed. Considering all the points in Figure 5.11 for both large and small cross section, the average energy dissipation rate appears to be increase exponentially with the rotation speed,

$$\bar{\varepsilon} = 9.0\times10^{-5} Exp[0.043\Omega] \text{, with } R^2=0.97 \qquad (5.9)$$

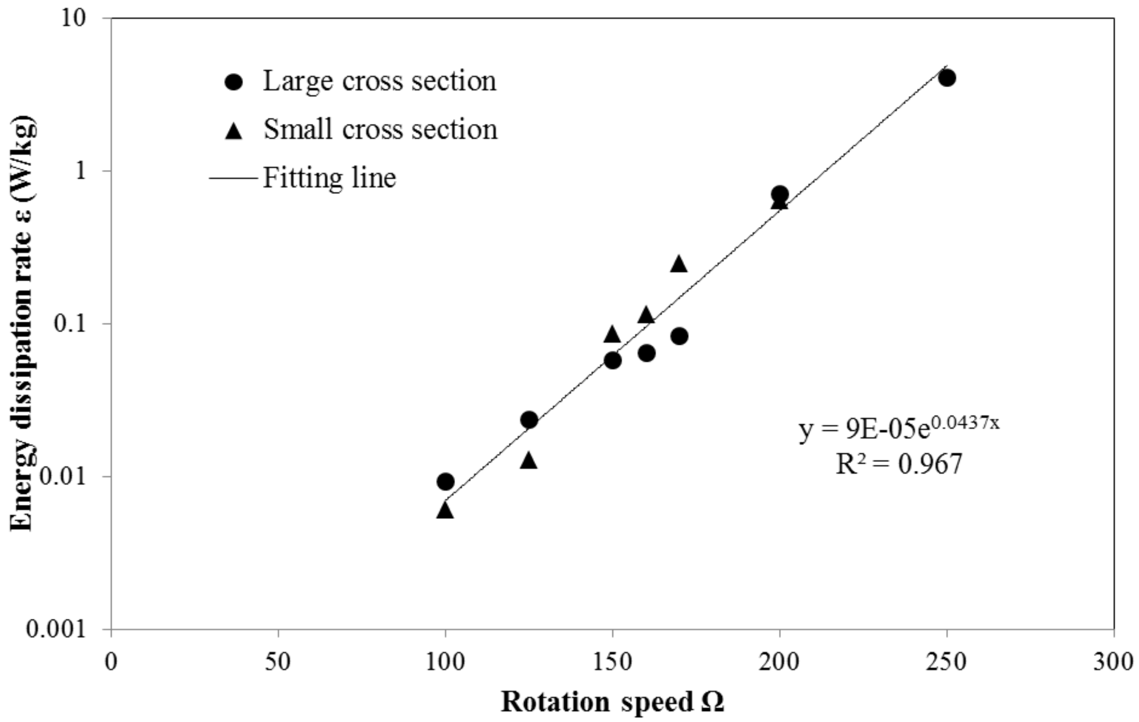

Figure 5.11 Variation of energy dissipation rate ε as a function of the rotation speed for the large and small cross sections.

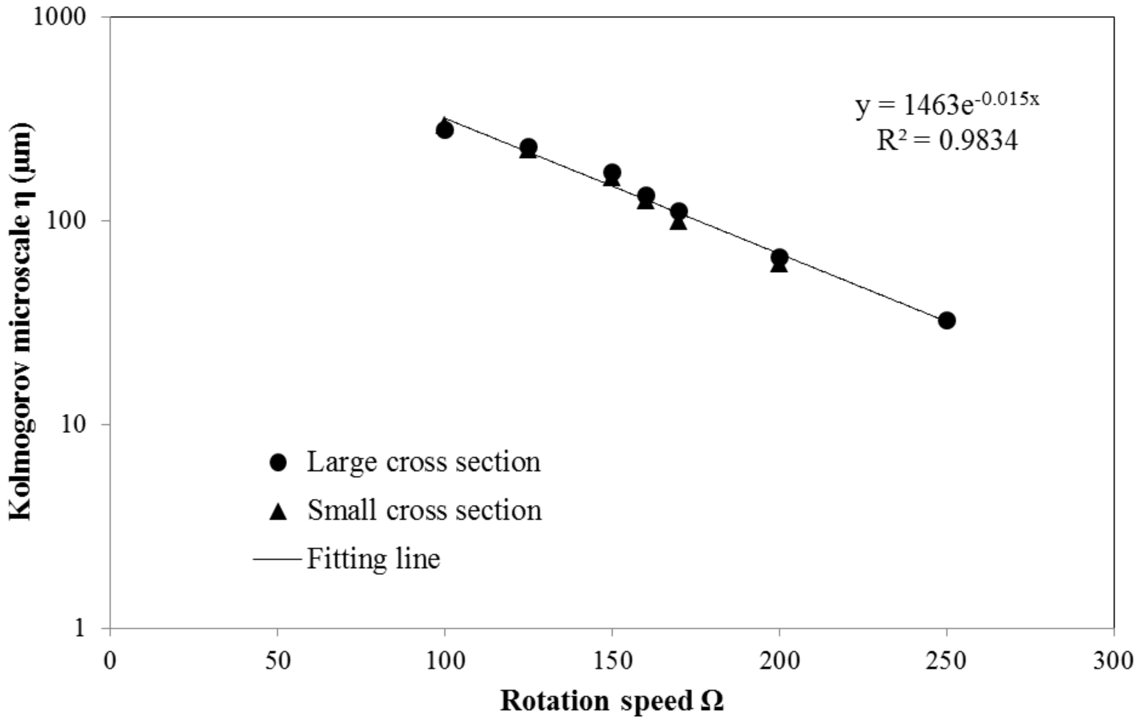

Figure 5.12 Variation of Kolmogorov microscale η as a function of the rotation speed for the large and small cross sections.

The average Kolmogorov scale and velocity gradient was calculated based on Equations 5.5 and 5.6 using the energy dissipation rate for each velocity components (radial and axial) at each PIV interrogation cell, and then taking the average for each rotation speed. Figure 5.12 shows the results of the average Kolmogorov microscale in both large and small cross sections. The value decreases from 296 to 32 μm with the rotation speed increases from 100 to 250 rpm. Similar to energy dissipation rate (Figure 5.11), a fitting line is generated using the data from both large and small cross section,

$$\bar{\eta} = 1463 Exp\left[-0.015\Omega\right], \text{ with } R^2=0.98 \tag{5.10}$$

The mean velocities increase from 0.017 to 0.14 m/s with the rotation speed increases from 100 to 250 rpm. The RMS velocity also increases with the increase of Ω. The integral length scales at Ω ≤ 160 rpm has the same magnitude with 0.63-0.69 mm for Ω = 100-150 rpm and 0.91 mm for Ω = 160 rpm. Then the integral length scales increase an order of magnitude at Ω ≥ 170 rpm to 1.19-1.27 mm. The average energy dissipation rates are in the range of 7.65×10^{-3}- 4 W/kg for the rotation speed investigated in the current study (Ω = 100-250 rpm). The Kolmogorov scales estimated in this study for all seven rotation speeds (32 – 296 μm) are well in the range of the sizes of oil droplets observed at sea, which is 50-400 μm [82]. The velocity gradient increases from 26.3 to 1472.6 /s based on the measurements obtained in this study. Kaku et al. [5] suggested that the energy dissipation rate ε is more presentative of the turbulent intensity because ε could be stipulated based on the law of conservation of energy while there is no law that requires the conservation of velocity or its gradient.

5.5 Discussion

Rather than single-point velocity measurement techniques (e.g. HWA), the PIV system can provide a 2D or 3D instantaneous velocity fields depending on the system chosen. However, the limitations of using the PIV system should be recognized and considered during the experiments. There are many sources can introduce errors in the PIV measurements such as CCD camera noise, tracer characteristics, light scattering, and velocity gradient [90]. As presented in this study that air bubbles are trapped in the water of $\Omega = 250$ rpm in small cross section (Figure 5.4), air bubbles are also found for some of the other high speed experiments in both cross sections. The effects of air bubbles and other error sources on the results presented in this study require further investigations in the near future.

The velocity value from PIV measurements is not speed value at a single point like the one measured by HWA rather than an average velocity of each interrogation cell [85]. Bounded by the measuring techniques and capacity of the instruments (e.g., camera and laser), compromise has to be made between spatial resolutions and accuracy of the measuring data as discussed earlier in the paper. Such compromise could also limit the methods used for analyzing the energy distribution and turbulent structure within the vessel (e.g. energy dissipation rate estimation). In the current study, the most widely used energy dissipation estimation method – dimensional argument analysis was chosen to compute the ε. In theory, this method applies only to turbulence that is homogeneous, isotropic, and in spectral equilibrium, but in practice, it is rather difficult to meet these conditions [80]. The fine-scale structure of most actual non-isotropic turbulent flows is locally nearly isotropic, therefore many features of isotropic turbulence may thus be applied to phenomena in actual turbulence that are determined mainly by the fine-scale structure [91, 92]. Results of energy spectra shown in the previous section demonstrate a nearly isotropic flow and the existence of inertial subrange, which validate the use of dimensional argument analysis (Eq. 5.2) to estimate ε in the current study. However, it was reported that the dimensional argument analysis could produce reliable average energy dissipation but may be incorrect when local ε values and distribution are estimated [93]. Further investigations using different dissipation rate estimation techniques are conducted in the on-going studies.

Table 5.1 shows the comparison of the average turbulent parameters between the current study and the one from Kaku et al. [5, 68] for Ω = 100, 200 rpm. The mean velocities from Kaku et al. are slightly larger than the ones from the current study. This is expected because as discussed above, the HWA used in Kaku et al. is a single point velocity measuring instrument, while PIV measurements are the average velocity in each interrogation cell. The energy dissipation rate estimated in this work is slightly larger than the one estimated by Kaku et al. The reasons may rely on that the instruments are different from one another, Kaku et al. used Hotwire which can only measure the point velocities while PIV gives spatial velocity fields. Because of this, Kaku et al. used temporal autocorrelation function to estimate the dissipation rate, while in this work we calculated spatial autocorrelation and the integral length scale for the estimation of ε.

Table 5.1 Comparison of Average Turbulent Parameters with Data From Kadu et al. [5,68]

Rotation speed (rpm)	Data Source	Mean Velocity (m/s)	RMS Velocity U_{rms} (m/s)	Average Energy Dissipation Rate $\bar{\varepsilon}$ (W/kg)	Kolmogorov Microscale $\bar{\eta}$ (μm)	Average Velocity Gradient $\overline{G}$ (/s)
100	Current study	1.74×10^{-2}	6.28×10^{-3}	7.65×10^{-3}	287.5	26.3
	Kaku et al. [5, 68]	6.31×10^{-2}	3.68×10^{-3}	4.78×10^{-4}	276.7	17.2
200	Current study	8.81×10^{-2}	5.62×10^{-2}	6.70×10^{-1}	63.8	446.7
	Kaku et al. (2006a, b)	5.33×10^{-1}	4.95×10^{-2}	1.63×10^{-1}	57.0	349.9

5.6 Conclusion

Measurements of the water velocity in the Baffled Flask were obtained using Particle Image Velocimetry (PIV) for seven rotation speeds of 100, 125, 150, 160, 170, 200, and 250 rpm. Two vertical cross sections were measured to obtain the velocity profiles in the flask: the one with largest diameter of the flask, and the one with the smallest diameter. The 1D energy spectra indicate nearly isotropic flow in the BF for all rotation speeds and the existence of inertial subrange, which validate the use of dimensional argument analysis for the estimation of energy dissipation rate. Noises were also observed in spectrum at smaller scale than the fundamental spatial resolution of the PIV measurements. The energy dissipation rate was estimated using dimensional argument for both cross sections, and the overall dissipation rates were the average of the results from the two cross sections. An exponential model was created for both average energy dissipation rate and Kolmogorov microscale as a function of rotation speed with $R^2 \geq 0.97$. The estimated average energy dissipation rates are in the range of 7.65×10^{-3}- 4 W/kg for rotation speeds of $\Omega = 100$-250 rpm, of which it is slightly larger than the one estimated by Kaku et al. [5, 68] for $\Omega = 100$ and 200 rpm. The Kolmogorov scale estimated in this study for all seven rotation speeds approached the size of oil droplets observed at sea, which is 50-400 μm [82].

CHAPTER 6

CONCLUSIONS

In this work, a number of laboratory apparatuses were studied from an engineering perspective, with special regard to their hydrodynamics under different operating conditions. More specifically, the systems that were examined here are the following:

- USP Dissolution Testing Apparatus 2 with and without automatic sampling probes
- Dissolution testing mini vessel apparatuses
- Baffled shaker flasks

For the first of these systems, a dissolution testing USP Apparatus 2 provided with a fiber optic probe, CFD simulations of the hydrodynamics in the standard system and in the testing system with the probe have shown that the overall flow pattern in the USP 2 system is not significantly affected by the presence of the probe. However, the probe slightly but consistently alters the velocity profiles especially in some regions inside the vessel. In particular, in the bottom zone, which is the most critical zone because this is where the dissolving tablet is typically located during a dissolution test, the velocity increases appreciably in the probe system compared to the standard system. This can be shown not only in the simulation results, but also in the experimental results with PIV.

Actual dissolution tests were conducted, and they showed that, consistently with the CFD and PIV results, tablets in the testing system have higher dissolution profiles than in the standard system, especially when located in specific zones. This is also in agreement with the hydrodynamics results since the largest velocity differences can be observed, with and without the probe, at the same locations where the tablets produced higher dissolution rates. Therefore, both the experiment results and the CFD simulations show that the presence of an optic probe can introduce hydrodynamic changes in USP 2 dissolution apparatus and that the resulting hydrodynamic effects appear to influence the tablet dissolution rate observed in dissolution experiments.

Similarly, the hydrodynamics of mini vessels was investigated computationally (by conducting CFD simulations) and experimentally through PIV. The hydrodynamics was studied at four different agitation speeds and the velocity distributions were compared with those in the standard USP Apparatus 2 system. CFD simulations were first conducted without a tablet on the bottom of the mini vessel. Special attention was paid to the determination of the velocity distribution in the region below the impeller in order to compare the fluid dynamic regime experienced by tablets in both the mini vessel system and the USP 2 apparatus. In the most important zone, i.e., the inner core zone at the vessel bottom, the velocities were similar on the lowest iso-surface, especially for the axial velocity at 100rpm and 125rpm in the mini vessel compared with 100rpm in 900mL USP 2 system. This was not clearly the case for iso-surfaces above the bottom zone.

Strain rates were obtained from the CFD simulations for different agitation speeds in the mini vessel and compared with those in the standard system. Additionally, the mass transfer coefficient between a virtual tablet place at the vessel bottom and the surrounding fluid was calculated based on a rotating disk and rotating cylinder models and compared with mass transfer similarly obtained previously in the USP 2 system. In general, the values of the strain rate at the wall in mini vessels increased as the agitation speed increased. At 125rpm and 100rpm the strain rates on the surface of the virtual tablet in in the mini vessel, were similar to the corresponding strain rate values at 100rpm in the 900mL USP 2 system.

Even in mini vessels, the poorly mixed central inner core zone below the impeller persisted at high agitation speed, although this zone shrank as the agitation speed increased. The predicted strain rate and mass transfer coefficients from a virtual tablet to the fluid also increased as the agitation increased. It was found that at 125rpm the strain rate and mass transfer coefficient in the in mini vessel were very close to those in the standard USP 2 system at 100rpm.

To the best of our knowledge, this first study focused on the basic hydrodynamics of mini vessel systems. The result of this work can provide guidance to their application in industry and help in comparing dissolution testing data obtained in different dissolution testing apparatuses.

Finally, the hydrodynamics of baffled trypsinizing shaker flasks was investigated. The Baffled Flask Test (BFT), based on the use of these flasks, has been proposed by EPA as the official standard protocol for testing dispersant effectiveness. The mixing energy in the baffled flask was investigated in this work using PIV to measure the water velocity in the flask placed at an orbital shaker that was rotated at seven rotation speeds from 100 rpm to 250 rpm. Two-dimensional velocity fields in large and small vertical cross sections of the flask for each rotation speed were obtained. The 1D energy spectra indicate nearly isotropic flow in the flasks for all rotation speeds and the existence of inertial subrange, which validate the use of dimensional argument analysis for the estimation of energy dissipation rate. The energy dissipation rate was estimated using dimensional argument for both cross sections, and the overall dissipation rates were the average of the results from the two cross sections.

In summary, the results obtained in this work will contribute to increase our understanding of the performance of a number of very common and important laboratory apparatus thus contributing to a more appropriate use of all these devices in both industry and federal and state agencies.

REFERENCES

[1] Lu, X.; Lozano, R.; Shah, P. In-Situ Dissolution Testing Using Different UV Fiber Optic Probes and Instruments. Dissol. Technol. 2003, 10, 6-15.

[2] Inman, G.W.; Wethington, E.; Baughman, K.; Horton, M. System Optimization for in Situ Fiber-Optic Dissolution Testing. Pharm. Technol. 2001, 10 (4), 92-100.

[3] Olmos, Eric.; Loubiere, Karine.; Martin, Céline.; Delaplace, Guillaume.; Marc, Annie. Critical Agitation for Microcarrier Suspension in Orbital Shaken Bioreactors: Experimental Study and Dimensional Analysis. Chemical Engineering Science. 2015, 122, 545-554.

[4] Colomera, Jordi.; Peters, Francesc.; Marrase, Celia. Experimental Analysis of Coagulation of Particles Under Low-Shear Flow. Water Research. 2005, 39, 2994-3000.

[5] Vikram, J.; Kaku, L.; Michel, C.; Boufadel, M.; Albert, D. Evaluation of Mixing Energy in Laboratory Flasks Used for Dispersant Effectiveness Testing. Journal of Environmental Engineering. 2006, 01, 93.

[6] Bai, G.; Armenante, P.M.; Plank, R.V.; Gentzler, M.; Ford, K.; Harmon, P. Hydrodynamic Investigation of USP Dissolution Test Apparatus II. J. Pharm. Sci. 2007, 96, 2327-2349.

[7] Bai, G.; Armenante, P.M. Hydrodynamic, Mass Transfer, and Dissolution Effects Induced by Tablet Location During Dissolution Testing. J. Pharm. Sci. 2009, 98, 1511-1531.

[8] Delvigne, G.A.L.; Sweeney, C.E. Natural Dispersion of Oil. Oil & Chemical Pollution. 1998, 4, 281-310.

[9] Tennekes, H.; Lumley, J.L. First course in turbulence. 1972, MIT Press.

[10] Bijlani, V.; Yuonayel, D.; Katpally, S.; Chukwumezie, B.N.; Adeyeye, M.C. Monitoring Ibuprofen Release From Multiparticulates: In Situ Fiber-Optic Technique Versus the HPLC Method: A Technical Note. AAPS Pharm. Sci. Tech. 2007, 8 (3), art. no. 52, E1-E4.

[11] Josefson, M.; Johansson, E.; Torstensson, A. Optical Fiber Spectrometry in Turbid Solutions by Multivariate Calibration Applied to Tablet Dissolution Testing. Anal. Chem. 1998, 60, 2666-2671.

[12] Wells, C. E. Effect of Sampling Probe on Dissolution of Tableted Drug Samples. J. Pharm. Sci. 1981, 70 (2), 232-233.

[13] Savage, T. S.; Wells, C. E. Automated Sampling of In Vitro Dissolution Medium: Effect of Sampling Probes on Dissolution Rate of Prednisone Tablets. J. Pharm. Sci. 1982, 71, 670-673.

[14] Cox, D. C.; Furman, W.B.; Moore, T.W.; Wells, C.E. Guidelines for Dissolution Testing: An Addendum. Pharm. Technol. 1984, 8(2), 42-46.

[15] Aldridge, P. K.; Kostek, L. J. In Situ Fiber Optics Dissolution Analysis. Dissolution Technol. 1995, 2(4), 10-11.

[16] Cho, J. H.; Gemperline, P. J.; Walker, D. S. Wavelength Calibration Method for a CCD Detector and Multi-Channel Fiber Optic Probes. Appl. Spectrosc. 1995, 49, 1841-1845.

[17] Cho, J. H.; Gemperline, P. J.; Salt, A.; Walker, D. S. UV/Visible Spectral Dissolution Monitoring by In Situ Fiber Optic Probes. Anal. Chem. 1995, 67, 2858-2863.

[18] Schatz, C.; Ulmschneider, M.; Altermatt, R.; Marrer, S. Manual In Situ Fiber Optic Dissolution Analysis in Quality Control. Dissolution Technol. 2000, 7(2), 6-13.

[19] Schatz, C.; Ulmschneider, M.; Altermatt, R.; Marrer, S.; Altorfer, H. Thoughts on Fiber-Optic Dissolution Testing, Dissolution Technol. 2001, 8(2), 6-11.

[20] Bynum, K.; Roinestad, K.; Kassis. A.; Pocreva, J.; Gehrlein, L.; Cheng, F.; Palermo, P. Analytical Performance of a Fiber Optic Probe Dissolution System. Dissolution Technol. 2001, 8(4), 1-8.

[21] Batchelor, G. K. An Introduction to Fluid Dynamics. 1967, Cambridge University Press, Cambridge, England.

[22] Nir, I.; Johnson, B. D.; Johansson, J.; Schatz, C. Application of Fiber-Optic Dissolution Testing for Actual Products. Pharm. Technol. 2002, 14(3), 20-28.

[23] Gray, V. Dissolution Testing Using Fiber Optics -A Regulatory Perspective. Dissolution Technol. 2003, 10(4), 33-36.

[24] Wunderlich, M.; Way, T.; Dressman, J. B. Practical Considerations When Using Fiber Optics for Dissolution Testing. Dissolution Technol. 2003, 10(4), 17-19.

[25] Toher, C. J.; Nielsen, P. E.; Foreman, A. S.; Avdeef, A. In situ Fiber Optic Dissolution Monitoring of a Vitamin B12 Solid Dosage Formulation. Dissolution Technol. 2003, 10(4), 20-25.

[26] Inman, G. W. Quantitative Assessment of Probe and Spectrometer Performance for a Multi-Channel CCD-based Fiber Optic Dissolution Testing System. Dissolution Technol. 2003, 10(4), 26–32.

[27] Martin, C. A. Evaluating the utility of fiber optic analysis for dissolution testing of drug products. Dissolution Technol. 2003, 10(4), 37–40.

[28] Gray, V. Challenges to the dissolution test, including equipment calibration. Dissolution Technol. 2006, 16(4), 6-9.

[29] Liu, L.; Fitzgerald, G.; Embry, M.; Cantu, R.; Pack, B. Technical Evaluation of a Fiber-Optic Probe Dissolution System. Dissolution Technol. 2008, 15(1), 10-20.

[30] Muhammad, T.; Wang, J.; Li-wan, M.; Chen, J. Monitoring Dissolution Rate of Amiodarone Tablets by a Multiple Fiber-Optic Sensor System. Dissolution Technol. 2008, 15(1), 22-27.

[31] Mirza, T.; Liu, Q.; Vivilecchia, R.; Joshi, Y. Comprehensive Validation Scheme for In Situ Fiber Optics Dissolution Method for Pharmaceutical Drug Product Testing. J. Pharm. Sci. 2009, 98(3), 1086-1094.

[32] Martin, C. A. Evaluating the utility of fiber optic analysis for dissolution testing of Nie, K.; Li, L.; Li, X.; Zhang, Y.; Mu, X.; Chen, J. Monitoring Ambroxol Hydrochloride Sustained-Release Tablets Release by Fiber-Optic Drug Dissolution In Situ Test System. Dissolution Technol. 2009, 16(1), 14-17.

[33] Bai, G.; Armenante, P. M. Velocity Distribution and Shear Rate Variability Resulting From Changes in the Impeller Location in the USP Dissolution Testing Apparatus II. Pharm. Res. 2008, 25(2), 320-336.

[34] The United States Pharmacopeia & The National Formulary. The Official Compendia of Standards, USP 35-NF 30. The United States Pharmacopeial Convention, Inc., Rockville, Maryland, 2012.

[35] Cox, D.C.; Furman, W.B. Systematic error associated with apparatus 2 of the USP dissolution test I: Effects of physical alignment of the dissolution apparatus. J Pharm. Sci. 1982, 71 (4):451-452.

[36] Kukura, J.; Baxter, J.L.; Muzzio, F.J. Shear distribution and variability in the USP Apparatus 2 under turbulent conditions. Int. J. Pharm. 2004, 279, 9-17.

[37] Baxter, J.L.; Kukura, J.; Muzzio, F.J. Shear-induced variability in the United States Pharmacopeia apparatus 2: Modifications to the existing system. AAPS J 7(4): E857-E864.

[38] Bai, G.; Armenante, P.M.; Plank, R.V. Experimental and Computational Determination of Blend Time in USP Dissolution Testing Apparatus II. J. Pharm. Sci. 2007, 96(11), 3072-3086.

[39] Kukura, J.; Arratia, P.C.; Szalai, E.S.; Muzzio, F.J. Engineering Tools for Understanding Hydrodynamics of Dissolution Tests. Drug. Dev. Ind. Pharm. 2003, 29, 231-239.

[40] Bai, G.; Wang, Y.; Armenante, P.M. Velocity Profiles and Shear Strain Rate Variability in the USP Dissolution Testing Apparatus 2 at Different Impeller Agitation Speeds. Int. J. Pharm. 2010, 403, 1-14.

[41] Wang, B.; Armenante, P.M. Effect of a Fiber-Optic Probe on the Dissolution of Salicylic Acid Tablets in USP Apparatus 2. Dissolution Technol. 2013, 5, 21-30.

[42] Wang, Y.; Armenante, P. M. A Novel Off-center Paddle Impeller (OPI) Dissolution Testing System for Reproducible Dissolution Testing of Solid Dosage Forms. J. Pharm. Sci. 2012, 101 (2), 746-760.

[43] The United States Pharmacopeia and National Formulary USP 35–NF 30; The United States Pharmacopeial Convention, Inc.: Rockville, MD, 2012.

[44] Moore, T. W. Dissolution Testing: A Fast, Efficient Procedure for Degassing Dissolution Medium. Dissolution Technol. 1996, 3 (2), 3-5.

[45] Lapin, L. Statistics: Meaning and Method; Harcourt Brace Jovanovich, Inc.: New York, 1975.

[46] Moore, J. W.; Flanner, H. H. Mathematical comparison of curves with an emphasis on in vitro dissolution profiles. Pharm. Tech. 1996, 20 (6), 64-74.

[47] Dissolution Testing of Immediate Release Solid Oral Dosage Forms; Guidance for Industry; U.S. Department of Health and Human Services, Food and Drug Administration, Center for Drug Evaluation and Research (CDER), U.S. Government Printing Office: Washington, DC, 1997.

[48] Dantec Dynamics A/S, 2002. FlowManager Software and Introduction to PIV Instrumentation-Software User's Guide. Dantec Dynamics A/S, Denmark.

[49] Courant, R., Friedrichs, K., & Lewy, H. Die Partiellen Differenzengleichungen der Mathematischen Physik. Mathematische Annalen (English version: On the Partial Difference Equations of Mathematical Physics), 1928, 100, 32-74.

[50] Parviz, M.; John, K. Tackling turbulence with supercomputers. Scientific American, 1997, 1, 276.

[51] Sahu, A.K.; Kumar, P.; Patwardhan, A.W.; Joshi, J.B. CFD Modelling and Mixing in Stirred Tanks. Chemical Engineering Science 1999, 54 (13-14), 2285-2293.

[52] Kieviet, F.G.; Van, R.J.; De Moor, P.P.E.A.; Kerkhof, P.J.A.M. Measurement and Modelling of the Air Flow Pattern in A Pilot-Plant Spray Dryer. Chemical Engineering Research and Design. 1997, 75 (A3), 321-328.

[53] Kumar, A. Numerical Investigation of Secondary Flows in Helical Heat Exchangers. Institute of Food Technologists Annual Meeting. 1995, Anaheim, CA, USA. pp. 148.

[54] Wanot, J. Computational Fluid Dynamics Methods in Ship Design. R&D projects, 1996, Germany.

[55] Bakker, A.; Ahmad, H.H.; Lanre, M.O. Realize Greater Benefits from CFD. Fluid/Solids Handling. 2001, March, pp. 45-53.

[56] Wilcox, D.C. Turbulence Modeling for CFD. 1993, DCW Industries. Inc., La Canada, California.

[57] Hanjalic, K.; Nagano, Y.; Tummers, M. Turbulence, Heat and Mass Transfer 4. 2003, Begell House Inc., Redding, Connecticut, pp. 625-632.

[58] Launder, B. E.; Spalding, D. B. Lectures in Mathematical Models of Turbulence. 1972, Academic Press, London, England.

[59] Zhang, Z.; Kleinstreuer, C. Low-Reynolds-Number Turbulent Flows in Locally Constricted Conduits: A Comparison Study. AAIA Journal. 2003, 41(5), 831-840.

[60] Batchelor, G. K. An Introduction to Fluid Dynamics. 1967, Cambridge University Press, Cambridge, England.

[61] Akiti, O.; Yeboah, A.; Bai, G.; Armenante, P. M. Hydrodynamic Effects on Mixing and Competitive Reactions in Laboratory Reactors. Chem. Eng. Sci. 2005, 60(8-9), 2341-2354.

[62] Hemrajani, R. R.; Tatterson, G. B. Mechanically Stirred Vessels. Handbook of Industrial Mixing-Science and Practice, by Paul E. L.; Atiemo-Obeng V. A.; Kresta, S. M. Eds.; John Wiley & Sons. 2004, New York, pp. 345-390.

[63] Tanaka, M.; Fujiwara, H.; Fujiwara, M. Effect of the Irregular Inner Shape of a Glass Vessel on Prednisone Dissolution Results. Dissolution Technol. 2005, 12(4), 15-19.

[64] Zhou, A.; Armenante, P.M. Experimental Determination of the Mixing Requirements for Solid Suspension in Pharmaceutical Stirred Tank Reactors. 2014, AIChE Annual Meeting.

[65] Fingas, M. "Use of Surfactants for Environmental Applications." Surfactants: Fundamentals and Applications to the Petroleum Industry, 2000, Cambridge University Press, Cambidge, UK, 461-539.

[66] NRC. Oil in the Sea III: Inputs, Fates, and Effects. 2003, National Academies Press.

[67] NRC. Oil Spill Dispersants: Efficacy and Effects. 2005, National Academic Press.

[68] Kaku, V. J.; Boufadel, M. C.; Venosa, A. D.; Weaver, J. Flow Dynamics in Eccentrically Rotating Flasks Used For Dispersant Effectiveness Testing. Environmental Fluid Mechanics, 2006, 6, 385-406.

[69] Kaku, V. J.; Boufadel, M. C.; Weaver, J. W. Scaling Exponents of Structure Functions in an Eccentrically Rotating Flask. Adv. Thor. Appl. Mech. 2010, 3, 233-252.

[70] Delvigne, G. A. Natural Dispersion of Oil by Different Sources of Turbulence. Proc., International Oil Spill Conference, American Petroleum Institute, 415-419.

[71] Fingas, M. F. Dispersants: A Review of Effectiveness Measures and Laboratory Physical Studies. Proc., Proc. Alaska RRT Dispersant Workshop, 37.

[72] Venosa, A. D.; Holder, E. L. Determining the Dispersibility of South Louisiana Crude Oil by Eight Oil Dispersant Products Listed on the NCP Product Schedule. Marine pollution bulletin, 2013, 66(1), 73-77.

[73] Hinze, J. Turbulence. 1975, McGraw-Hill, New York.

[74] Liu, Z.-C.; Landreth, C.; Adrian, R.; Hanratty, T. High Resolution Measurement of Turbulent Structure in a Channel with Particle Image Velocimetry. Experiments in Fluids. 1991, 10(6), 301-312.

[75] Hyun, B.; Balachandar, R.; Yu, K.; Patel, V. Assessment of PIV to Measure Mean Velocity and Turbulence in Open-Channel Flow. Experiments in Fluids. 2003, 35(3), 262-267.

[76] Cheng, C-Y.; Atkinson, J. F.; Bursik, M. I. Direct Measurement of Turbulence Structures in Mixing Jar Using PIV. Journal of Environmental Engineering. 1997, 123(2), 115-125.

[77] Delafosse, A.; Collignon, M.-L.; Crine, M.; Toye, D. Estimation of the Turbulent Kinetic Energy Dissipation Rate from 2D-PIV Measurements in a Vessel Stirred by an Axial Mixel TTP Impeller. Chemical Engineering Science. 2011, 66(8), 1728-1737.

[78] Kilander, J.; and Rasmuson, A. Energy Dissipation and Macro Instabilities in a Stirred Square Tank Investigated Using PIV Approach and LDA Measurements. Chemical Engineering Science. 2005, 60(24), 6844-6856.

[79] Micheletti, M.; Baldi, S.; Yeoh, S.; Ducci, A.; Papadakis, G.; Lee, K.; Yianneskis, M. On Spatial and Temporal Variations and Estimates of Energy Dissipation in

Stirred Reactors. Chemical Engineering Research and Design. 2004, 82(9), 1188-1198.

[80] Sheng, J.; Meng, H.; Fox, R.NA Large Eddy PIV Method for Turbulence Dissipation Rate Estimation. Chemical Engineering Science. 2000, 55(20), 4423-4434.

[81] Nelkin, M. Universality and Scaling in Fully Developed Turbulence. Advances in Physics. 1994, 43(2), 143-181.

[82] Delvigne, G. A. L.; Sweeney, C. E. Natural Dispersion of Oil. Oil & Chemical Pollution. 1988, 4, 281-310.

[83] Tennekes, H.; Lumley, J. L. First Course in Turbulence. 1972, MIT Press.

[84] Kresta, S.; Wood, P. The Flow Field Produced by a Pitched Blade Turbine: Changes in the Circulation Pattern Due to Off Bottom Clearance. Can. J. Chem. Eng. 1993, 71, 42-53.

[85] Dantec Dynamics A/S. FlowManager Software and Introduction to PIV Instrumentation-Software User's Guide. 2002, Dantec Dynamics A/S, Denmark.

[86] Frisch, U. Turbulence, the Legacy of A.N. Kolmogorov. 1995, Cambridge University Press, Cambridge, UK.

[87] Kolmogorov, A. N. The Local Structure of Turbulence in Incompressible Viscous Fluid for Very Large Reynolds Number. Dokl. Akad. Nauk., SSSR 1941, 30, 301-305. Reprinted in 1991: Proc. R. Sco. Lond. A1434, 1999-1913.

[88] Kaimal, J. C.; Finnigan, J. J. Atmospheric Boundary Layer Flows: Their Structure and Measurement. 1994, Oxford University Press, New York.

[89] Gilbert, A. D. Spiral Structures and Spectra in Two-Dimensional Turbulence. Journal of Fluid Mechanics. 1988, 193, 475-497.

[90] Tanaka, T.; and Eaton, J. K. A Correction Method for Measuring Turbulence Kinetic Energy Dissipation Rate by PIV. Experiments in Fluids. 2007, 42(6), 893-902.

[91] Hinze, J. Fundamentals of The Hydrodynamic Mechanism of Splitting in Dispersion Processes. AIChE Journal. 1955, 1(3), 289-295.

[92] Luo, H.; Svendsen, H. F. Theoretical Model for Drop and Bubble Breakup in Turbulent Dispersions. AIChE Journal. 1996, 42(5), 1225-1233.

[93] Baldi, S.; Yianneskis, M. On the Direct Measurement of Turbulence Energy Dissipation in Stirred Vessels with PIV. Industrial & Engineering Chemistry Research. 2003, 42(26), 7006-7016.

[94] Dissolution Testing of Immediate Release Solid Oral Dosage Forms;Guidance for Industry; U.S. Department of Health and Human Services, Food and Drug Administration,Center for Drug Evaluation and Research (CDER), U.S. Government Printing Office:Washington, DC, 1997.

[95] Waiver of In Vivo Bioavailability and Bioequivalence Studies for Immediate-Release Solid Oral Dosage Forms Based on a Biopharmaceutics Classification System; Guidance for Industry; U.S. Department of Health and Human Services, Food and Drug Administration,Center for Drug Evaluation and Research (CDER), U.S. Government Printing Office:Washington, DC, 2000.

[96] Amidon, G.; Lennernas, L.H.; Shah, V.P.; Crison, J.R. A Theoretical Basis for a Biopharmaceutic Drug Classification: The Correlation of In Vitro Drug Product Dissolution and In Vivo Bioavailability. Pharm. Res. 1995, 12, 413-420.

[97] Gu, C.H.; Gandhi, R.B.; Tay, L.K.; Zhou, S.; Raghavan, K. Importance of using physiologically relevant volume of dissolution medium to correlate the oral exposure of formulations of BMS-480188 mesylate. Int. J. Pharm. 2004, 269, 195-202.

[98] Scale-Up and Postapproval Changes for Modified Release Solid Oral Dosage Forms; Guidance for Industry; U.S. Department of Health and Human Services, Food and Drug Administration, Center for Drug Evaluation and Research (CDER), U.S. Government Printing Office: Washington, DC, 1997.

[99] Avdeef, A. Solubility of Sparingly Soluble Ionizable Drugs. Adv. Drug Deliv. 2007, 59, 568-590.

[100] Klein, S.; Shah, V. The Mini Paddle Apparatus a Useful Tool in the Early Developmental Stage Experiences with Immediate-Release Dosage Forms. Dissolution Technol. 2006, 13, 6-11.

[101] Middleman S. An introduction to mass and heat transfer. New York: John Wiley & Sons, Inc. 1998.

[102] Bird, R. Byron.; Stewart, Warren E.; Lightfoot, Edwin N. Transport Phenomena. New York: John Wiley & Sons, Inc. 2002.

[103] Geankoplis, Christie John. Transport Processes and Separation Process Principles. Upper Saddle River, New Jersey: Prentice Hall. 2003.

[104] Labraga, L.; Berkah, T. Mass Transfer from A Rotating Cylinder With and Without Crossflow. Int. J. Heat. Mass. Transf. 2004, 47: 2493-2499.